

## ABSTRACT

HASAN, TAMIR SAFA. Microstructural Modeling of Nanocrystalline Twinned Face Centered Cubic Systems. (Under the direction of Professor Mohammed Zikry).

Nanocrystalline-twinned materials exhibit significantly higher strength and ductility than nanocrystalline face centered cubic (f.c.c.) materials without twins. The underlying material mechanisms have not been well quantified or fundamentally understood. In this investigation, a dislocation-density based multiple-slip crystalline constitutive and a nonlinear finite-element formulation have been used to understand how twin volume fractions, grain and twin orientations and texture, dislocation-density accumulation, and large inelastic strains affect the competing strengthening and toughening effects in nanotwinned materials. Dislocation-density accumulation at twin boundaries that resulted in local and global strengthening and toughening occurred because of inelastic strain accumulation within the nanograins and nanotwins. Furthermore, the predictions have indicated that the highest strengthening for the nanocrystalline-twinned materials are physically representative of high and low angle grain-boundary (GB) misorientations with respect to the loading axis. The predictions were validated with experiments pertaining to nanotwinned f.c.c. copper aggregates. The validated predictions from this investigation can be used as design guidelines for optimizing the mechanical behavior of nanotwinned crystalline materials, such that failure can be mitigated and controlled at the nanocrystalline scale.

© Copyright 2015 Tamir Safa Hasan

All Rights Reserved

Microstructural Modeling of Nanocrystalline Twinned Face Centered Cubic Systems

by  
Tamir Safa Hasan

A thesis submitted to the Graduate Faculty of  
North Carolina State University  
in partial fulfillment of the  
requirements for the degree of  
Master of Science

Mechanical Engineering

Raleigh, North Carolina

2015

APPROVED BY:

---

Dr. Mohammed Zikry  
Committee Chair

---

Dr. Jeffrey Eischen

---

Dr. Kevin Lyons

## **DEDICATION**

Dedicated to my parents.

## **BIOGRAPHY**

Tamir Hasan was born in Linköping, Sweden, where he spent a few short months of his early life before his family immigrated to the United States. He grew up in a rural town in North Carolina where he always took for granted his wondrous view of the night sky. He attended the North Carolina School of Science and Math for his final two years of secondary school, where he built and tested rocket engines as part of a research course. After graduating, he enrolled in the Mechanical Engineering program at North Carolina State University in Raleigh. While there, his interests expanded to include volunteering as a firefighter and EMT at a local fire department and turning wrenches on his beloved 1986 Toyota MR2. He graduated with his Bachelor's degree from North Carolina State University in May 2013 and thereafter returned for a Master's degree.

Tamir has accepted a position at Eaton Corporation as an Engineering and Technology Leadership Development Program participant.

## ACKNOWLEDGEMENTS

I would like to acknowledge my family for their unwavering support of my education and for all of their quite sensible advice.

To my committee: Dr. Zikry, Dr. Eischen, and Dr. Lyons. Thank you for your time and flexibility.

Thanks to Dr. Lyons and to Dr. Kribs for befriending me as a freshman and giving me a lab to call home.

Special thanks are also due to Dr. Zikry, who believed in me from the onset and who, in his nonchalant manner, expected nothing short of excellence of me.

I would also like to thank my office mates for the past year and a half: Dr. Prasenjit Khanikar, Dr. Letisha McLaughlin Lam, Dr. Drew LaBarbera, Dr. Qifeng Wu, Shoayb Ziaei, Judith Brown, Bingxiao Zhao, Matt Bond, Michael Rosenberg, and Ismail Mohamed. Thank you for the discussions, the help, and the invitations to lunch. Special thanks also to Dr. Drew LaBarbera for never hesitating to share his extensive knowledge of Crystal2D.

Support from the Office of Naval Research through Grant N000140510097 is also gratefully acknowledged.

## TABLE OF CONTENTS

LIST OF TABLES .....	vi
LIST OF FIGURES .....	vii
CHAPTER 1: INTRODUCTION TO CRYSTALLOGRAPHIC TWINNING .....	1
1.1 Overview .....	1
1.2 Experimental Results .....	2
Applications .....	4
Modeling of Nanocrystalline-Twinned Materials .....	5
CHAPTER 2: DISLOCATION-DENSITY BASED MULTIPLE-SLIP CRYSTALLINE CONSTITUTIVE FORMULATION .....	7
2.1 Multiple-Slip Crystal Plasticity Formulation .....	7
2.2 Mobile and Immobile Dislocation Density Evolution Equations .....	10
2.3 Numerical Methods .....	14
CHAPTER 3: VALIDATION WITH EXPERIMENTAL RESULTS .....	15
3.1 Further examination of 19% Twin Volume Fraction Case .....	16
3.2 Conclusions .....	18
CHAPTER 4: ORIENTATION EFFECTS ON TWINNED AGGREGATES .....	26
4.1 Mesh Convergence .....	27
4.2 Grain Aggregate Size .....	27
4.3 Comparison of Stress-Strain Responses .....	27
4.4 Dislocation Density Evolution .....	29
4.5 Lattice Rotation, Shear Slip, and Stress Buildup .....	33
4.6 Predictions of Twinned Materials under Compression .....	34
4.7 Conclusions .....	35
CHAPTER 5: RECOMMENDATIONS FOR FUTURE RESEARCH .....	96
BIBLIOGRAPHY .....	97

## LIST OF TABLES

Table 1: Parent and equivalent twin slip systems .....	20
Table 2: Experimental microstructure description .....	20
Table 3: Simulation parameters .....	21

## LIST OF FIGURES

Figure 1: Comparison of experimental and predicted stress-strain curves. ....	19
Figure 2: Representative material featuring randomized grains and twin lamella. (Spatial dimensions are in meters) .....	22
Figure 3: Normalized dislocation density values from one slip system. (Spatial dimensions are meters).....	23
Figure 4: Lattice rotation at terminal strain showing that twinned regions have an effect on local rotation. (Spatial dimensions are meters).....	23
Figure 5: Shear slip in the material appears localized in either the twinned or parent material, depending on grain orientation. (Spatial dimensions are meters).....	24
Figure 6: Stress distribution in the material, normalized by the yield stress. (Spatial dimensions are meters) .....	24
Figure 7: Normalized shear stress. (Spatial dimensions are meters) .....	25
Figure 8: Normalized lateral stress. (Spatial dimensions are meters).....	25
Figure 9: Example of a 30° oriented twinned structure. $\phi = 30^\circ \pm 10^\circ$ . (Spatial units are in meters).....	36
Figure 10: Normal mesh density (top) and refined mesh (bottom) .....	37
Figure 11: Mesh convergence in 45° simulation. ....	38
Figure 12: Comparison of 9-grain and 16-grain simulated results. ....	38
Figure 13: Stress-strain curves comparison of 19% v.f. simulation experimental results and orientation results .....	39
Figure 14: Twinned and non-twinned material responses quantified in the form of toughness. Toughness was determined at the experimentally observed nominal failure strain. ....	40
Figure 15: Percentage increase in toughness between twinned and non-twinned simulations. ....	40
Figure 16: Stress-strain curves for the twinned and non-twinned versions of the 45° material. ....	41
Figure 17: Correlation between twinned percent deviation in immobile dislocation density and toughness percent change for the [111](101) parent slip system and the [200](020) twin slip system.....	42
Figure 18: Correlation between twinned percent deviation in immobile dislocation density and toughness percent change for the 111110 parent slip system and the [002](110) twin slip system.....	43

Figure 19: Relation between twinned percent deviation in mobile dislocation density and toughness percent change for the [111](011) parent slip system and the [002](110) twin slip system.....	44
Figure 20: Correlation between twinned percent deviation in mobile dislocation density and toughness percent change for the [111](011) parent slip system and the [111](011) twin slip system.....	45
Figure 21: Aggregate immobile dislocation density percent change compared with percent changes in toughness values for twinned materials and their non-twinned counterparts. ....	46
Figure 22: Aggregate mobile dislocation density percent change compared with percent changes in toughness values for twinned materials and their non-twinned counterparts. ....	47
Figure 23: Total immobile dislocation densities summed over all slip systems. All spatial units are in meters. Dislocation densities are normalized by their initial values. ....	48
Figure 24: Total mobile dislocation density, across all slip systems. All spatial units are in meters. Dislocation densities are normalized by their initial values. ....	53
Figure 25: [111](101) parent/[200](020) twin slip system immobile dislocation density for 0°, 15°, 30°, 45°, 60°, 75°, and 90° are shown above. All spatial units are in meters. Dislocation densities represented are normalized by their initial values. ....	58
Figure 26: [111](011) parent/[111](011) twin slip system mobile dislocation density for 0°, 15°, 30°, 45°, 60°, 75°, and 90° are shown above. All spatial units are in meters. Dislocation densities represented are normalized by their initial values. ....	63
Figure 27: Lattice rotation for twinned and non-twinned materials at various orientations. (All spatial units are in meters) .....	68
Figure 28: Shear slip comparisons between twinned and non-twinned materials. (All spatial units are in meters) .....	73
Figure 29: Percent difference in aggregate shear slip compared with material orientation....	78
Figure 30: Normalized stress comparisons between twinned and non-twinned materials. (All spatial units are in meters) .....	79
Figure 31: Aggregate normal stress percentage increase from non-twinned to twinned materials plotted against orientation. Note that all twinned materials represent an increase in aggregate normal stress.....	84
Figure 32: Normalized lateral stress for twinned and non-twinned materials. (All spatial units are in meters).....	85
Figure 33: Normalized Shear Stress for twinned and non-twinned materials. (All spatial units are in meters).....	90

Figure 34: Compressive loading at different orientations compared with experimental toughness for comparison. .... 95

Figure 35: Toughness increase from non-twinned simulation shown as function of orientation. .... 95

## **CHAPTER 1: INTRODUCTION TO CRYSTALLOGRAPHIC TWINNING**

### **1.1 Overview**

Twinning is a phenomenon observed in crystallographic materials in which the direction of a uniform lattice is mirrored across a particular plane, referred to as the twin plane. (Niewczas 2007) Non-twinned material is referred to as parent material. Nanotwins have relatively low thicknesses, generally measured on the order of tens of nanometers, and have been experimentally shown to induce a significant strengthening effect in crystalline materials. Plastic deformation occurs when atomic dislocations move throughout a material in response to applied stress. Therefore, the strength and ductility of a material is directly dependent on the material characteristics that block dislocation motion or store dislocations, such as the addition of twin boundaries. (You, Lu and Lu 2011) This factor is influenced by the material properties and microstructural texture. Twin boundaries behave much in the same manner as grain boundaries (GBs) within a material, and the dislocation activity may be regarded in the same way as in subgrain structures. (Rezvanian, Zikry and Rajendran 2007, Dao, et al. 2006, Christian and Mahajan 1995)

Twinning is a mechanism that crystalline materials use to cope with stress application and to maintain a low energy state. It occurs naturally during plastic deformation and other mechanical or chemical processes that encourage energy minimization through the application of shear. (Lu, Shen, et al. 2004) Recent experimental studies have focused on the effects of applied twinning on the strength and ductility of crystallographic materials. This class of materials promises a new method of material strengthening and toughening in

addition to conventional methods that have included grain size refinement and secondary phases. Material tensile strength has been shown to increase by up to ten times in nanocrystalline-twinned materials when compared with non-twinned materials. (Lu, Shen, et al. 2004) Other experimentally observed benefits include increases in ductility and crack blunting during fracture. (Shan, et al. 2008)

This investigation is focused on developing a validated computational framework for understanding nanocrystalline-twinned materials and identifying the mechanisms by which twinning strengthens and improves ductility in materials. Specifically, the effects of orientation of twinned materials are examined in materials undergoing tensile and compressive loading conditions. This will lead to understanding and identifying how mechanisms that include dislocation-density evolution and stress and shear strain accumulation affect strengthening and toughening.

## **1.2 Experimental Results**

Recent experimental results have shown that coherent nanoscale twin boundaries in crystalline materials result in a strengthening effect while maintaining high levels of ductility. This is in contrast with the method of refining grain size for strengthening grained material, in which high strength is achieved at the expense of ductility when compared with coarse-grained materials. (Lu, Shen, et al. 2004, Koch, et al. 1999) Twin boundaries have been determined to be coherent to the parent crystal lattice, and may act as sources, sinks, or blocking structures for dislocations. (Lu, Zhu, et al. 2009) The experimental analysis of twinned materials has shown that the effect of twinned boundaries on dislocations moving

throughout the material, either by blockage or partial glissile dislocation creation, generates a significant contribution to the overall strength and ductility of the material. (Lu, Shen, et al. 2004) Dislocations have generally been observed in concentrated form at twin boundaries and are less common within twin lamella. (Shen, et al. 2005, Dao, et al. 2006) Molecular dynamics (MD) simulations have also demonstrated that twin boundaries can serve as boundaries to inhibit dislocation motion. (Yamakov, et al. 2003)

Experimental results have demonstrated the strengthening effects of nanotwins in various f.c.c. materials that include copper (Lu, Shen, et al. 2004) and stainless steel. (Zhang, et al. 2004) The most common techniques for the reliable formation of strengthening twins include pulsed electrodeposition (Lu, Shen, et al. 2004, Shen, et al. 2005), sputter deposition (Zhang, et al. 2004), and dynamic plastic deformation at cryogenic temperatures (Wang, Wang and Lu 2011, Xiao, Tao and Lu 2011).

The pulsed electrodeposition technique utilizes an electrolyte of  $\text{CuSO}_4$  to create thin Cu sheets with thicknesses of  $\sim 500 \mu\text{m}$  that exhibit twinning. Highly purified Cu and Ti sheets are used as anodes and cathodes, respectively. When using this method, modification of the electrodeposition parameters allows control over specific physical features such as the grain sizes and twin thicknesses. (You, Lu and Lu 2011, Chen, Lu and Lu 2011) Procedures have been developed to ensure preferential grain orientation in as-deposited materials. (You, Lu and Lu 2011) This technique has shown that smaller grain sizes and even smaller twin thicknesses result in the greatest strengthening. Specifically, the nanotwinned Cu samples that have exhibited the highest strengths had twin thicknesses on the order of  $\sim 15\text{-}20 \text{ nm}$  and grain sizes on the order of  $\sim 500 \text{ nm}$ . (Chen, Lu and Lu 2011, Lu, et al. 2005) Reduced

strength and ductility were observed in samples with higher twin thicknesses. (Lu, et al. 2005) This is partially a result of lower twin thicknesses inhibiting the nucleation of new dislocations. (Shan, et al. 2008)

Sputter deposition can also be used in the creation of nanotwinned materials. Cu/330 Stainless Steel multilayers have been deposited on Si substrates in near vacuum conditions, resulting in twinning. Microstructural analysis has revealed that the f.c.c. crystal structure was maintained throughout the resulting material, and that the material had a texture strongly oriented perpendicular to the deposition plane. (Zhang, et al. 2004) In this scenario, increases in material hardness were observed because the twinned interfaces blocked dislocation motion. (Zhang, et al. 2004)

Dynamic plastic deformation (DPD) is another process that has been developed to create twinned materials. It is a subset of the severe plastic deformation twin formation method that involves applying high compressive stresses to materials that result in high strains. (Hong, Tao and Huang, et al. 2010, Wang, Wang and Lu 2011) The strains applied during this process determine the volume fraction of the resulting twins. (Xiao, Tao and Lu 2011) This method has shown promise in the development of materials with preferential twin orientation by responding in a predictable manner to differing grain orientations. (Hong, Tao and Lu, et al. 2009)

### **1.3 Applications**

In addition to being applicable to any setting in which high material strength and ductility are preferred, twinned materials can also be used across a spectrum of more specific

applications. Nanotwinned copper aggregates improve materials used in three-dimensional integrated-circuit packaging. This leads to increased mechanical strength and chip life. (Hsiao, et al. 2012) Improvements in electrical conductivity in Cu have also been measured, which is rare to find in conjunction with increased strength. (Lu, Shen, et al. 2004)

#### **1.4 Modeling of Nanocrystalline-Twinned Materials**

Modeling of nanocrystalline-twinned materials has mainly focused on molecular dynamics (MD) simulations. These included the modeling of dislocation-dislocation and dislocation-twin boundary interactions to further understand specific atomistic behaviors at twin boundaries (Yamakov, et al. 2003, Wu, Zhang and Srolovitz 2009), modeling the nucleation characteristics of twins (Li, et al. 2010), and modeling of aggregates with twinned structures and random grain orientations. (Dao, et al. 2006, Zhou, Qu and Yang 2010) Many of these modeling techniques have been successful in reproducing specific experimentally derived responses of twinned materials. Some finite element modeling of twinned aggregates has also been performed using strain gradient plasticity theory, and this modeling also matches experimental results. (Wu and Wei 2008)

The specific mechanisms resulting in the strengthening and toughening of nanocrystalline-twinned materials have not been identified or understood. Therefore, a dislocation-density based crystalline plasticity formulation and a nonlinear finite element framework will be used to analyze nanocrystalline-twinned aggregates on the microstructural scale. This approach will provide an understanding of how aggregate dislocation density evolution and crystalline slip affects material behavior with different volume fractions and

loading conditions. The twins, which are known to form on the [111] plane in f.c.c. materials, were oriented properly with respect to their individual parent grains on the 2-D projection for a plane strain representation (Chen, et al. 2003, Pumphrey and Bowkett 1971, Cronje, et al. 2013)

This thesis is organized as follows: Chapter 2 describes the general theory behind the dislocation density-based formulation utilized in this research; Chapter 3 includes results from finite element method simulations that were designed to recreate experimental results; Chapter 4 includes results from finite element method simulations designed to better understand the mechanisms behind twin strengthening, especially as related to twin orientation; and Chapter 5 gives an overview of proposed future research objectives.

## CHAPTER 2: DISLOCATION-DENSITY BASED MULTIPLE-SLIP CRYSTALLINE CONSTITUTIVE FORMULATION

This chapter presents the formulation for the finite deformation of multiple-slip crystal plasticity rate-dependent constitutive relations that are coupled to evolutionary nonlinear equations for mobile and immobile dislocation densities. A more thorough treatment of this dislocation-density based formulation may be found in (Zikry and Kao 1996) and (Kameda and Zikry 1998).

### 2.1 Multiple-Slip Crystal Plasticity Formulation

The material deformation gradient tensor,  $F_{ik}$ , is used to define the spatial velocity gradient,  $L_{ij}$ , as follows:

$$L = \dot{F} \cdot F^{-1} \quad (2.1)$$

It is assumed that the velocity gradient is composed of symmetric and skew-symmetric parts:

$$L_{ij} = D_{ij} + W_{ij} \quad (2.2)$$

Here, the symmetric portion, or the deformation rate tensor, is defined as:

$$D_{ij} = \frac{1}{2}(L_{ij} + L_{ji}), \quad (2.3)$$

and the skew-symmetric part, or the total spin tensor, is defined as:

$$W_{ij} = \frac{1}{2}(L_{ij} - L_{ji}). \quad (2.4)$$

These two tensors can be logically decomposed into elastic and inelastic components:

$$D_{ij} = D_{ij}^e + D_{ij}^p, \quad W_{ij} = W_{ij}^e + W_{ij}^p. \quad (2.5)$$

The plastic components can then be further reduced to relations that are defined in terms of the crystallographic slip rate:

$$D_{ij}^P = P_{ij}^{(\alpha)} \dot{\gamma}^{(\alpha)} \quad W_{ij}^P = \omega_{ij}^{(\alpha)} \dot{\gamma}^{(\alpha)}. \quad (2.6)$$

Here,  $(\alpha)$  indicates a summation across all slip systems. The composing elements  $P_{ij}^{(\alpha)}$  and  $\omega_{ij}^{(\alpha)}$ , which represent the symmetric and asymmetric components of the Schmid tensor, are defined as:

$$P_{ij}^{(\alpha)} = \frac{1}{2} (s_i^{(\alpha)} n_j^{(\alpha)} + s_j^{(\alpha)} n_i^{(\alpha)}) \quad \omega_{ij}^{(\alpha)} = \frac{1}{2} (s_i^{(\alpha)} n_j^{(\alpha)} - s_j^{(\alpha)} n_i^{(\alpha)}). \quad (2.7)$$

Here,  $s_i^{(\alpha)}$  represents the unit vector in the slip direction and  $n_i^{(\alpha)}$  is the unit vector normal to the slip plane.

Plastic strain is incorporated through the plastic deformation rate tensor, which represents the effective plastic shear slip, as shown below:

$$\gamma_{eff} = \frac{2}{3} \int \sqrt{D_{ij}^P D_{ij}^P} dt \quad (2.8)$$

The elastic response is represented using the Jaumann stress rate, which is corotational with the lattice:

$$\sigma_{ij}^{\Delta,e} = C_{ijkl} D_{kl}^e \quad (2.9)$$

Here,  $C_{ijkl}$  is the material matrix: a fourth-order isotropic elastic modulus tensor defined as follows:

$$C_{ijkl} = \mu (\delta_{ik} \delta_{jl} + \delta_{jk} \delta_{il}) + \lambda \delta_{ij} \delta_{kl}. \quad (2.10)$$

The Jaumann stress rate can then be described as a term of the material stress rate in the reference coordinate system as follows:

$$\dot{\sigma}_{ij} = \sigma_{ij}^{\Delta,e} + W_{ik}^e \sigma_{kj} + W_{jk}^e \sigma_{ki}. \quad (2.11)$$

Slip rates by slip system are formulated using the assumption of power law hardening. (Hutchinson 1976) The slip rates are related to the resolved shear stresses by slip system.

$$\dot{\gamma}^{(\alpha)} = \dot{\gamma}_{ref}^{(\alpha)} \left[ \frac{\tau^{(\alpha)}}{\tau_{ref}^{(\alpha)}} \right] \left[ \frac{|\tau^{(\alpha)}|}{\tau_{ref}^{(\alpha)}} \right]^{\left(\frac{1}{m}\right)-1} \quad \text{no sum on } \alpha. \quad (2.12)$$

Here,  $\dot{\gamma}_{ref}^{(\alpha)}$  is the reference shear strain rate that corresponds to a reference shear stress  $\tau_{ref}^{(\alpha)}$ .

The strain rate sensitivity parameter, represented as  $m$ , is defined by:

$$m = \frac{\partial \ln \tau^{(\alpha)}}{\partial \ln \dot{\gamma}^{(\alpha)}}. \quad (2.13)$$

The reference shear stress is determined by incorporating the hardening effects of immobile dislocation density  $\rho_{im}$ , an interaction coefficient to track dislocation movement between slip systems  $a_{\alpha j}$ , thermal softening using a negative exponent  $\xi$ , and a normalizing reference temperature  $T_r$  (293 K). The Burgers vector is denoted by  $b$  and the number of slip systems in the material is denoted by  $nss$ .

$$\tau_{ref}^{(\alpha)} = \left( \tau_s^\alpha + \mu b \sum_{j=1, nss} \sqrt{a_{\alpha j} \rho_{im}^j} \right) \left( \frac{T}{T_r} \right)^\xi \quad (2.14)$$

In the present study, interaction coefficients are varied between twinned and non-twinned (parent) structures. Motivation for representing the material in this manner was drawn from indications from experimental studies that relatively few dislocations were present in twinned structures after deformation, along with observations of increased slip activity occurring near twin boundaries. (Shen, et al. 2005, Mirkhani and Joshi 2011)

Temperature ( $T$ ) is updated using the following rate of change formulation that is related to the rate of plastic work.

$$\dot{T} = \frac{\chi}{\rho c_p} \sigma_{ij}^{dev} D_{ij}^p \quad (2.15)$$

Here,  $\chi$  is the fraction of plastic work converted to heat,  $\rho$  is the material density,  $c_p$  is the specific heat of the material, and  $\sigma_{ij}^{dev}$  is the deviatoric stress.

## 2.2 Mobile and Immobile Dislocation Density Evolution Equations

The total dislocation density,  $\rho^{(\alpha)}$ , of a structure is assumed to be additively composed of mobile ( $\rho_m^{(\alpha)}$ ) and immobile ( $\rho_{im}^{(\alpha)}$ ) dislocation densities, as shown below:

$$\rho^{(\alpha)} = \rho_m^{(\alpha)} + \rho_{im}^{(\alpha)} \quad (2.16)$$

As a material is strained, the simulation of various material effects can modify mobile and immobile dislocation densities. These include mobile dislocation density generation, dislocation interactions between the mobile and immobile dislocation densities, or immobile dislocation density annihilation. (Shanthraj and Zikry 2011) These are represented using the following coupled differential equations:

$$\dot{\rho}_m^{(\alpha)} = \dot{\rho}_{generation}^{(\alpha)} - \dot{\rho}_{interaction-}^{(\alpha)} \quad (2.17)$$

$$\dot{\rho}_{im}^{(\alpha)} = \dot{\rho}_{interaction+}^{(\alpha)} - \dot{\rho}_{annihilation}^{(\alpha)} \quad (2.18)$$

The components of these differential equations include the generation term:

$$\dot{\rho}_{generation}^{(\alpha)} = \rho_{source}^{(\alpha)} \left( \frac{v^{(\alpha)}}{y_{back}} \right), \quad (2.19)$$

which is composed of the velocity of a mobile dislocation divided by the average distance traveled by a dislocation  $y_{back}$  emitted from a dislocation source  $\rho_{source}$ . The generation rate can be further modified using the Orowan equation,  $\dot{\gamma}^{(\alpha)} = \rho_m^{(\alpha)} b^{(\alpha)} v^{(\alpha)}$ :

$$\dot{\rho}_{generation} = \phi \sum_{\beta} \frac{\sqrt{\rho_{im}^{(\beta)}}}{b^{(\alpha)}} \left( \frac{\rho_{im}^{(\alpha)}}{\rho_m^{(\alpha)}} \right) \dot{\gamma}^{(\alpha)}. \quad (2.20)$$

Here,  $\phi$  is a geometric parameter and  $b^{(\alpha)}$  is the Burgers vector length on slip system  $\alpha$ .

The dislocation density formulation also involves mobile dislocation immobilization as a result of the interactions of dislocation densities on separate slip systems. The relative velocity between two slip systems assumed to interact is defined as:

$$v^{(\alpha\beta)} = \frac{\dot{\gamma}^{(\alpha)}}{\rho_m^{(\alpha)} b^{(\alpha)}} + \frac{\dot{\gamma}^{\beta}}{\rho_m^{(\beta)} b^{(\beta)}} \quad (2.21)$$

The junction length bridging two slip systems is assumed to be dependent on the immobile dislocation spacing:

$$l_c = \frac{1}{\sum_{\beta} \sqrt{\rho_{im}^{(\beta)}}}. \quad (2.22)$$

From the above formulations, the dislocation density immobilization rates on slip system  $\alpha$  because of the interaction with slip system  $\beta$  are  $f_0 \rho_m^{(\alpha)} \rho_{im}^{(\beta)} l_c v^{(\alpha)}$  for the effect of immobile dislocations from  $\beta$  and  $f_0 \rho_m^{(\alpha)} \rho_m^{(\beta)} l_c v^{(\alpha\beta)}$  for the effect of mobile dislocations from  $\beta$ .  $f_0$  represents the fraction of the junctions that are stable and contribute to the immobilization rate. The rate of mobile dislocation density immobilization on slip system  $\alpha$  can then be derived as:

$$\dot{\rho}_{interaction-}^{(\alpha)} = f_0 \sum_{\beta} \left( \rho_m^{(\beta)} l_c \left( \frac{\dot{\gamma}^{(\alpha)}}{b^{(\alpha)}} \right) + \rho_m^{(\alpha)} l_c \left( \frac{\dot{\gamma}^{(\beta)}}{b^{(\beta)}} \right) \right) + f_0 \sum_{\beta} \rho_{im}^{(\beta)} l_c \left( \frac{\dot{\gamma}^{(\alpha)}}{b^{(\alpha)}} \right) \quad (2.23)$$

This interaction formulation also incorporates the effects of dislocation interactions forming further dislocation junctions. Frank's rule is used to determine the energetically favorable interactions, which may lead to immobile junction formation. The dislocation density interaction tensor for junction formation on slip system  $\alpha$  resulting from the interactions of slip systems  $\beta$  and  $\gamma$  is defined as:

$$n_{\alpha}^{\beta\gamma} = \begin{cases} 1 & \text{if } \mu b^{(\alpha)2} < \mu b^{(\beta)2} + \mu b^{(\gamma)2} \text{ and } b^{(\alpha)} = b^{(\beta)} + b^{(\gamma)} \\ 0 & \text{otherwise} \end{cases}. \quad (2.24)$$

The rates of junction formation on  $\alpha$  can then be defined as

$$n_{\alpha}^{\beta\gamma} f_0 \rho_m^{(\beta)} \rho_m^{(\gamma)} l_c v^{(\beta\gamma)} \text{ and } n_{\alpha}^{\beta\gamma} f_{\beta\gamma} l_c \left( \rho_m^{(\beta)} \rho_{im}^{(\gamma)} v^{(\beta)} + \rho_m^{(\gamma)} \rho_{im}^{(\beta)} v^{(\gamma)} \right) \quad (2.25)$$

for mobile/mobile and mobile/immobile interactions, respectively. From this, the total increase in mobile dislocations resulting from interactions becomes:

$$\begin{aligned} \dot{\rho}_{interaction+}^{(\alpha)} = & f_0 \sum_{\beta,\gamma} \left( \rho_m^{(\beta)} l_c \left( \frac{\dot{\gamma}^{(\gamma)}}{b^{(\gamma)}} \right) + \rho_m^{(\gamma)} l_c \left( \frac{\dot{\gamma}^{(\beta)}}{b^{(\beta)}} \right) \right) \\ & + f_0 \sum_{\beta,\gamma} \left( \rho_{im}^{(\beta)} l_c \left( \frac{\dot{\gamma}^{(\gamma)}}{b^{(\gamma)}} \right) + \rho_{im}^{(\gamma)} l_c \left( \frac{\dot{\gamma}^{(\beta)}}{b^{(\beta)}} \right) \right). \end{aligned} \quad (2.26)$$

Dislocation density annihilation from recovery is modeled using an Arrhenius relationship: (Rasmussen, et al. 2000)

$$\dot{\rho}_{annihilation}^{(\alpha)} = v^{(\alpha)} e^{\left( \frac{-H}{kT} \right)}. \quad (2.27)$$

where the frequency of immobile dislocations that are intersected by mobile dislocations on other slip systems is related to the attempt frequency,  $v^{(\alpha)}$ , as

$$v^{(\alpha)} = f_0 \sum_{\beta} \rho_{im}^{(\alpha)} l_c \left( \frac{\dot{\gamma}^{(\beta)}}{b^{(\beta)}} \right). \quad (2.28)$$

The activation enthalpy,  $H$ , is related to the immobile dislocation density and saturation density,  $\rho_s$ , as

$$H = H_0 \left( 1 - \sqrt{\frac{\rho_{im}^{(\alpha)}}{\rho_s}} \right) \quad (2.29)$$

The annihilation rate of dislocation densities on slip system  $\alpha$  becomes

$$\dot{\rho}_{annihilation} = \left( f_0 \sum_{\beta} \rho_{im}^{(\alpha)} l_c \left( \frac{\dot{\gamma}^{(\beta)}}{b^{(\beta)}} \right) \right) e^{-\frac{H}{kT}} \quad (2.30)$$

The generation, interaction, and annihilation rates are then substituted into Equations 2.17 and 2.18 to obtain a coupled nonlinear set of evolutionary equations for the dislocation densities. The evolutionary equations can be expressed as:

$$\frac{d\rho_m^\alpha}{dt} = |\dot{\gamma}^\alpha| \left( \frac{g_{sour}^\alpha}{b^2} \left( \frac{\rho_{im}^\alpha}{\rho_m^\alpha} \right) - g_{minter}^\alpha \rho_m^\alpha - \frac{g_{immob-}^\alpha}{b} \sqrt{\rho_{im}^\alpha} \right), \quad (2.31)$$

$$\frac{d\rho_{im}^\alpha}{dt} = |\dot{\gamma}^\alpha| \left( g_{minter+}^\alpha \rho_m^\alpha - \frac{g_{immob+}^\alpha}{b} \sqrt{\rho_{im}^\alpha} - g_{recov}^\alpha \rho_{im}^\alpha \right) \quad (2.32)$$

where  $g_{sour}$  is a coefficient pertaining to an increase in the mobile dislocation-density because of dislocation sources;  $g_{minter}$  is a coefficient related to the trapping of mobile dislocations because of forest intersections, cross-slip around obstacles, or dislocation interactions;  $g_{recov}$  is a coefficient for the rearrangement and annihilation of immobile dislocations; and  $g_{immob}$  is a coefficient for the immobilization of mobile dislocations.

### 2.3 Numerical Methods

The total deformation rate tensor,  $D_{ij}$ , and the plastic deformation rate tensor,  $D_{ij}^p$ , are needed to update the material stress state. Zikry developed the method used here for rate-dependent crystalline plasticity formulations, and only a brief outline will be presented here. For dynamic deformations, an explicit method is used with a lumped mass, four-point integration, and central-time-difference. To overcome numerical instabilities associated with stiffness that can occur because of large variations in slip rates, resolved shear stresses, and dislocations-densities, a hybrid explicit-implicit method is used to obtain the plastic deformation rate tensor,  $D_{ij}^p$ , and to update the evolutionary equations for the mobile and immobile dislocation densities. The hybrid method is based on using an explicit Runge-Kutta method, but is switched to an implicit Euler method when numerical stiffness is encountered.

### CHAPTER 3: VALIDATION WITH EXPERIMENTAL RESULTS

When developing methods for modeling twinned nanocrystalline aggregates, it was necessary to ensure that the simulation predictions were consistent with experimental data. To achieve this, experimental data was recreated using the twinned simulations (Figure 1). The three twinned cases presented by Shen et al. were used as the benchmark cases. In addition to simplifying the simulation by only focusing on one material, the experiments clearly showed the effects of varying percentages of twinned structures on the material responses to applied strain. The experimental specimens had been produced using the pulsed electro-deposition technique. No controlling methods for preferentially orienting the twin structures were used experimentally, so the Euler angles were chosen randomly for the material model simulations. (Shen, et al. 2005) Insights into specific material dynamics, including dislocation density evolution and areas of localized shear slip, were developed while ensuring conformance to experimental results.

Table 2 shows the material properties reported in the experimental work and Table 3 shows the material properties used to recreate the experiments. Table 3 also shows various parameters specific to the finite element simulation. The experimental and simulated results were consistent with one another. Material failure was not modeled, so hardening occurred indefinitely in simulation. This manifested itself in the stress-strain curve by a continuation in hardening beyond the experimental ultimate tensile yield stress.

Meshing was performed using Abaqus and mesh element sizes were generally on the order of 7,000-8,000 elements. These mesh sizes were found sufficient for convergence. The

only two material parameters that were modified between twin and parent materials were the slip system interaction coefficients and the slip systems themselves. The interaction coefficients were elevated in the twinned structures on the basis that experimental studies have found few dislocations residing within the twinned structures in the final strained state and that softness was observed near twin boundaries. (Shen, et al. 2005, Mirkhani and Joshi 2011) In addition to interaction coefficient modification, the slip systems in the twinned materials were modified in accordance with the work of Niewczas. (Niewczas 2007) The parent and twinned slip systems for f.c.c. materials can be found in Table 1. Symmetric boundary conditions were used for the bottom and left edges of the specimen, so that the modeled material consisted of the top right corner of a larger polycrystalline aggregate. Monotonic quasi-static loading was applied in the [001] direction. Using a framework developed in this manner, it was a relatively simple matter to control for such factors as twin volume fraction, grain size, twin thickness, grain (and twin) orientation, and grain misorientations.

### **3.1 Further examination of 19% Twin Volume Fraction Case**

The 19% twinned volume fraction (v.f.) case was selected for further examination. An image showing the specific grain shapes and twin lamella used in the simulation is shown in Figure 2. Random orientations were assigned to each grain and the twinned regions were oriented realistically with respect to the parent grains. Toughness values for the experimental and simulated cases were determined by calculating the area beneath the respective stress-

strain curves using a trapezoidal integration method. The simulation value of toughness for the 19% v.f. case was 3.99% greater than the experimentally derived value for toughness.

Contour maps of the resulting simulation were analyzed to further understand the effect of twins on the material aggregate. Figure 3 shows the dislocation density resulting from the  $[1\bar{1}1](110)$  parent/ $[1\bar{1}1](\bar{1}\bar{1}0)$  immobile slip system that was normalized by the initial dislocation density. In certain grains, it was evident that the orientation of the twins placed them in a position relative to the loading axis such that greater activity resulted in a higher dislocation density. In other grains, the parent material exhibited this trait. The only difference between individual grains was the material orientation, so it is understood that dislocation densities are dependent on grain orientation. This is significant because it highlights the effects of twinned structures on resulting dislocation density. Effectively, twins were modeled as small grains with different slip system orientations. This provided more opportunities for slip system activation compared with a homogeneously oriented material. This heterogeneous distribution of dislocations is consistent with experimental measurements. (Shen, et al. 2005) This effect will be utilized in Chapter 4 to produce further strengthening effects in simulation by preferentially orienting all grains within the material.

A contour map of lattice rotation for this material is shown in Figure 4. Rotation was generally higher in twinned materials than in other materials, and this feature differed per grain. Regions of high shear slip (Figure 5) also generally corresponded with regions of highly negative lattice rotation. Areas of high shear slip similarly were not strictly dependent on material type (twin or parent) and varied by grain.

The stress contour, shown in Figure 6, was uniform throughout the simulated material, with large regions of the material showing approximately five times the yield stress. There were also localized regions of high stress that corresponded with up to nine times the yield stress, and these occurred with greatest frequency near twin and grain boundaries, and particularly near triple junctions.

### **3.2 Conclusions**

Three twinned material experimental responses were successfully simulated, which validated the computational approach. The random orientations of the twinned structures had a significant effect on the distribution of stresses and dislocation-densities within the material. More significantly, this demonstrated that preferential orientations for twinned materials might exist.

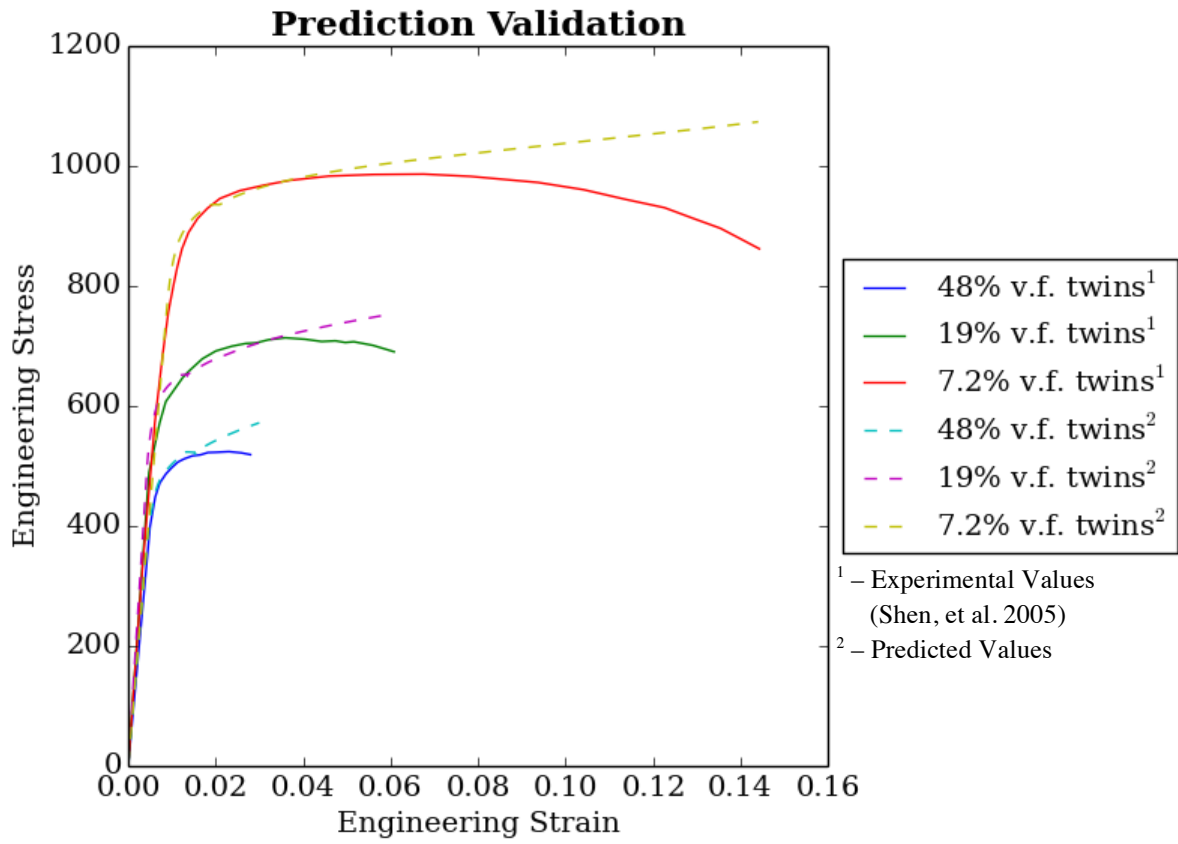


**Figure 1: Comparison of experimental and predicted stress-strain curves.**

**Table 1: Parent and equivalent twin slip systems**

Slip System Number	Parent Slip System	Equivalent Twin Slip System
1	$[111](\bar{1}01)$	$[\bar{1}\bar{1}\bar{1}](10\bar{1})$
2	$[111](\bar{1}10)$	$[\bar{1}\bar{1}\bar{1}](01\bar{1})$
3	$[111](0\bar{1}1)$	$[\bar{1}\bar{1}\bar{1}](1\bar{1}0)$
4	$[\bar{1}\bar{1}\bar{1}](011)$	$[200](0\bar{1}\bar{1})$
5	$[\bar{1}\bar{1}\bar{1}](\bar{1}10)$	$[200](01\bar{1})$
6	$[\bar{1}\bar{1}\bar{1}](101)$	$[200](0\bar{2}0)$
7	$[\bar{1}\bar{1}\bar{1}](101)$	$[00\bar{2}](0\bar{2}0)$
8	$[\bar{1}\bar{1}\bar{1}](110)$	$[00\bar{2}](\bar{1}\bar{1}0)$
9	$[\bar{1}\bar{1}\bar{1}](0\bar{1}1)$	$[00\bar{2}](1\bar{1}0)$
10	$[1\bar{1}\bar{1}](011)$	$[1\bar{1}\bar{1}](0\bar{1}\bar{1})$
11	$[1\bar{1}\bar{1}](110)$	$[1\bar{1}\bar{1}](\bar{1}\bar{1}0)$
12	$[1\bar{1}\bar{1}](\bar{1}01)$	$[1\bar{1}\bar{1}](10\bar{1})$

(Niewczas 2007)

**Table 2: Experimental microstructure description**

Microstructural Factors	Case A	Case B	Case C
<b>Grain Size</b>	450 nm	400 nm	400 nm
<b>Twin Volume Percentage</b>	48%	19%	7.2%
<b>Nominal Strain to Failure</b>	2.8%	6.1%	14.4%

(Shen, et al. 2005)

**Table 3: Simulation parameters**

<b>Parameter</b>	<b>Case A: 48% v.f.</b>	<b>Case B: 19% v.f.</b>	<b>Case C: 7.2% v.f.</b>
<b>Yield Stress</b>	125 MPa	165 MPa	300 MPa
<b>Modulus of Elasticity</b>	103 GPa	103 GPa	77.2 GPa
<b>Grain Size</b>	450 nm	400 nm	400 nm
<b>Twin Volume Percentage</b>	44.2%	20.7%	6.92%
<b>Strain Rate</b>	$1.88 \times 10^{-3} \text{ s}^{-1}$	$1.88 \times 10^{-3} \text{ s}^{-1}$	$1.88 \times 10^{-3} \text{ s}^{-1}$
<b>Taylor Coefficients</b>	0.3 Twin / 0.07 Parent	0.3 Twin / 0.07 Parent	0.3 Twin / 0.07 Parent
<b>Nominal Strain to Failure</b>	2.8%	6.1%	14.4%
<b>Mesh Size (elements)</b>	6,833	7,032	10,345
<b>Number of Grains</b>	9	9	9

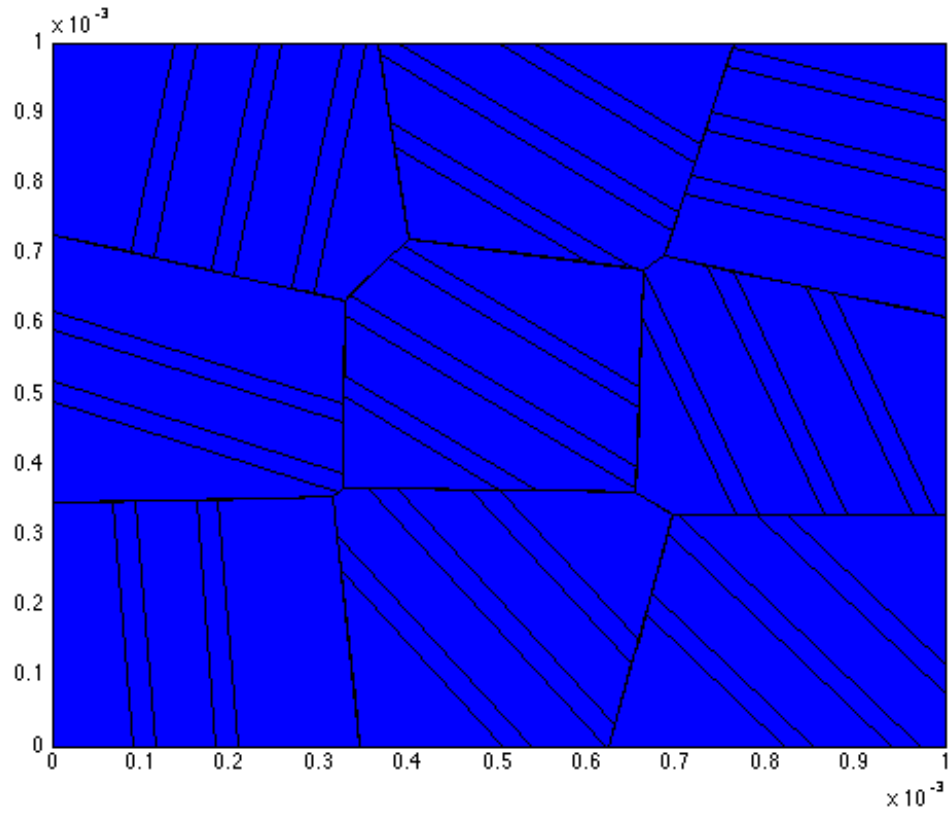


**Figure 2: Representative material featuring randomized grains and twin lamella.  
(Spatial dimensions are in meters)**

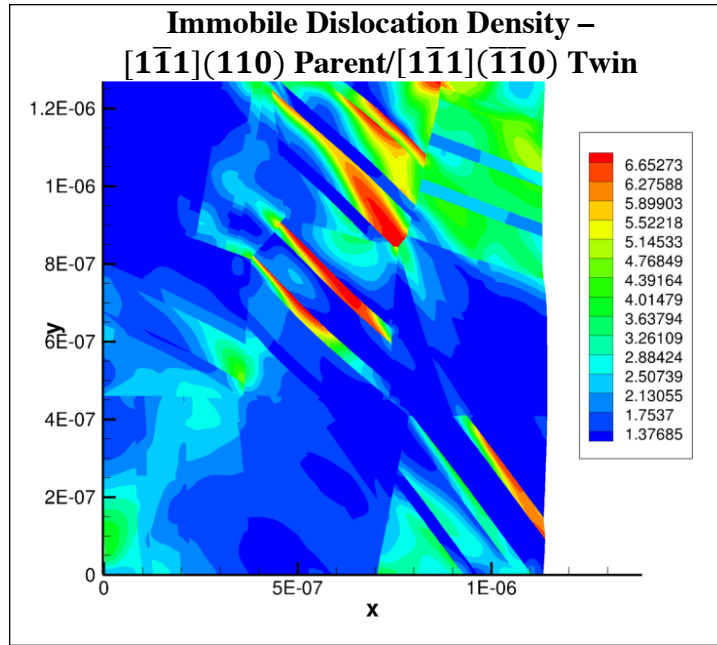


**Figure 3: Normalized dislocation density values from one slip system. (Spatial dimensions are meters)**

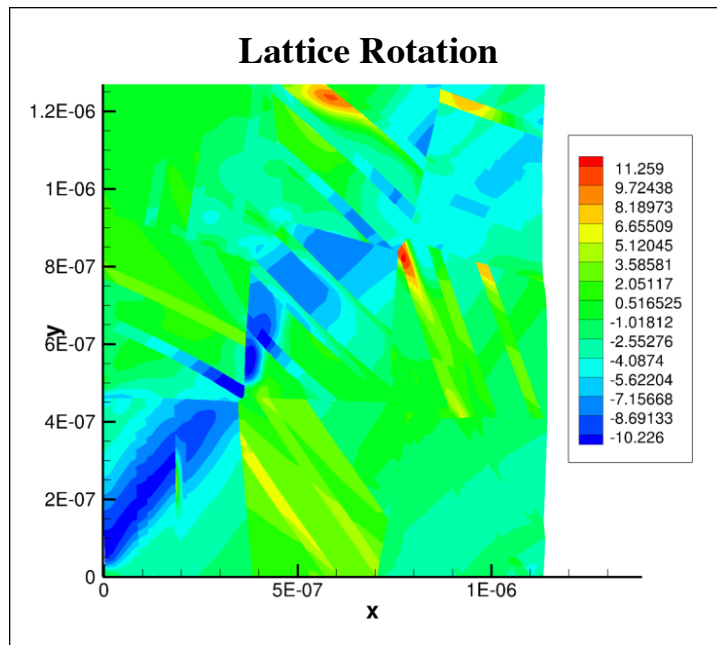


**Figure 4: Lattice rotation at terminal strain showing that twinned regions have an effect on local rotation. (Spatial dimensions are meters)**

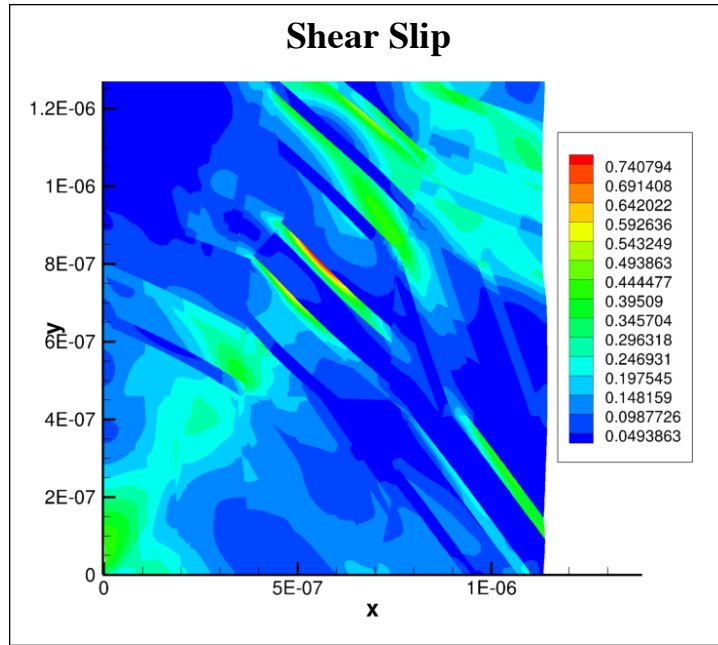


**Figure 5: Shear slip in the material appears localized in either the twinned or parent material, depending on grain orientation. (Spatial dimensions are meters)**

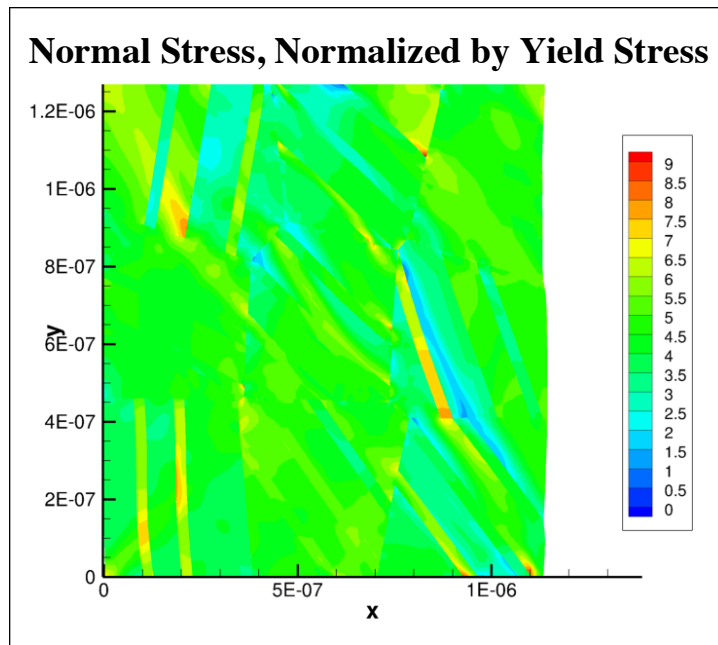


**Figure 6: Stress distribution in the material, normalized by the yield stress. (Spatial dimensions are meters)**

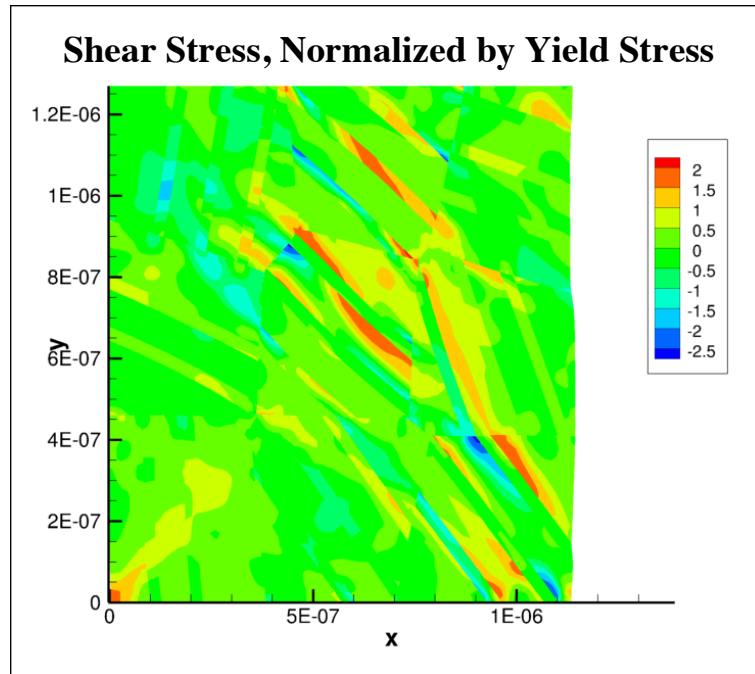


**Figure 7: Normalized shear stress. (Spatial dimensions are meters)**

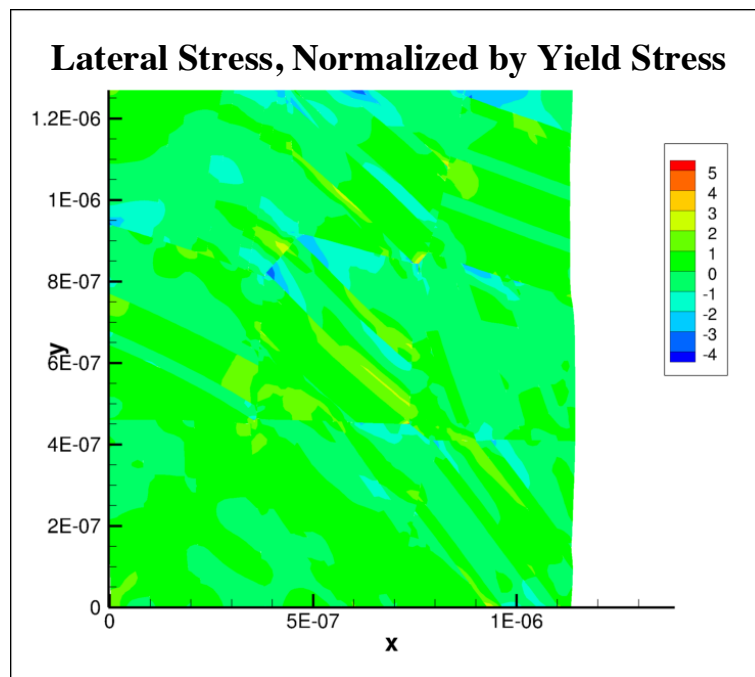


**Figure 8: Normalized lateral stress. (Spatial dimensions are meters)**

## CHAPTER 4: ORIENTATION EFFECTS ON TWINNED AGGREGATES

To further understand the effects of the twin addition to materials, the effects of orientation on twinned materials were quantified. To do this, the simulation designed to model the 19% v.f. case was modified to orient the grains so that the twin structures would be at seven specific angles with respect to the loading axis. No other material properties were modified. Because randomized Voronoi tessellations were used to create the figures, slight variations in microstructure geometry occurred. However, the average grain sizes were maintained at values consistent with experimental results. Simulations at each orientation with no twin structures were also performed. Up to  $10^\circ$  of misorientation were incorporated into the grain orientations to create a realistic representation of a preferentially oriented polycrystalline grain structure.

The goal for this phase of the research was to control for as many variables as possible while modifying the grain structure so that the materials would be preferentially oriented in one of seven directions. These directions were  $0^\circ$ ,  $15^\circ$ ,  $30^\circ$ ,  $45^\circ$ ,  $60^\circ$ ,  $75^\circ$ , and  $90^\circ$ . Only the Euler angle that controlled orientation in one direction perpendicular to the loading axis of the material was varied. The other two angles remained at  $0^\circ$ . Misorientations were incorporated so that a maximum of  $10^\circ$  of misorientation would be possible between neighboring grains. For example, in the  $30^\circ$  simulation, grain orientations were randomly chosen so that the twins would be oriented between  $25^\circ$  and  $35^\circ$  with respect to the horizontal axis. Figure 9 shows a sample grain structure with  $30^\circ$  orientation.

#### **4.1 Mesh Convergence**

The original mesh in the 45° simulation contained 7,657 elements. To ensure that mesh convergence had occurred, a new mesh with the same material shapes was created with 10,386 elements. These meshes are both shown in Figure 10. Figure 11 additionally shows the stress responses for both simulations. The material toughness and stress at terminal strain for the refined simulation were both 1.40% greater than the original values. Based on this analysis, the use of meshes within the 7,000-8,000 element range was deemed acceptable.

#### **4.2 Grain Aggregate Size**

All of the modeling simulations in this work were produced with 9-grain models created using Voronoi tessellations. Having boundary conditions on the left and bottom sides effectively turned the model into a two-way symmetric 36-grain representative material. To ensure that grain count was representative of a much larger aggregate, a 16-grain model was created using equivalent properties and orientations to the 0° orientation run described earlier. This effectively produced a 64-grain aggregate because of symmetry conditions. Similar stress-strain responses were noted between the higher grain count aggregate and the lower grain count aggregate, as shown in Figure 12.

#### **4.3 Comparison of Stress-Strain Responses**

Figure 13 shows the resulting stress-strain curves comparing the 19% v.f. case with the aforementioned simulations of preferentially oriented twins. Initial examination indicates a strong dependence on orientation for twinned materials. It appears that any preferential orientation produces a stronger material than the experimental case, where grains were

randomly oriented, and that the 45° simulation in particular has the greatest potential for material strengthening. It bears noting that Figure 13 does not incorporate the responses of the equivalent preferentially oriented non-twinned material at each orientation. To further understand and quantify the differences between twinned and non-twinned materials at each preferred orientation angle, the toughness values for each simulation were determined. These are presented in Figure 14. The dotted blue line represents the experimentally derived toughness of the benchmark 19% v.f. case, which had no preferred orientation. All twinned simulations exhibited higher toughness than the experimental case. One possible concern is that the comparison between the experimental case and simulated cases with no failure modeling may not be accurate, but it should also be noted that the difference between the toughness values of the experimental case and the randomized benchmark simulation was only 4%, and that many of the conclusions that follow are based solely on a comparison of variables from non-twinned material simulations and twinned material simulations, both of which used no failure modeling.

To understand the modeling results, the percentage differences between toughness values for the twinned and non-twinned simulations were compared. This provided an indication of exactly how much strength increase occurs when twins of the thickness and volume fraction used in the 19% v.f. case were introduced to a material, and what dependence on twin orientation this may have. Figure 15 shows this information. It is apparent that a pattern exists between orientation and percentage toughness increase compared with the non-twinned simulations. Contrary to what the information in Figure 13 may appear to suggest, the greatest advantage in the use of twinned materials appears to be

their reinforcement of the material at low and high angle orientations. The material toughness decreased in the twinned simulation when compared with the non-twinned analog at 45°. For further clarification, the stress-strain curves for this simulation are shown in Figure 16. The yield point in the twinned simulation was lower than that of the non-twinned counterpart, but the average stress at the terminal strain of the benchmark case was higher in the twinned case than in the non-twinned case. Conclusions regarding ductility in the twinned and non-twinned material cannot be made because failure was not modeled, but parameters such as shear slip may allude towards material ductile capability, and these will be discussed later in the text.

#### **4.4 Dislocation Density Evolution**

Dislocation activity plays a broad role in material response to strain. To characterize the effect of individual slip systems on the toughness response of twinned materials, the aggregate dislocation density in each material was taken per slip system and compared with material toughness. These values were then compared with non-twinned simulations to determine the changes in these material parameters when the material was subjected to twinning. The goal was to determine if the activation of certain slip systems at particular orientations was related to the resulting toughness of the material. Many slip systems showed no meaningful relationship in these areas, but there were noteworthy exceptions that appear in Figures 17-20. For these slip systems, it is clear that grain orientation (and therefore slip system orientation) with respect to the loading axis strongly influenced slip system activation, which in turn may have contributed to increases in toughness. The  $[\bar{1}\bar{1}1](101)$

parent/ $[200](0\bar{2}0)$  twinned immobile slip system displayed some positive relationship with toughness percent increase, as did the  $[\bar{1}11](110)$  parent/ $[00\bar{2}](\bar{1}\bar{1}0)$  immobile slip system. These two plots are shown as Figure 17 and Figure 18. Representations of mobile dislocations on slip systems tended to decrease with increasing toughness wherever discernable patterns existed. Figure 19 and Figure 20 show the  $[\bar{1}11](0\bar{1}1)$  parent/ $[00\bar{2}](1\bar{1}0)$  twinned mobile slip system and the  $[1\bar{1}1](011)$  parent/ $[1\bar{1}1](0\bar{1}\bar{1})$  twinned mobile slip system, where grain orientations that resulted in a reduction in aggregate mobile dislocation density compared with the respective non-twinned simulation generally had higher percent changes in toughness than did the orientations that resulted in higher aggregate mobile dislocation densities.

Figure 21 was generated using values for the aggregate immobile dislocation density summed over every slip system of each material. The motivation was to determine if immobile dislocation densities, irrespective of slip system, were dominant factors in determining the toughness of a material. This information was plotted with the percentage change in material toughness between the twinned and a similar non-twinned material as a dependent variable. Information from both twinned and the equivalent non-twinned materials were compared to form a percent change in aggregate immobile dislocation density at each orientation. The plot strongly suggests that the general immobilization of dislocations within the material leads to a relative increase in toughness compared with a non-twinned material. This is of significance because it suggests that twin lamella affect the aggregate material immobile dislocation density, which can in turn impact toughness.

It was projected that mobile dislocation densities may also influence material toughness. Figure 22 shows an aggregate similar to that presented for immobile dislocations, and a similar relationship was found between aggregate mobile dislocation density and the percentage increase in toughness. Essentially, mobile dislocation densities should remain similar to those of the non-twinned materials for higher material toughness values. The twinned material with the greatest negative percent change in mobile dislocation density was the 45° case, which was also the material with minimal change in toughness and greatest decrease in shear slip compared with the similar non-twinned case. This is largely consistent with dislocation theory, which indicates that immobilizing dislocations is advantageous to material strength. (You, Lu and Lu 2011)

To visually understand the specific roles of dislocations in twinned systems, the dislocation densities across all slip systems in each material simulation at the terminal strain were summed and presented in contour plots. Figure 23 shows the summed immobile slip systems in twinned and non-twinned simulations, and Figure 24 shows the summed mobile slip systems in twinned and non-twinned simulations. The maximum values for immobile dislocation density in twinned materials were unilaterally higher than those for non-twinned materials. For information on aggregate immobile dislocation density, the reader may recall Figure 21, where all twinned materials were shown to benefit from an increase in immobile dislocation densities. This is significant because the contours in Figure 23 show that the twinned materials have generally lower immobile dislocation densities when compared with the parent material surrounding the twin lamella. At 30°, 60°, and 75°, immobile dislocation densities were concentrated near twin boundaries, particularly on the side of the parent

material. This is consistent with experimental evidence that describes pileups at twin-parent boundaries. (Shen, et al. 2005) The maximum values of mobile dislocation density across all materials were lower than those of the non-twinned materials, indicating the tendency of twinned materials to convert mobile dislocations to immobile dislocations as a result of the higher percentage of internal boundaries.

Further investigation into individual slip systems is shown in Figure 25 and Figure 26. Figure 25 shows immobile dislocation densities for the  $[\bar{1}\bar{1}1](101)$  parent/ $[200](0\bar{2}0)$  twin slip system as contour maps for  $0^\circ$ ,  $15^\circ$ ,  $30^\circ$ ,  $45^\circ$ ,  $60^\circ$ ,  $75^\circ$  and  $90^\circ$  grain orientations. All twinned simulations present higher maximum values compared with non-twinned simulations, and Figure 17 shows that all twinned simulations that had increases in toughening also had increases in immobile dislocation density for this slip system. The contours also show that this particular slip system was most concentrated at triple junctions formed by grain and twin boundaries as opposed to higher concentrations along the length of the twin boundaries. The twins broke up the distributions that would otherwise be uniform in a non-twinned material with equivalent parent grain orientations.

Contours for the  $[1\bar{1}1](011)$  parent/ $[1\bar{1}1](0\bar{1}\bar{1})$  twin slip system are shown in Figure 26. This slip system is significant because activation in the twinned and parent materials differ greatly from one another. At low orientations (i.e.  $0^\circ - 15^\circ$ ), the twin lamellas had mostly higher activation than the surrounding parent material, but overall activation within the material was reduced compared with the non-twinned simulation. At  $30^\circ$  and  $45^\circ$ , the twin lamellas had higher activation than the surrounding parent material, and this was reflected in the non-twinned material, where low activation occurred. At  $60^\circ$ , however, both

twinned and non-twinned materials both had generally lower slip system activation. This trend reversed at  $75^\circ$ , and higher slip system activation, mostly in the parent regions, occurred. The non-twinned material model showed a similar increase. This slip system is an example of how heavily dependent slip system activation is on orientation.

#### **4.5 Lattice Rotation, Shear Slip, and Stress Buildup**

Lattice rotation contours are shown in Figure 27. It is interesting to note that at  $45^\circ$  orientation, the twinned regions exhibited greater lattice rotation than the surrounding areas, whereas at other orientations, the twinned regions had less rotation. The same pattern existed for shear slip, which is shown in Figure 28, which indicates that the twinned regions may be primarily responsible for the reduction in toughening at the  $45^\circ$  orientation. Shear slip buildup at twin boundaries also occurred, particularly at the  $60^\circ$  orientation. Aggregate shear slip in twinned and non-twinned simulations was also compared in the same manner that dislocation densities were in Figure 29. A sharp reduction in aggregate shear slip appeared to occur for the same orientations that experienced less toughening, in particular  $45^\circ$ . It would appear that higher shear slip within the twin lamella impacted the parent regions to reduce the aggregate values for shear slip.

Normal stresses in the loading direction for twinned and non-twinned materials at different orientations are shown in Figure 30. At lower orientation angles, the twins made little disruption in the material, but as the orientation angle increased, the twins had a greater impact on the contour. At all orientations, the twinned materials had greater maximum stresses compared with the non-twinned materials. At  $45^\circ$  and  $60^\circ$ , the twin lamellas

appeared to relieve stress. The stresses within these contours were additionally analyzed in the same manner as the dislocation densities earlier. Aggregate sums of stresses across the entire material were compared between non-twinned and twinned materials. The results are shown in Figure 31, which shows that a positive percentage increase in stress occurred in all twinned materials, and that the general pattern of stress increase by orientation followed that of toughness shown in Figure 15.

Lateral stress is shown in Figure 32. The general trends in lateral stress were similar to those found in normal stress. No discernible patterns were found amongst the twinned materials. A similar conclusion can be reached upon examination of the shear stress in Figure 33. Buildups in shear stress can be seen at the twin boundaries and maximum shear stress values were unilaterally higher in the twinned materials as opposed to the non-twinned materials. This was likely a result of the higher dislocation activity in those areas.

#### **4.6 Predictions of Twinned Materials under Compression**

The orientation predictions were reevaluated under compression instead of tension. All simulation parameters, including mesh and shape, remained the same. The absolute value of the final nominal strain also remained constant. The results led to the same general conclusions as those from the simulations with tensile loading, with similar but slightly different values for toughness. Figure 34 shows a comparison between twinned and non-twinned simulations for compressive loading toughness at each orientation, along with the randomly oriented twinned baseline. Figure 35 shows the percent difference between twinned and non-twinned simulations at each orientation. All orientations have improved toughness

compared with the original randomly oriented twinned simulation, with the greatest difference in percent toughness between twinned and non-twinned simulations occurring at low and high angle orientations.

#### **4.7 Conclusions**

It is clear that the activation of immobile slip systems is a contributing factor to the strengthening found in twinned materials. The provided contour plots support this by showing the activity in certain slip systems in which twinned materials produce different results when compared with non-twinned materials. Additionally, values for aggregate mobile and immobile dislocation density were related with material toughness. Most importantly, it is clear that the effect of twins on the parent material is a direct result of the twin orientation with respect to the loading axis. This implies that the potential of twins to strengthen engineered materials exceeds that recorded in current experimental results, where little is known about twin orientation control in bulk materials. The conclusions provide guidance for significant improvements to toughness and strength in nanocrystalline-twinned materials.

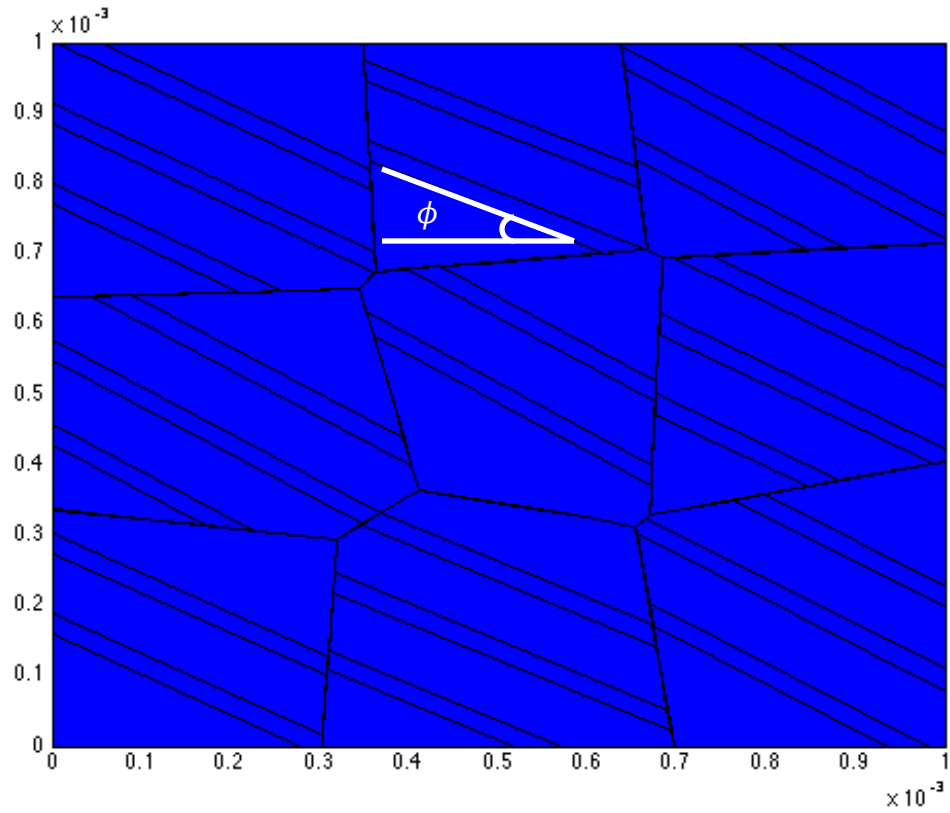


**Figure 9: Example of a  $30^\circ$  oriented twinned structure.  $\phi = 30^\circ \pm 10^\circ$ . (Spatial units are in meters)**

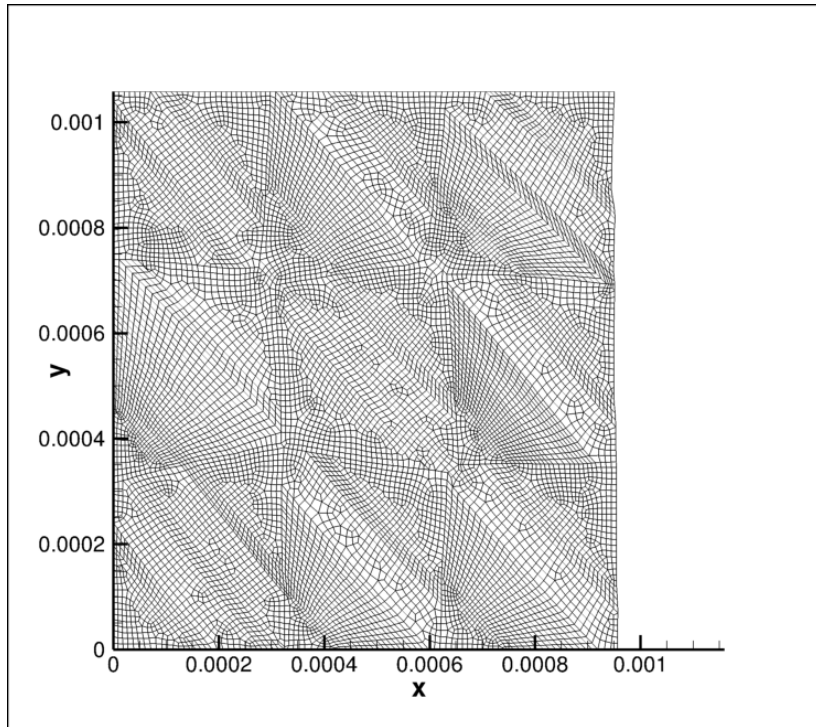
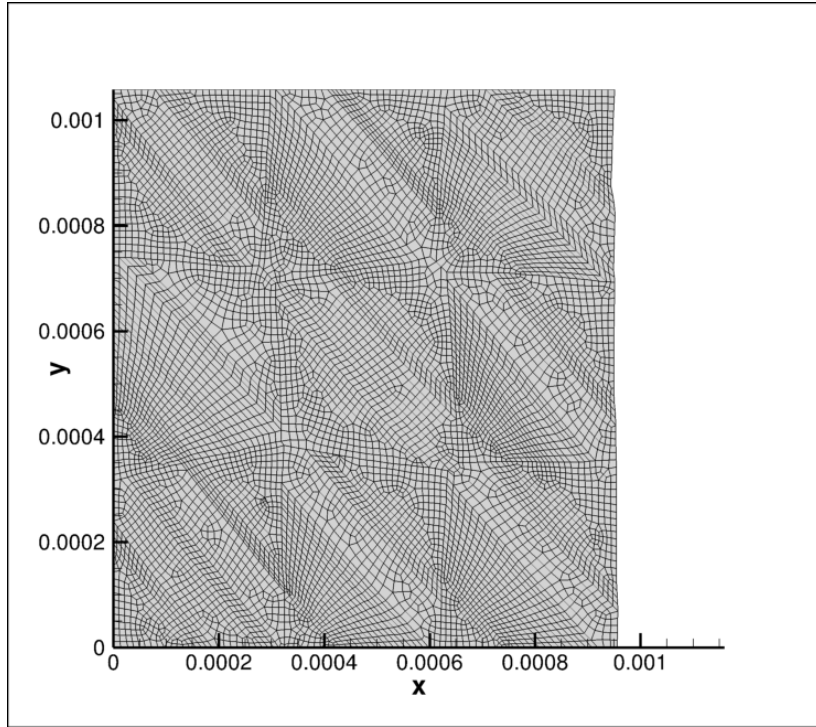


**Figure 10: Normal mesh density (top) and refined mesh (bottom)**

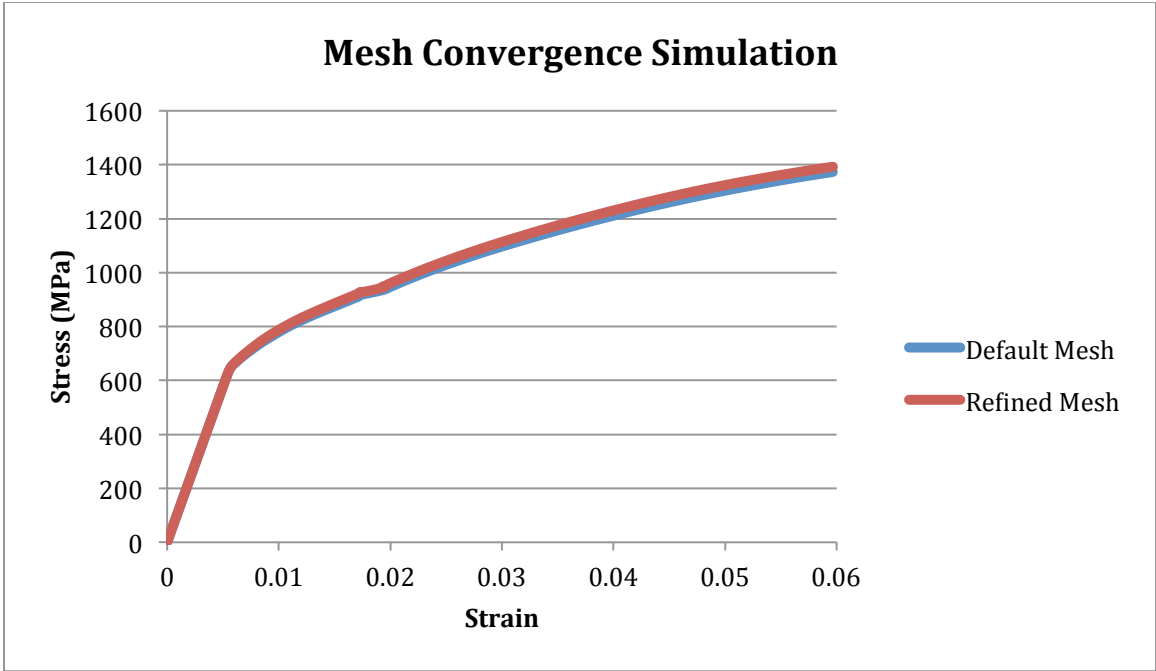


**Figure 11: Mesh convergence in 45° simulation.**

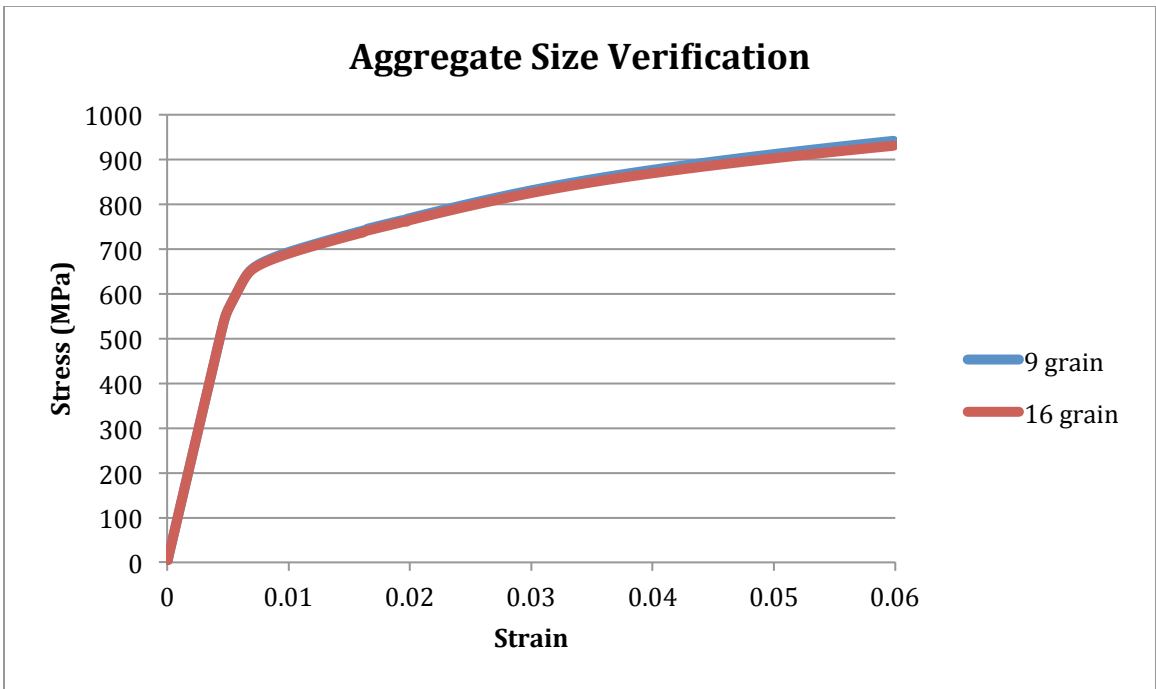


**Figure 12: Comparison of 9-grain and 16-grain simulated results.**

### Strength Dependence on Orientation

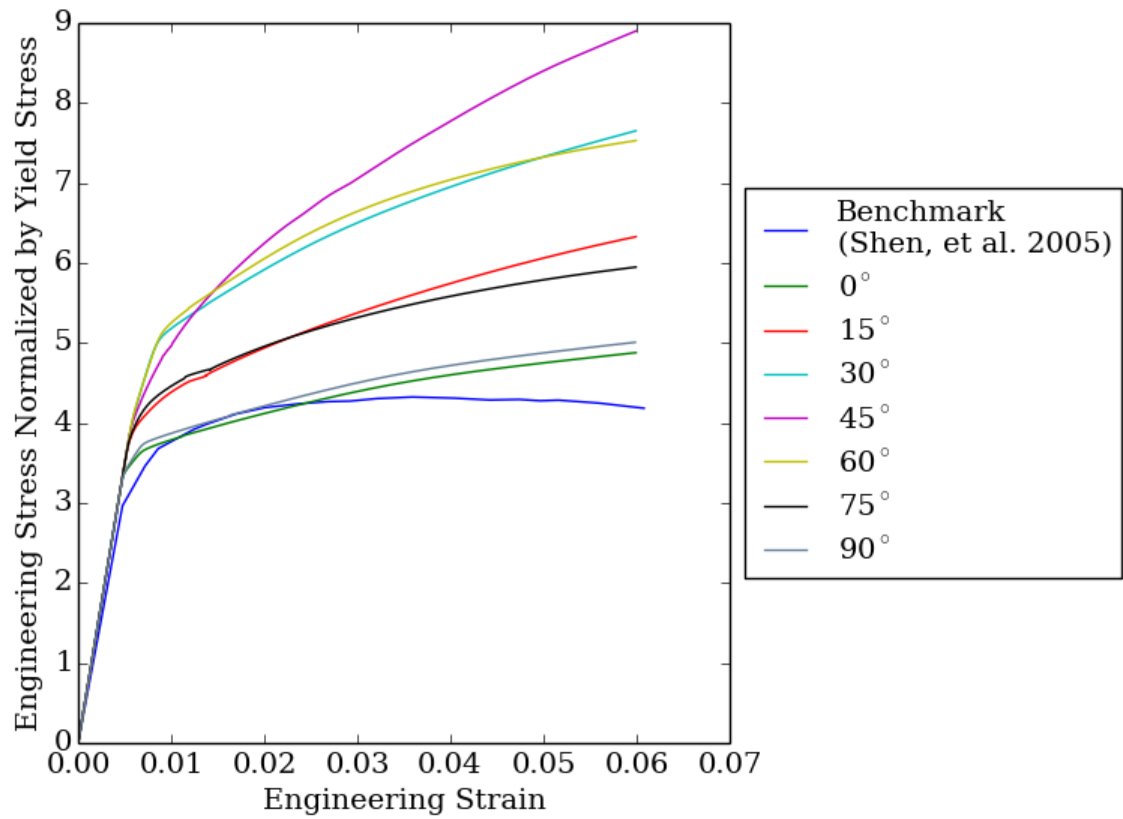
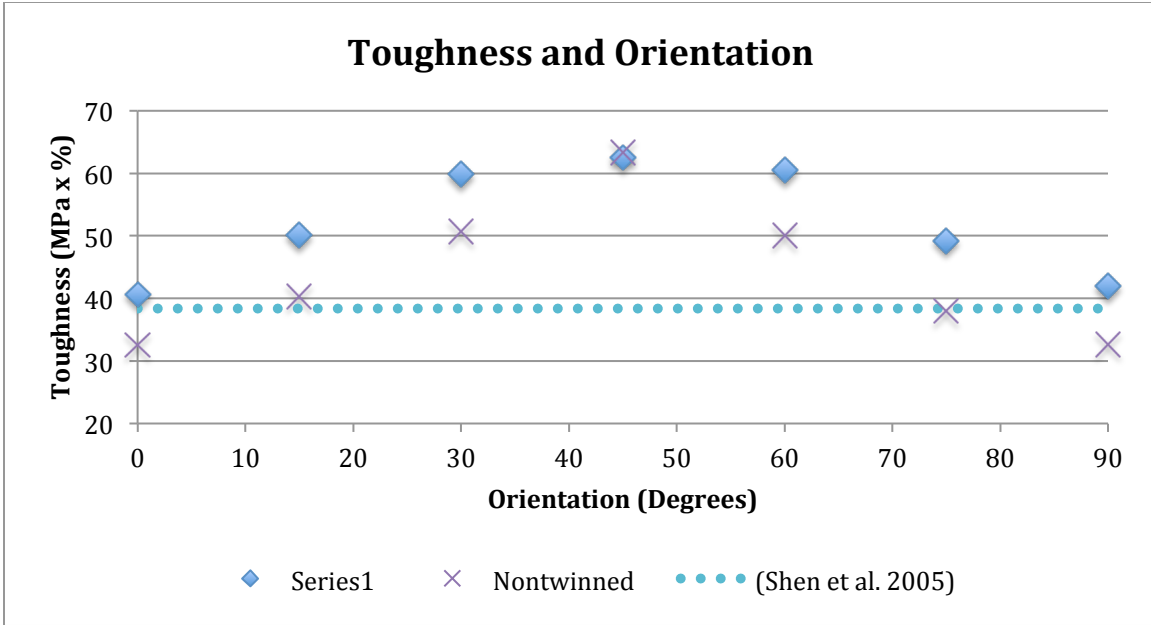
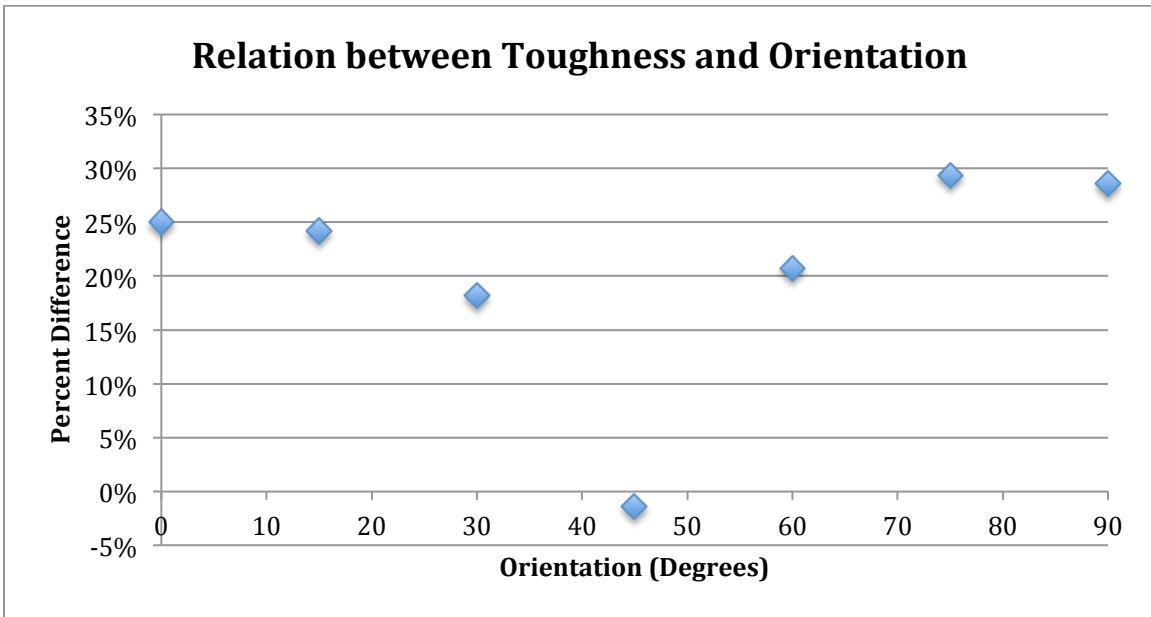


Figure 13: Stress-strain curves comparison of 19% v.f. simulation experimental results and orientation results



**Figure 14: Twinned and non-twinned material responses quantified in the form of toughness. Toughness was determined at the experimentally observed nominal failure strain.**



**Figure 15: Percentage increase in toughness between twinned and non-twinned simulations.**

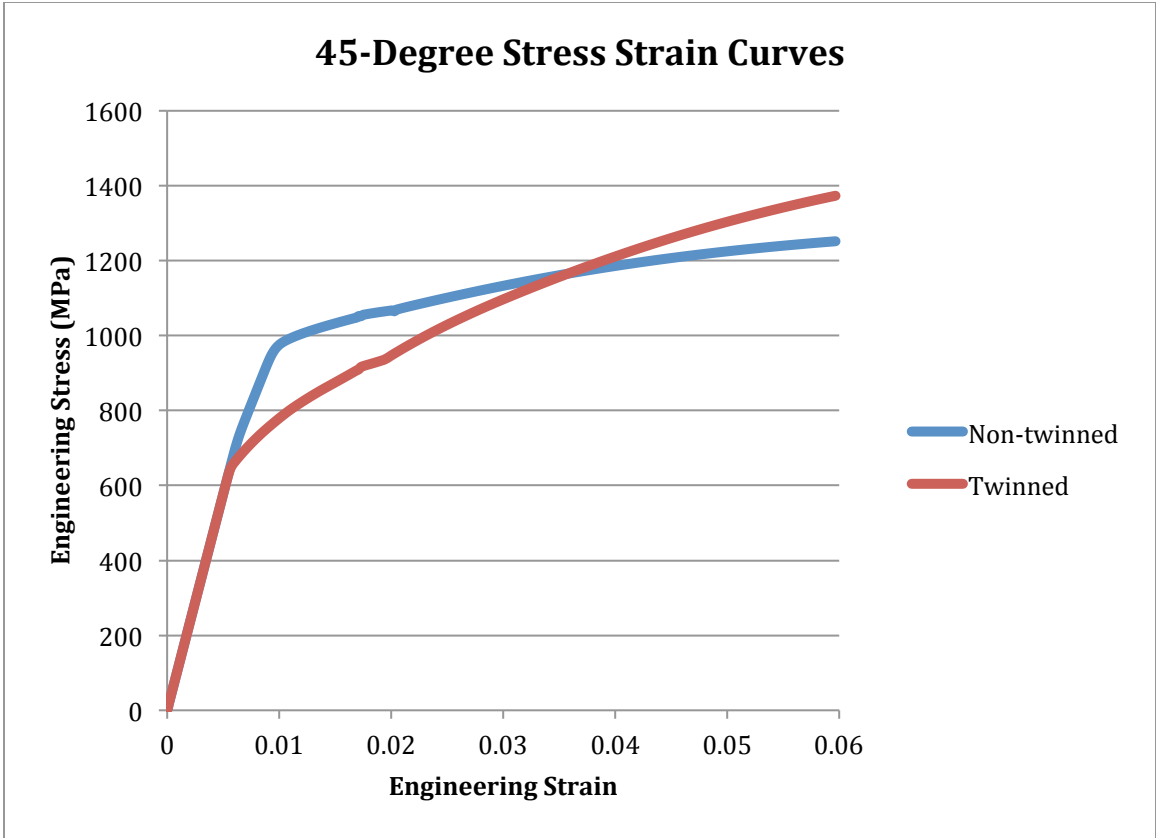


**Figure 16: Stress-strain curves for the twinned and non-twinned versions of the 45° material.**

**Immobile Dislocation Density Percent Change for  $[\bar{1}\bar{1}\bar{1}](101)$   
non-twinned/ $[200](0\bar{2}0)$  twinned slip system**

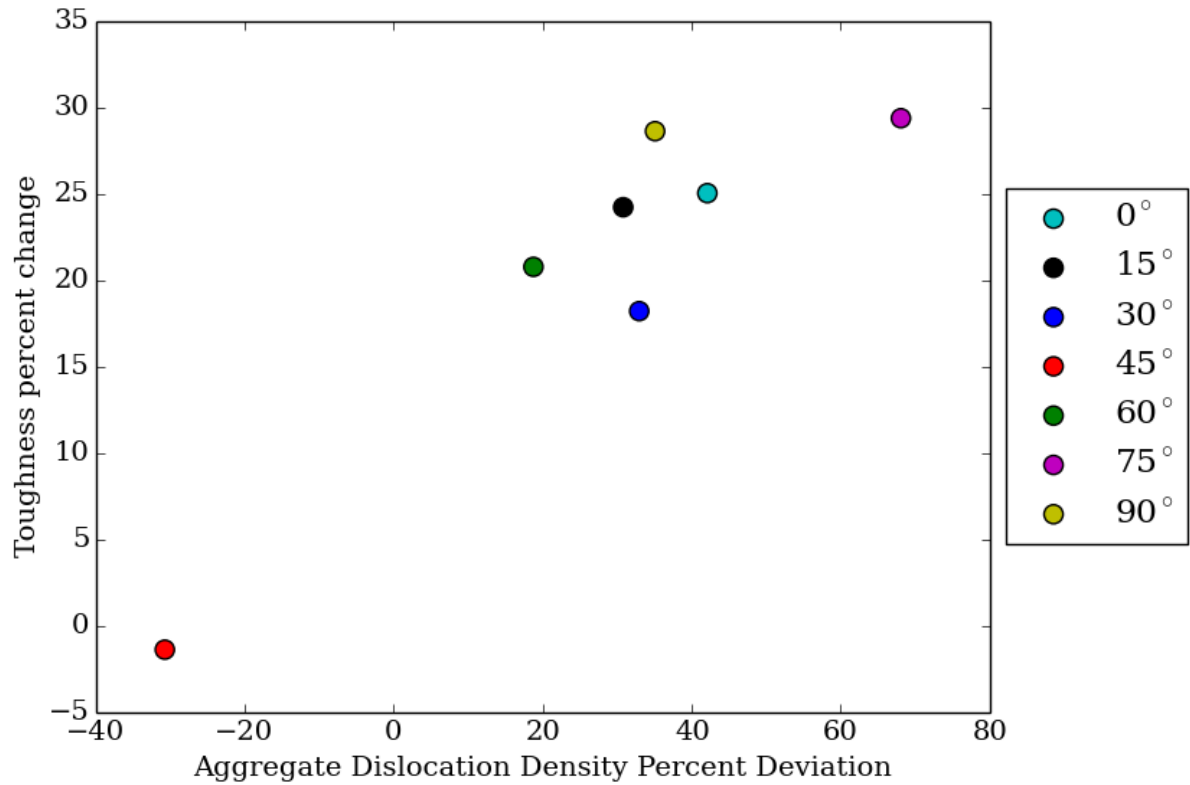


**Figure 17: Correlation between twinned percent deviation in immobile dislocation density and toughness percent change for the  $[\bar{1}\bar{1}\bar{1}](101)$  parent slip system and the  $[200](0\bar{2}0)$  twin slip system.**

**Immobile Dislocation Density Percent Change for  $[\bar{1}11](110)$   
non-twinned/ $[00\bar{2}](\bar{1}\bar{1}0)$  twinned slip system**

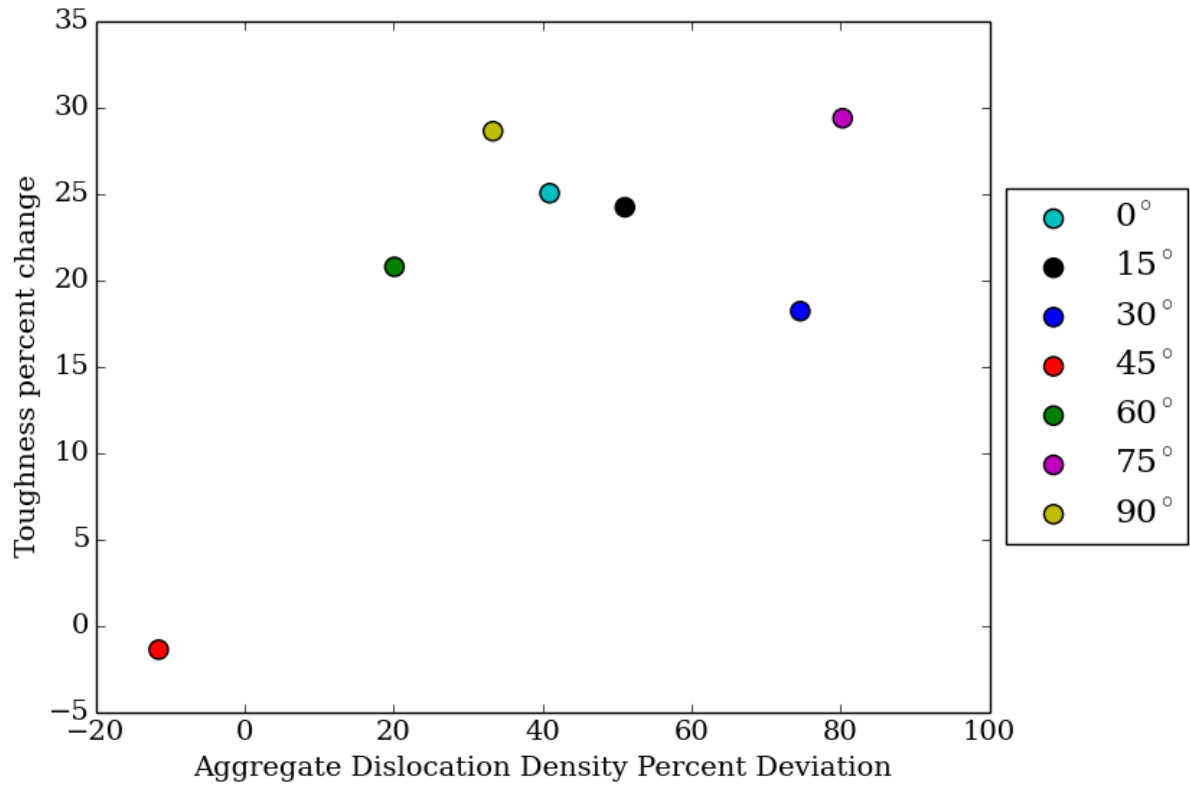


**Figure 18: Correlation between twinned percent deviation in immobile dislocation density and toughness percent change for the  $[\bar{1}11](110)$  parent slip system and the  $[00\bar{2}](\bar{1}\bar{1}0)$  twin slip system.**

**Mobile Dislocation Density Percent Change for  $[\bar{1}11](0\bar{1}1)$  non-twinned/ $[00\bar{2}](1\bar{1}0)$  twinned slip system**

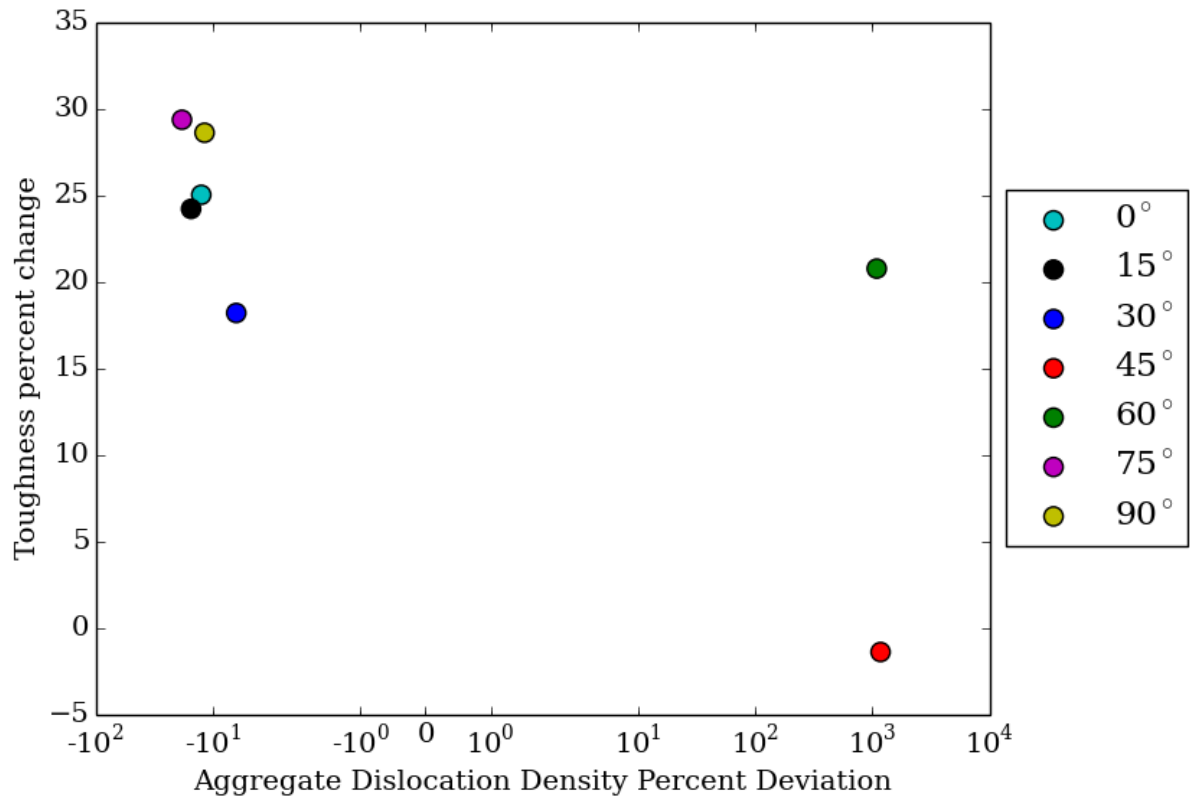


**Figure 19: Relation between twinned percent deviation in mobile dislocation density and toughness percent change for the  $[\bar{1}11](0\bar{1}1)$  parent slip system and the  $[00\bar{2}](1\bar{1}0)$  twin slip system.**

**Mobile Dislocation Density Percent Change for  $[\bar{1}\bar{1}1](011)$  non-twinned/ $[\bar{1}\bar{1}1](0\bar{1}\bar{1})$  twinned slip system**

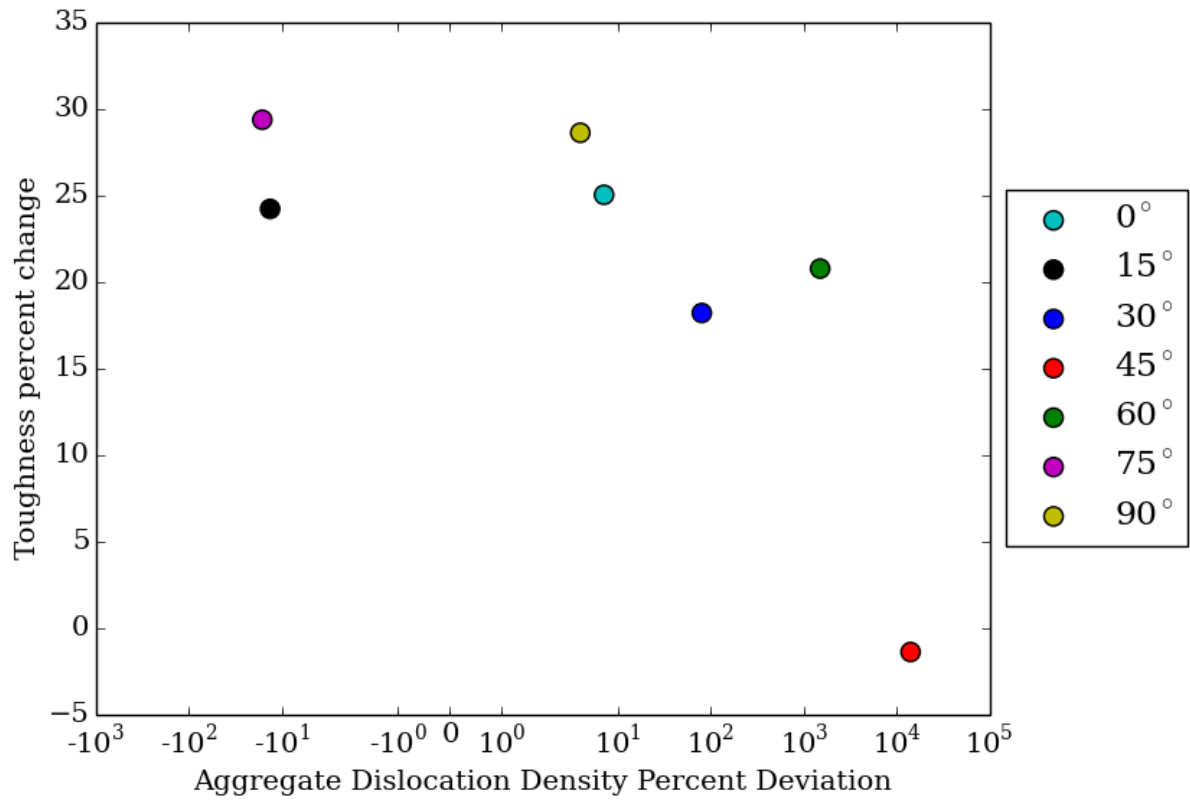


**Figure 20: Correlation between twinned percent deviation in mobile dislocation density and toughness percent change for the  $[\bar{1}\bar{1}1](011)$  parent slip system and the  $[\bar{1}\bar{1}1](0\bar{1}\bar{1})$  twin slip system.**

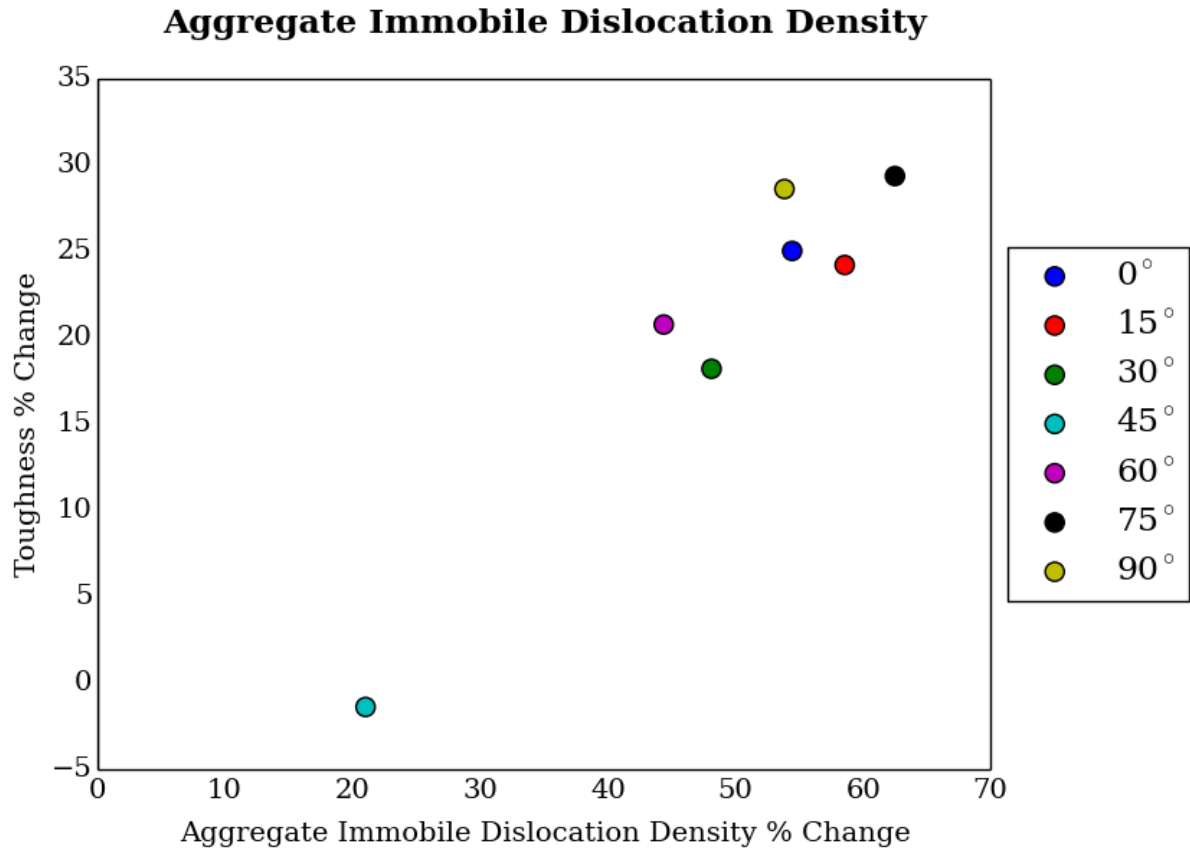


**Figure 21: Aggregate immobile dislocation density percent change compared with percent changes in toughness values for twinned materials and their non-twinned counterparts.**

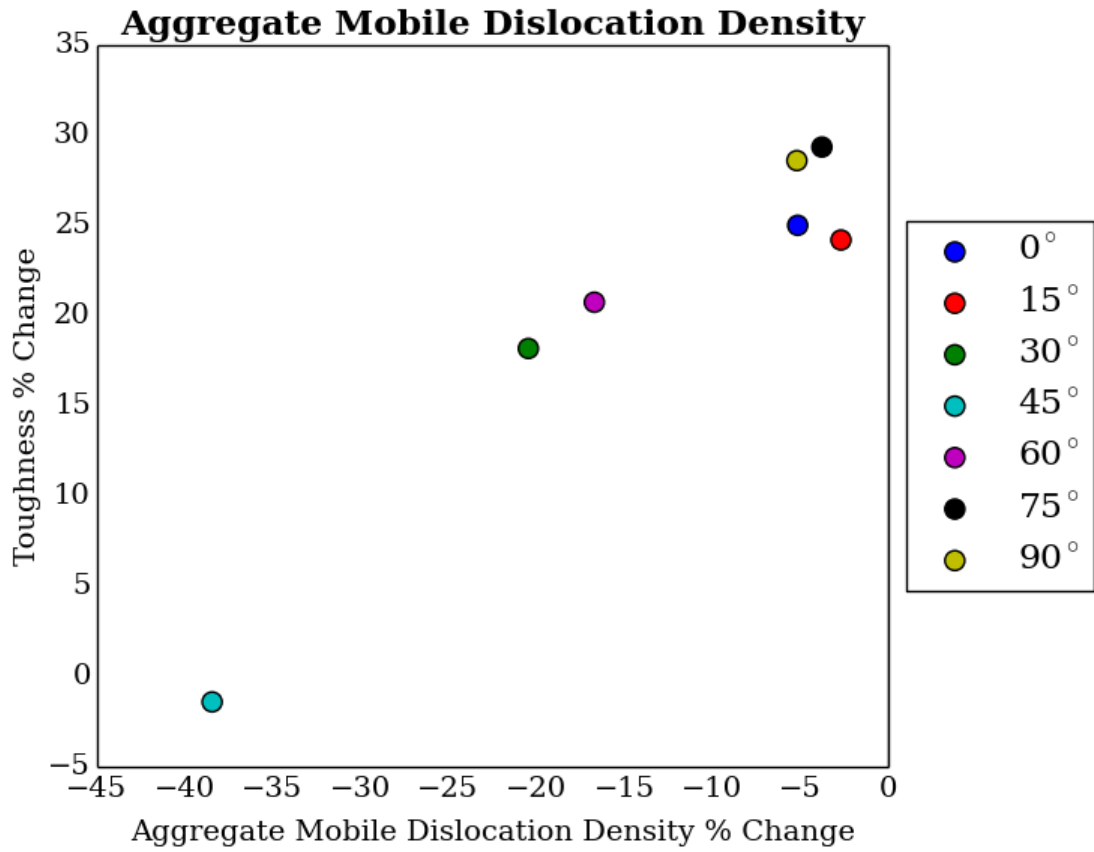
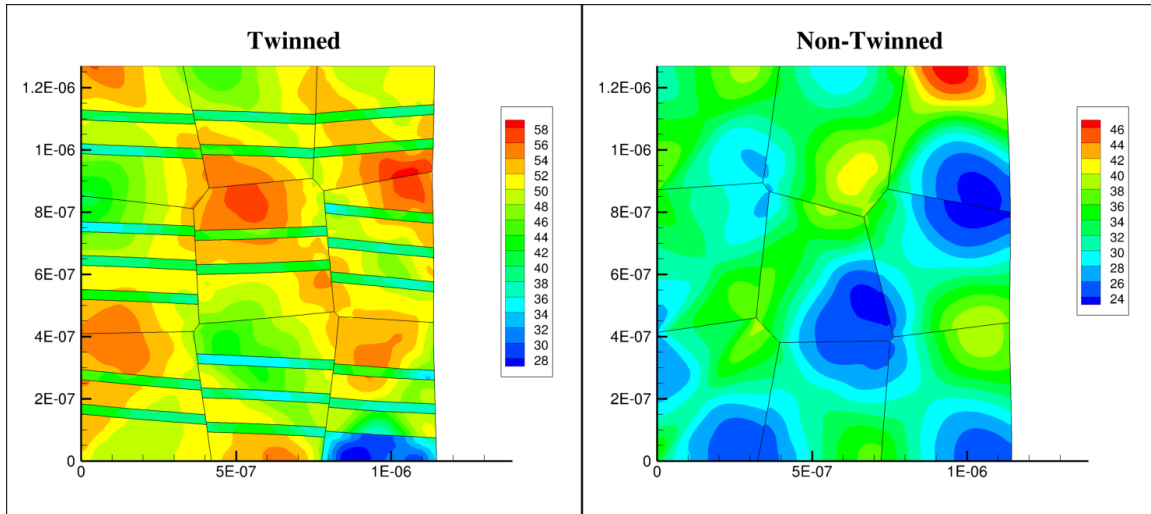


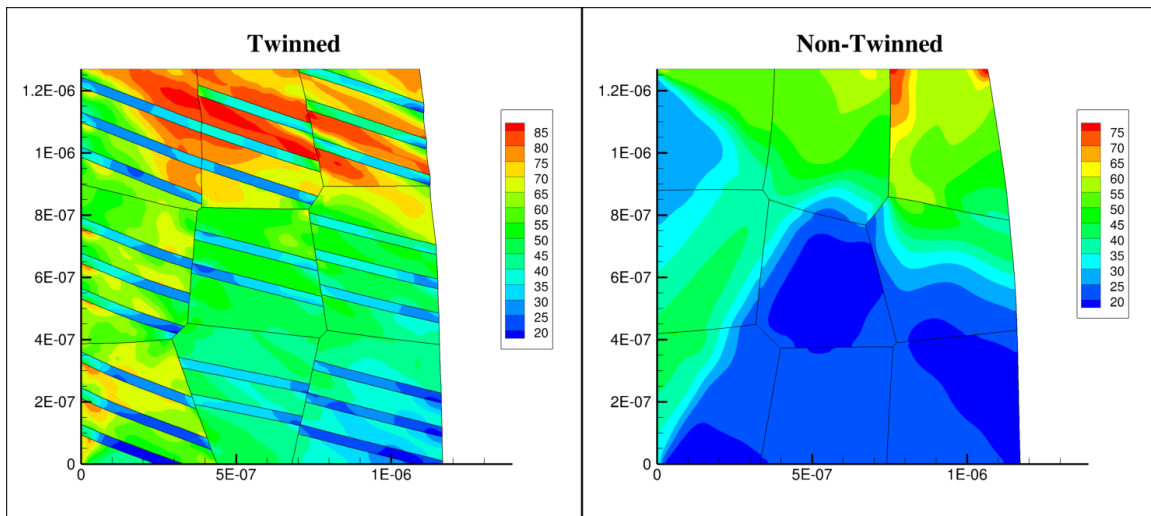
**Figure 22: Aggregate mobile dislocation density percent change compared with percent changes in toughness values for twinned materials and their non-twinned counterparts.**

**Figure 23: Total immobile dislocation densities summed over all slip systems. All spatial units are in meters. Dislocation densities are normalized by their initial values.**

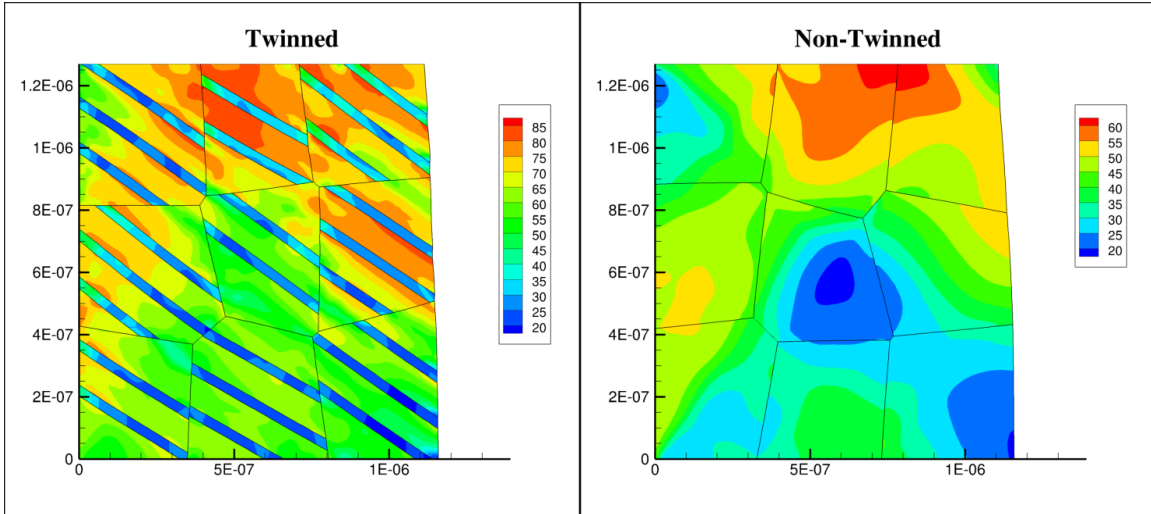
## 0° Orientation Total Immobile Dislocation Density



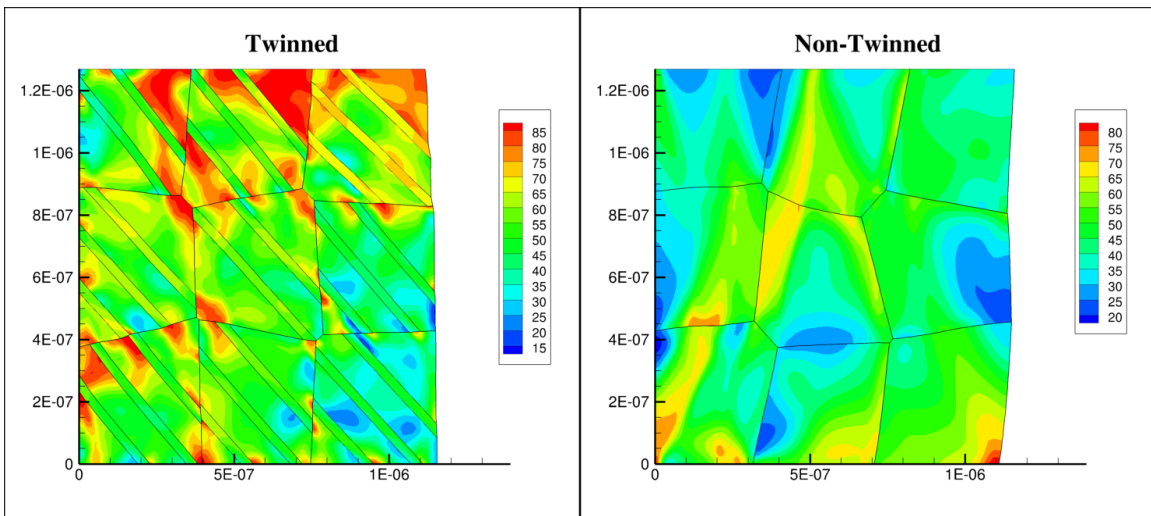
## 15° Orientation Total Immobile Dislocation Density



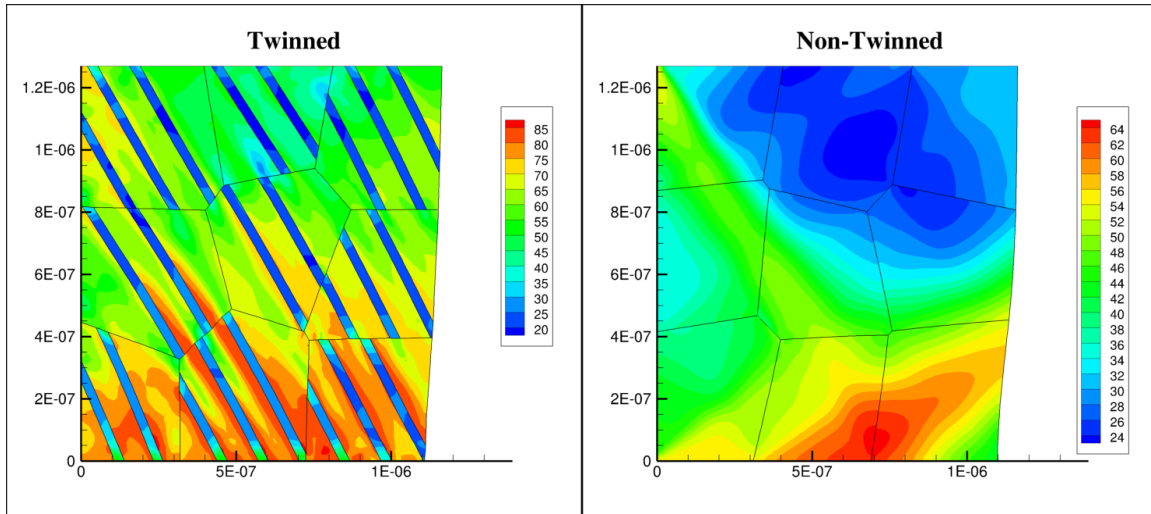
### 30° Orientation Total Immobile Dislocation Density



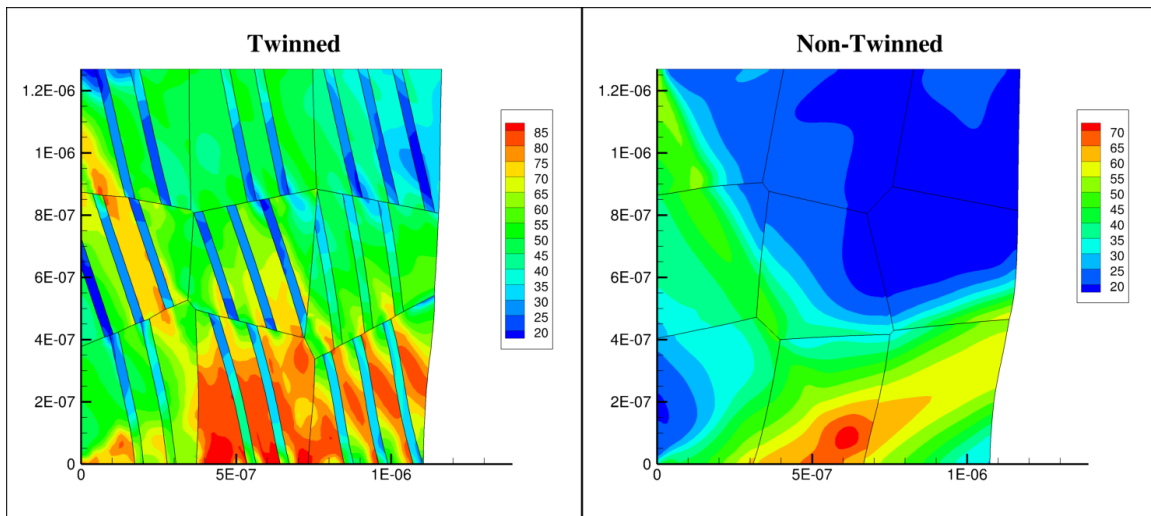
### 45° Orientation Total Immobile Dislocation Density



## 60° Orientation Total Immobile Dislocation Density



## 75° Orientation Total Immobile Dislocation Density



# 90° Orientation Total Immobile Dislocation Density

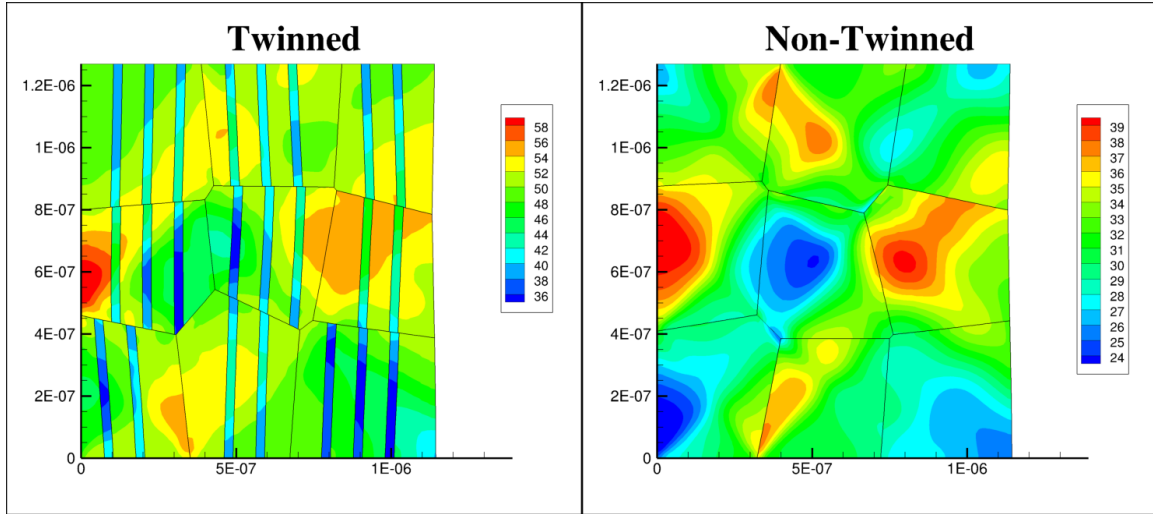
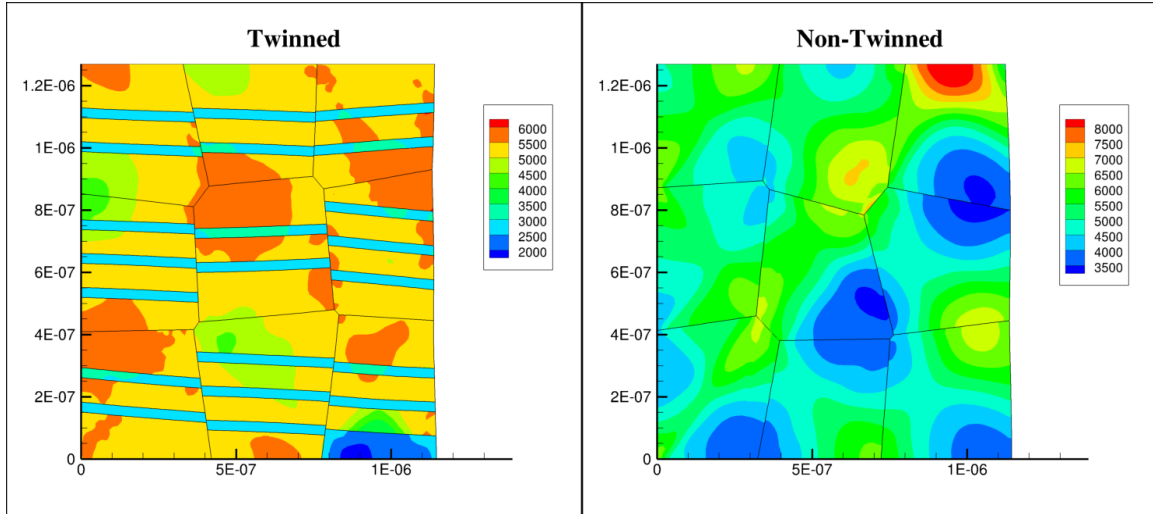
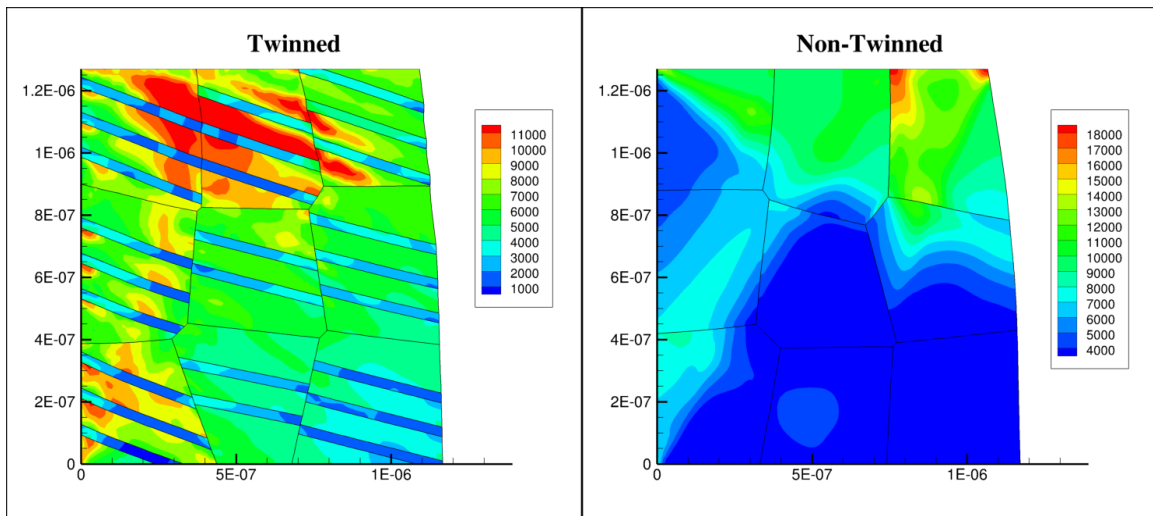


**Figure 24: Total mobile dislocation density, across all slip systems. All spatial units are in meters. Dislocation densities are normalized by their initial values.**

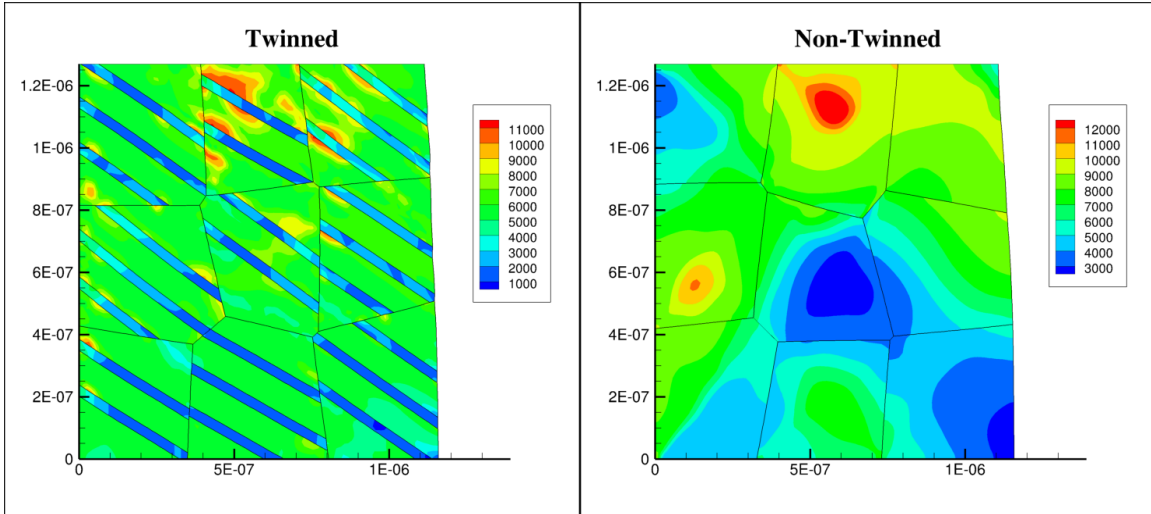
## 0° Orientation Total Mobile Dislocation Density



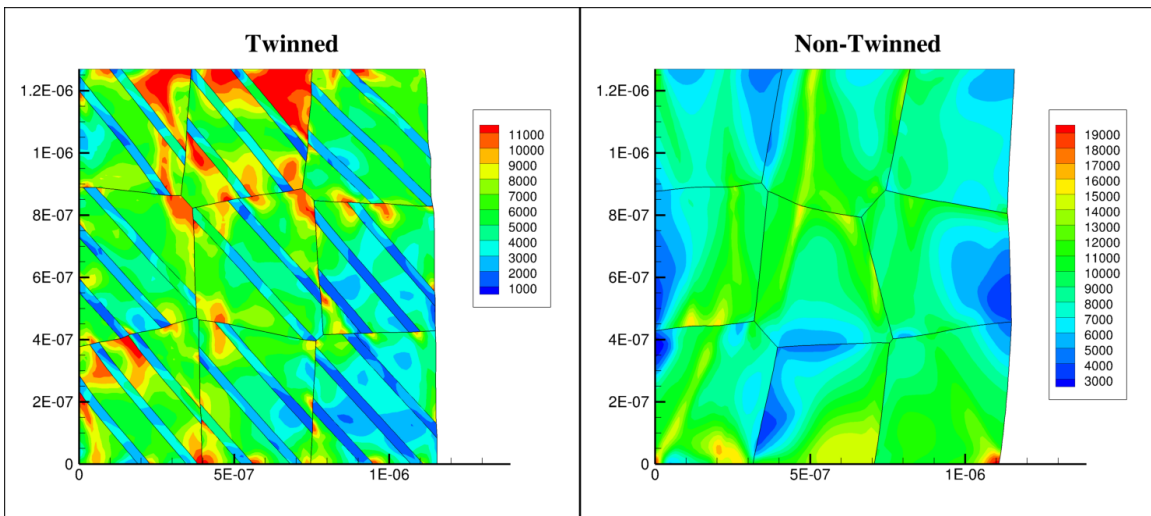
## 15° Orientation Total Mobile Dislocation Density



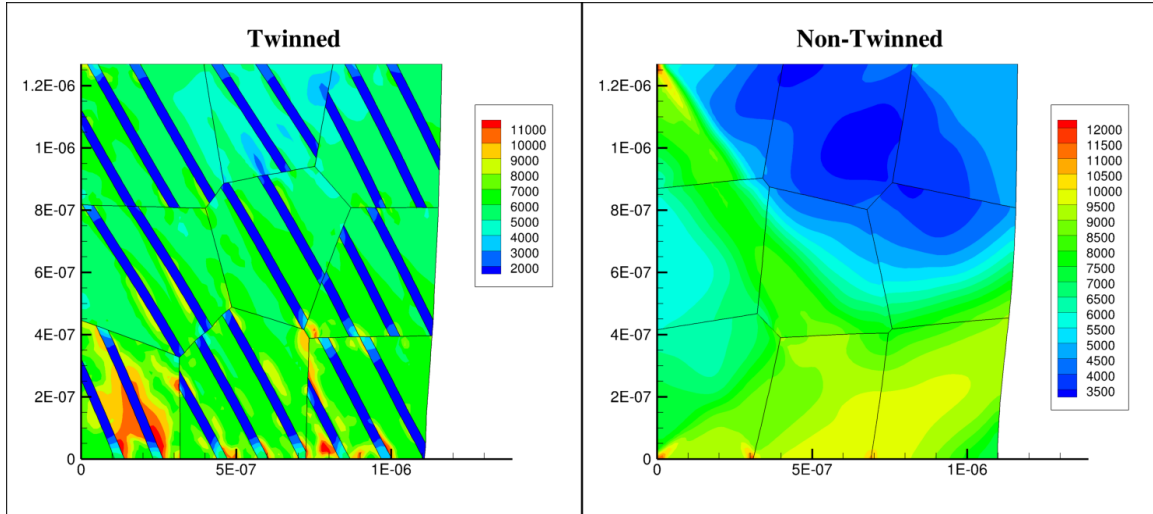
### 30° Orientation Total Mobile Dislocation Density



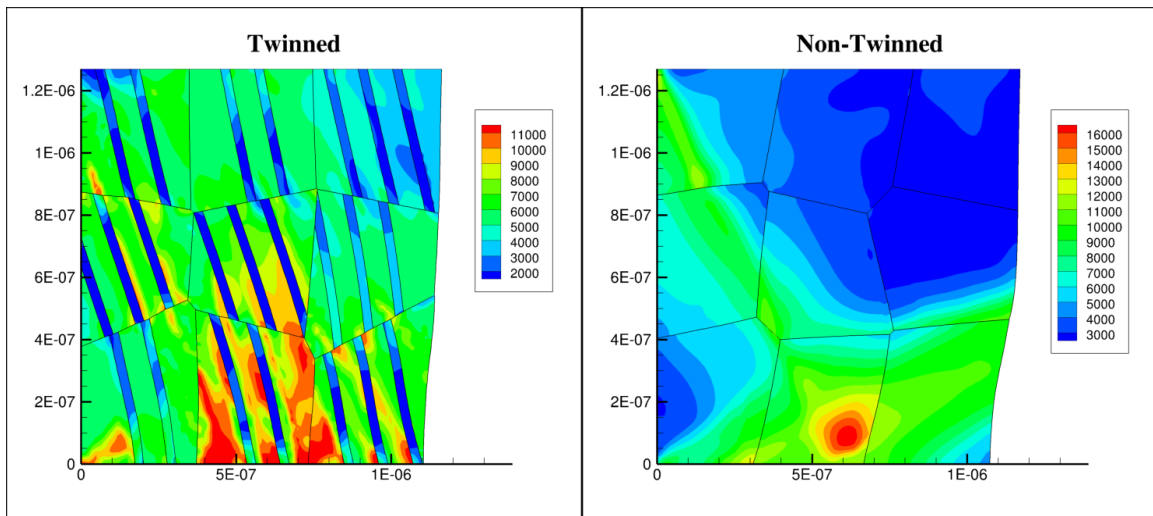
### 45° Orientation Total Mobile Dislocation Density



## 60° Orientation Total Mobile Dislocation Density



## 75° Orientation Total Mobile Dislocation Density



# 90° Orientation Total Mobile Dislocation Density

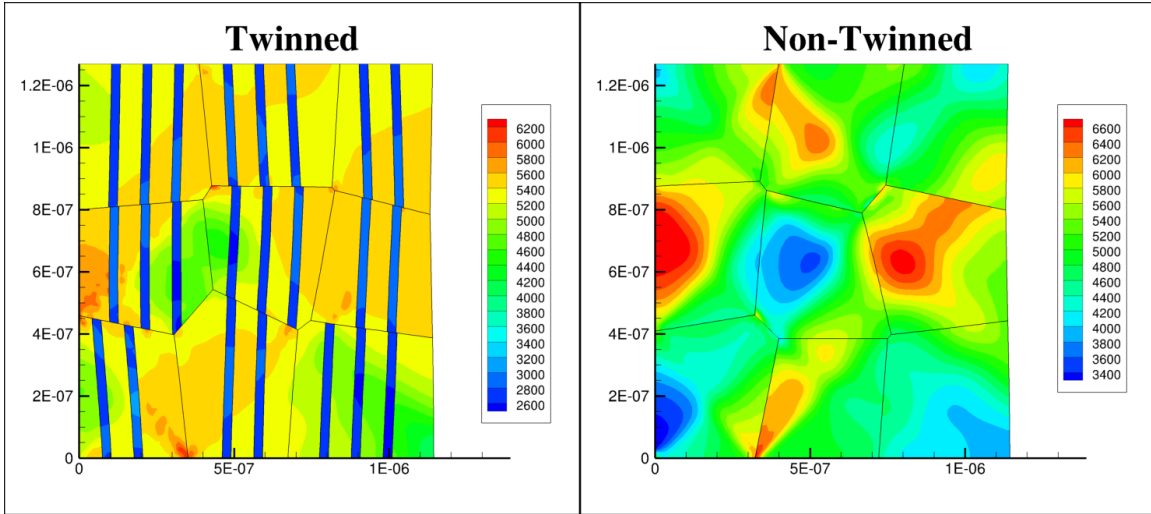
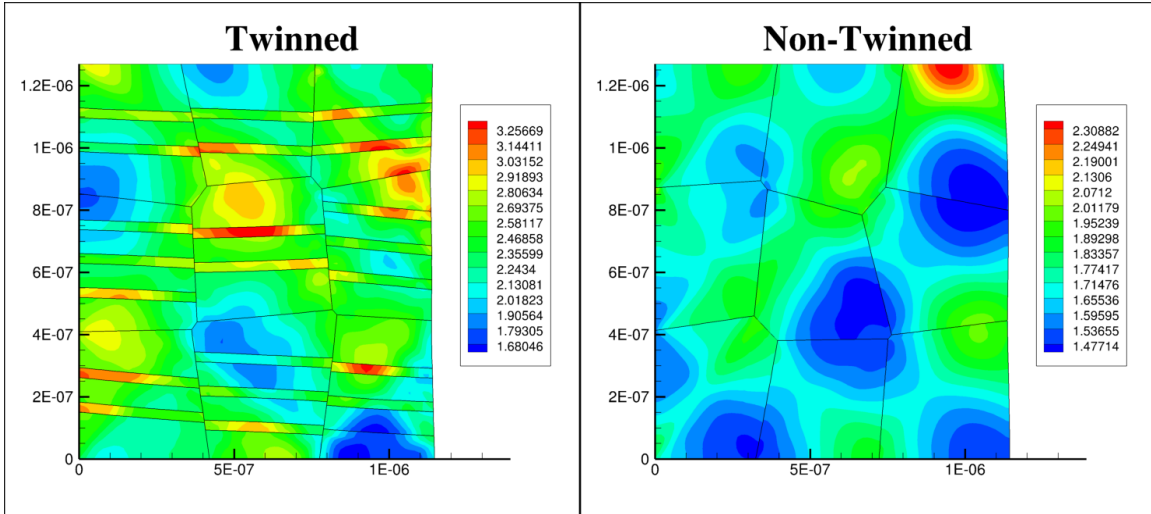
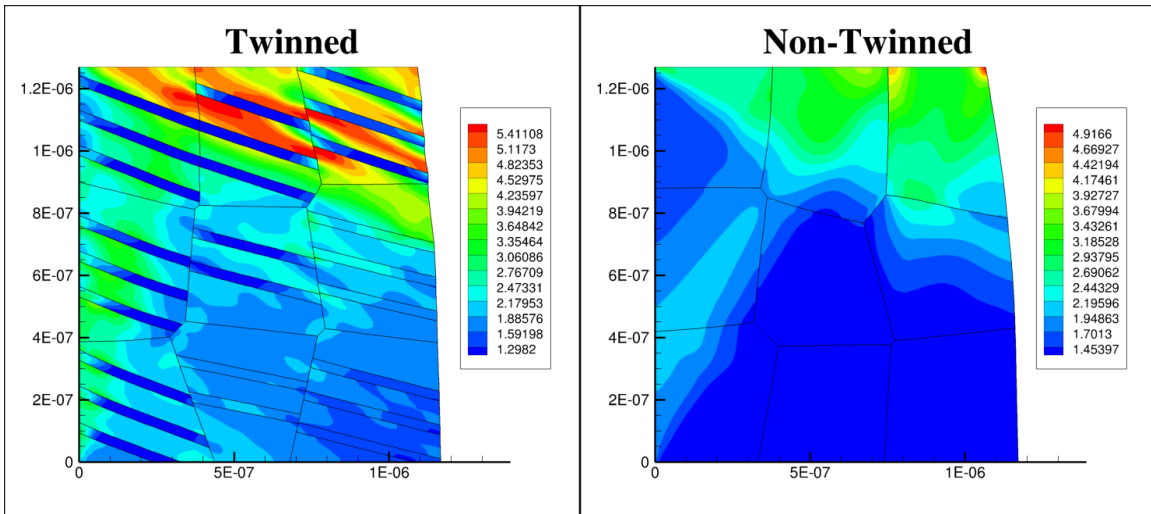


**Figure 25:**  $[\bar{1}\bar{1}\bar{1}](101)$  parent/ $[200](0\bar{2}0)$  twin slip system immobile dislocation density for  $0^\circ$ ,  $15^\circ$ ,  $30^\circ$ ,  $45^\circ$ ,  $60^\circ$ ,  $75^\circ$ , and  $90^\circ$  are shown above. All spatial units are in meters. Dislocation densities represented are normalized by their initial values.

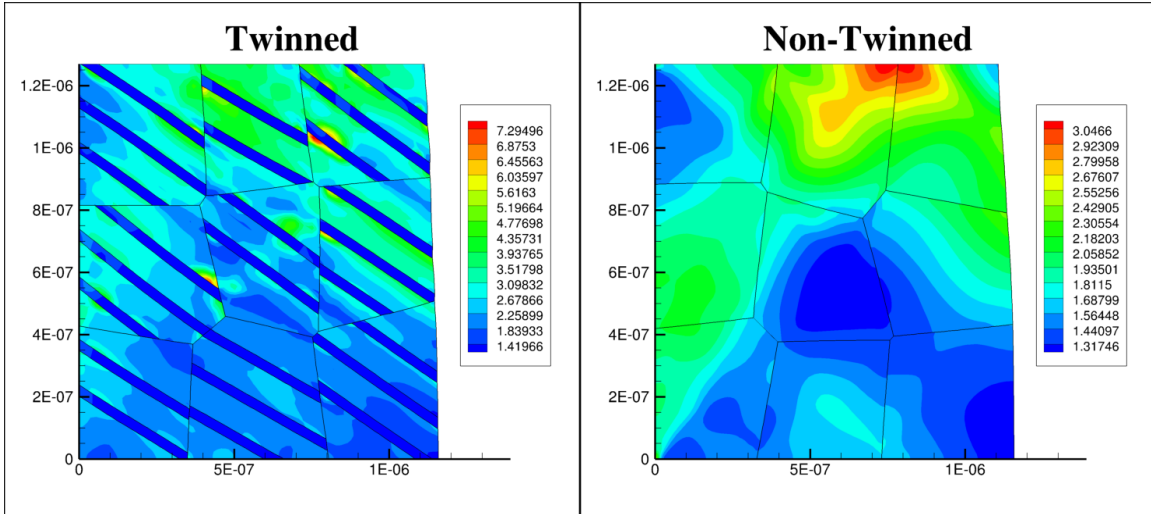
0° Oriented  $[\bar{1}\bar{1}1](101)$  parent/ $[200](0\bar{2}0)$  Twin Immobile Slip System



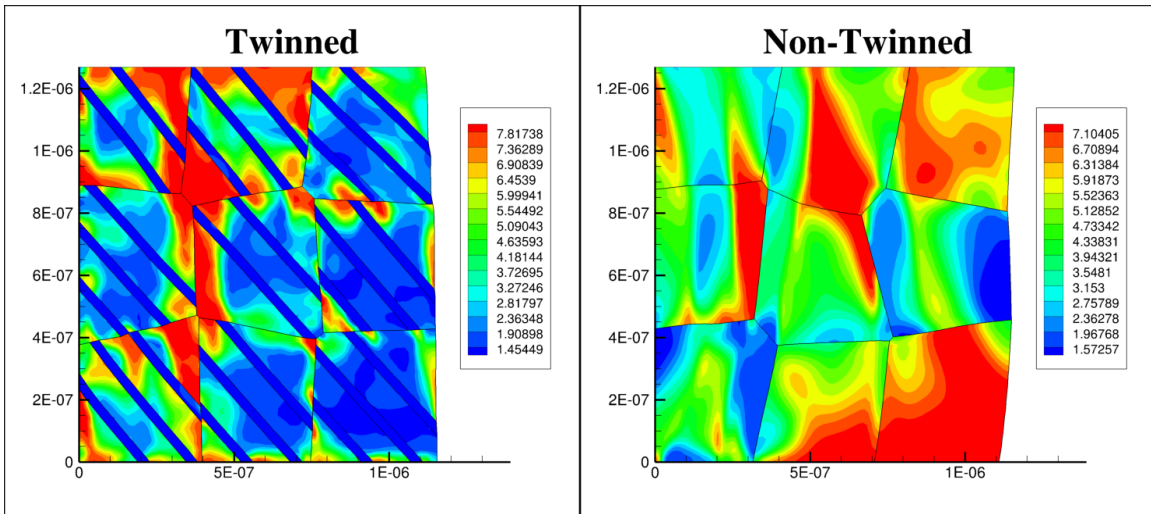
15° Oriented  $[\bar{1}\bar{1}1](101)$  parent/ $[200](0\bar{2}0)$  Twin Immobile Slip System



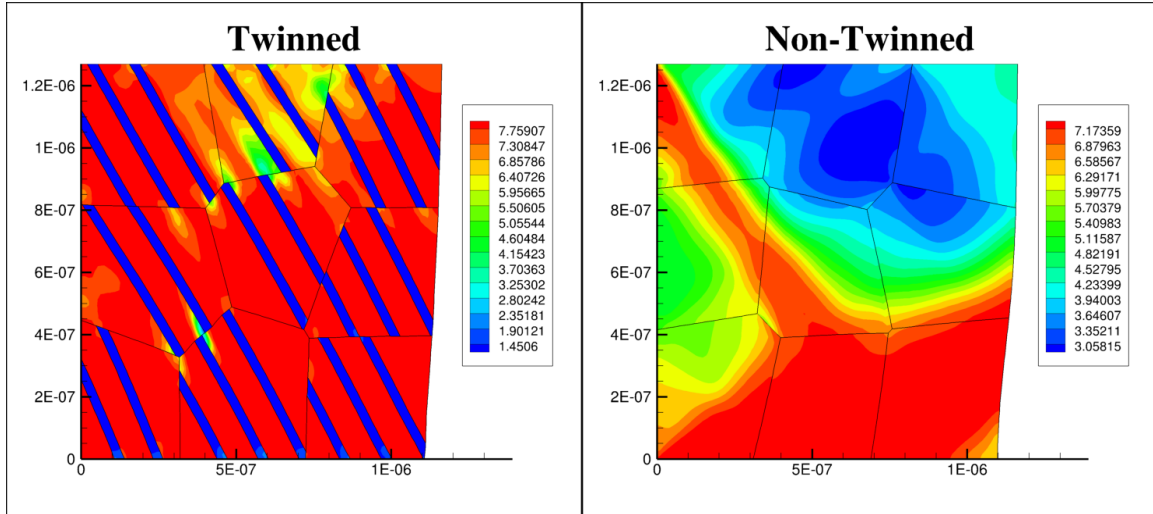
30° Oriented  $[\bar{1}\bar{1}1](101)$  parent/ $[200](0\bar{2}0)$  Twin Immobile Slip System



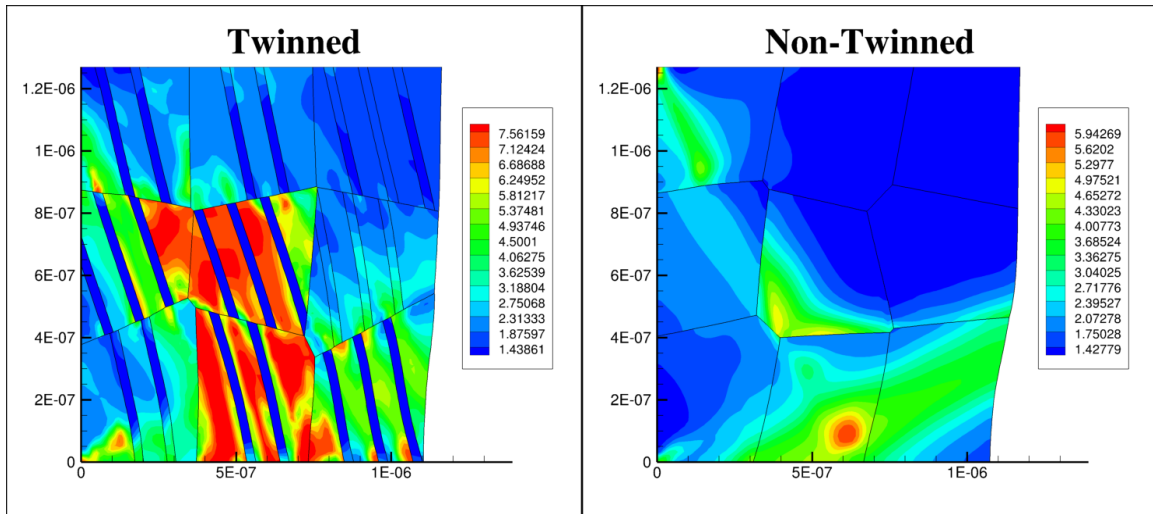
45° Oriented  $[\bar{1}\bar{1}1](101)$  parent/ $[200](0\bar{2}0)$  Twin Immobile Slip System



60° Oriented  $[\bar{1}\bar{1}\bar{1}](101)$  parent/ $[200](0\bar{2}0)$  Twin Immobile Slip System



75° Oriented  $[\bar{1}\bar{1}\bar{1}](101)$  parent/ $[200](0\bar{2}0)$  Twin Immobile Slip System



90° Oriented  $[\bar{1}\bar{1}\bar{1}](101)$  parent/ $[200](0\bar{2}0)$  Twin Immobile Slip System

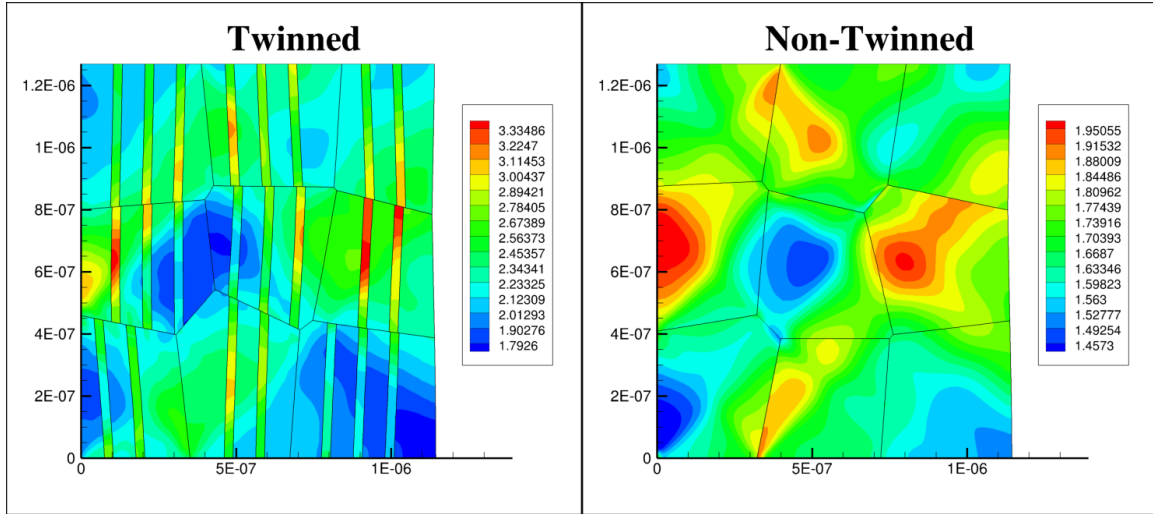
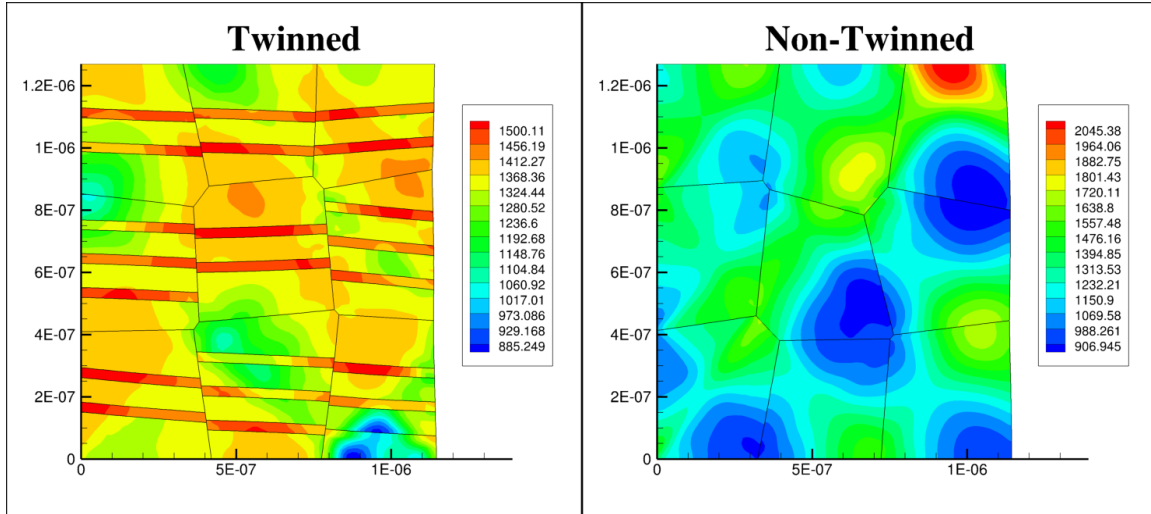
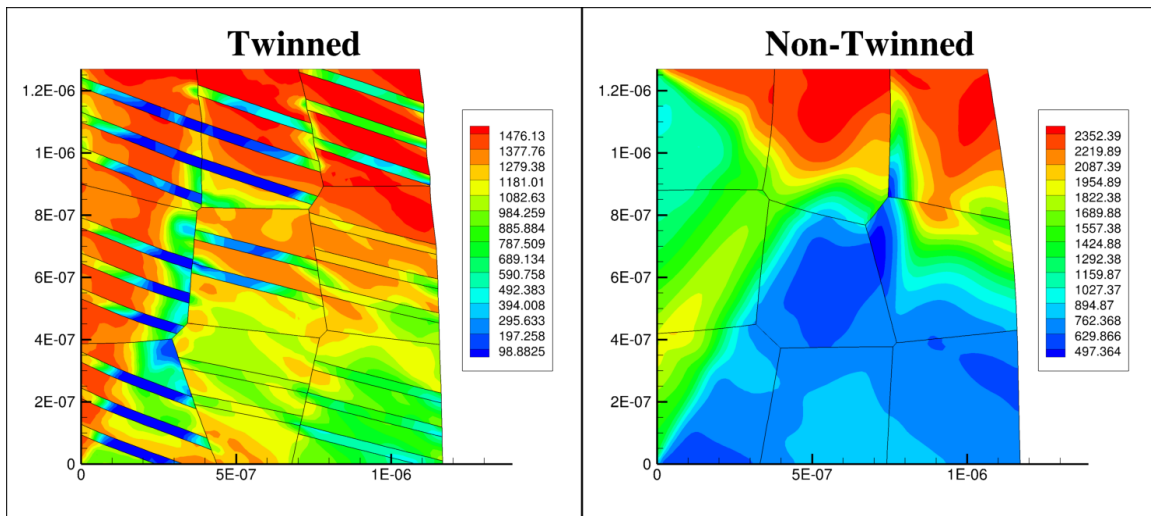


**Figure 26:  $[\bar{1}\bar{1}1](011)$  parent/ $[\bar{1}\bar{1}1](0\bar{1}\bar{1})$  twin slip system mobile dislocation density for  $0^\circ, 15^\circ, 30^\circ, 45^\circ, 60^\circ, 75^\circ,$  and  $90^\circ$  are shown above. All spatial units are in meters. Dislocation densities represented are normalized by their initial values.**

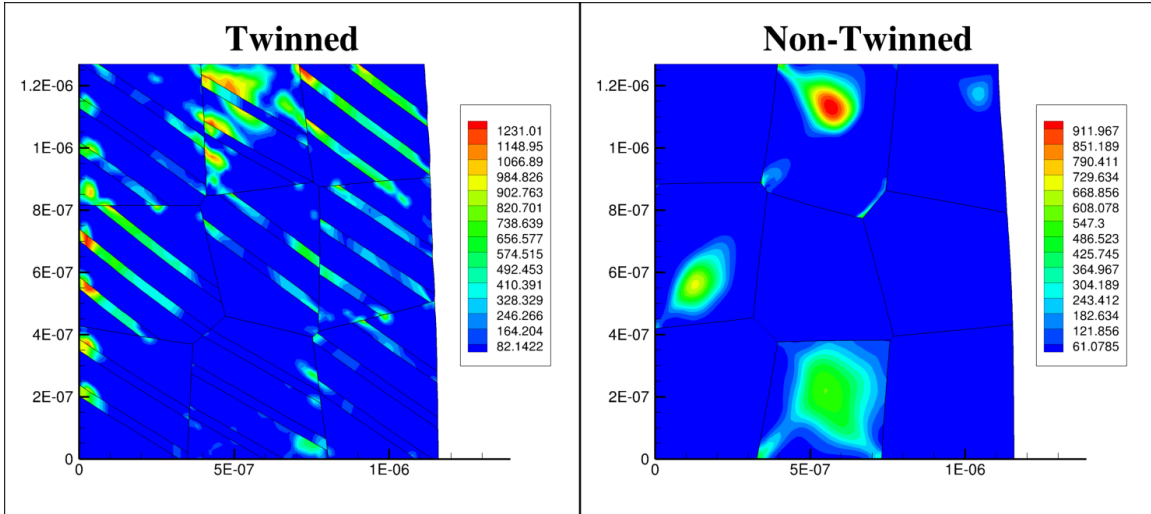
0° Oriented  $[\bar{1}\bar{1}1](011)$  parent/ $[\bar{1}\bar{1}1](0\bar{1}\bar{1})$  twinned mobile slip system



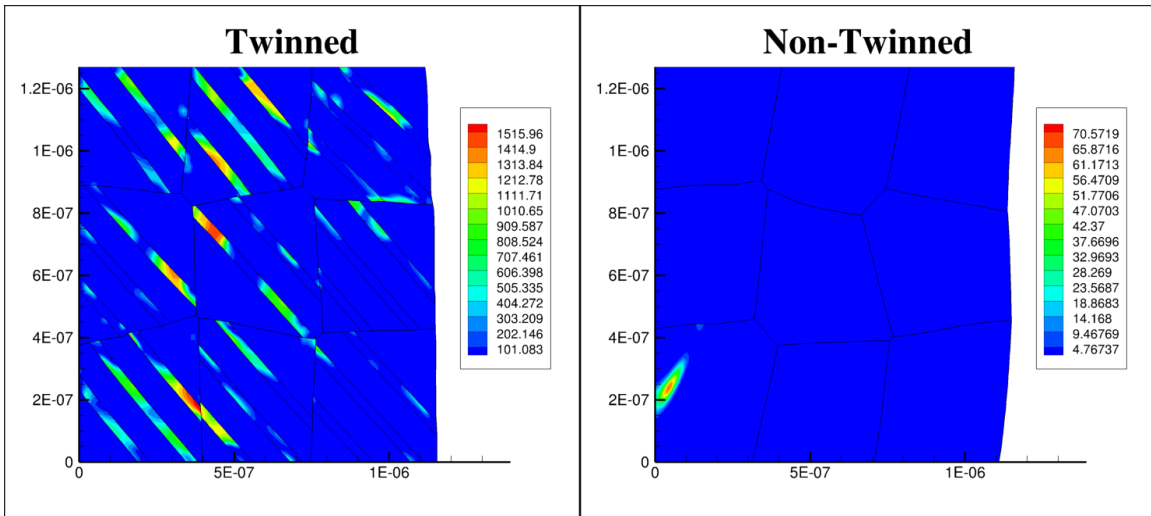
15° Oriented  $[\bar{1}\bar{1}1](011)$  parent/ $[\bar{1}\bar{1}1](0\bar{1}\bar{1})$  twinned mobile slip system



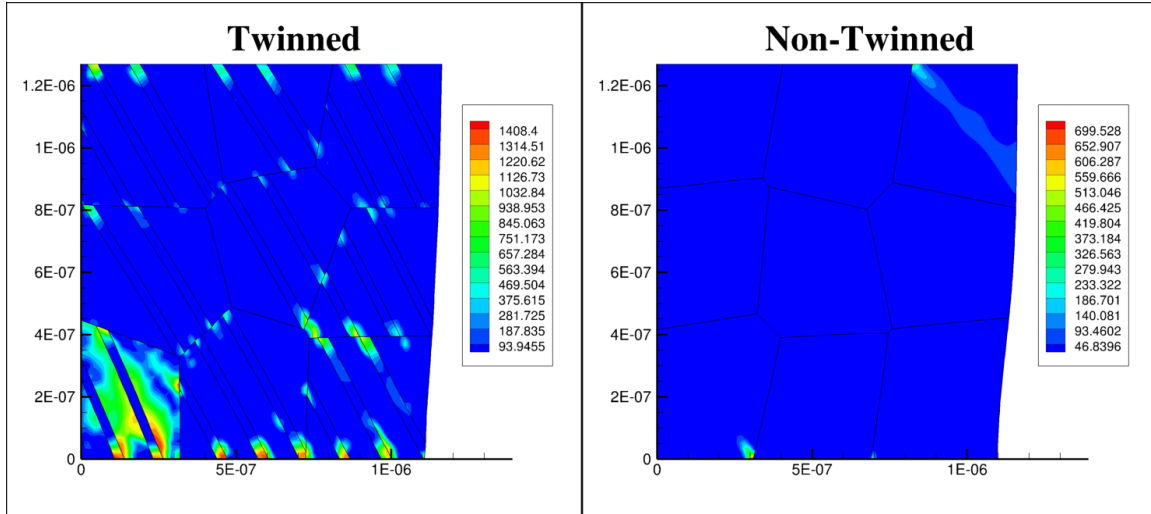
30° Oriented  $[\bar{1}\bar{1}1](011)$  parent/ $[\bar{1}\bar{1}1](0\bar{1}\bar{1})$  twinned mobile slip system



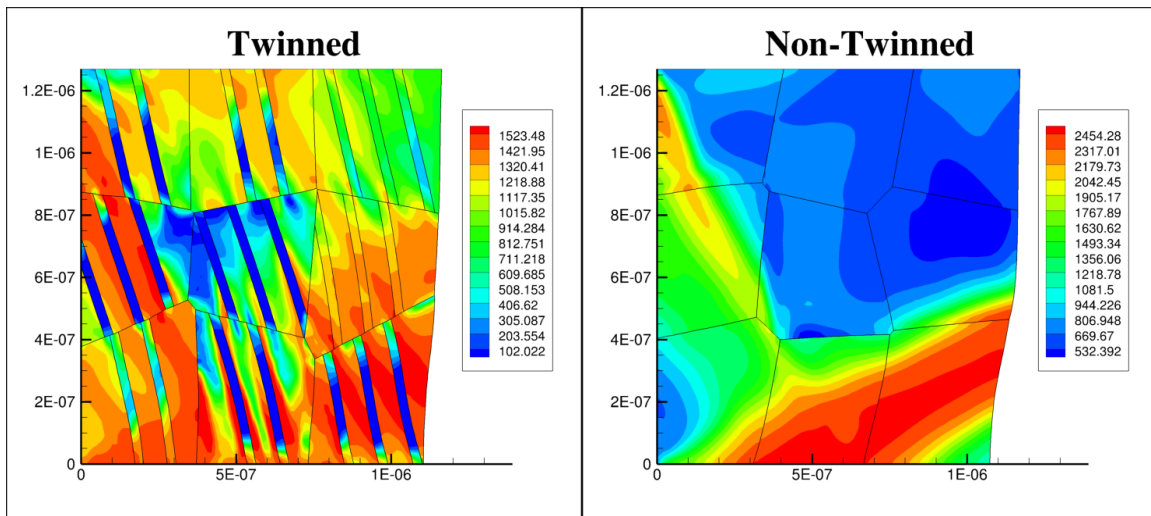
45° Oriented  $[\bar{1}\bar{1}1](011)$  parent/ $[\bar{1}\bar{1}1](0\bar{1}\bar{1})$  twinned mobile slip system



60° Oriented  $[\bar{1}\bar{1}1](011)$  parent/ $[\bar{1}\bar{1}1](0\bar{1}\bar{1})$  twinned mobile slip system



75° Oriented  $[\bar{1}\bar{1}1](011)$  parent/ $[\bar{1}\bar{1}1](0\bar{1}\bar{1})$  twinned mobile slip system



90° Oriented  $[1\bar{1}1](011)$  parent/ $[1\bar{1}1](0\bar{1}\bar{1})$  twinned mobile slip system

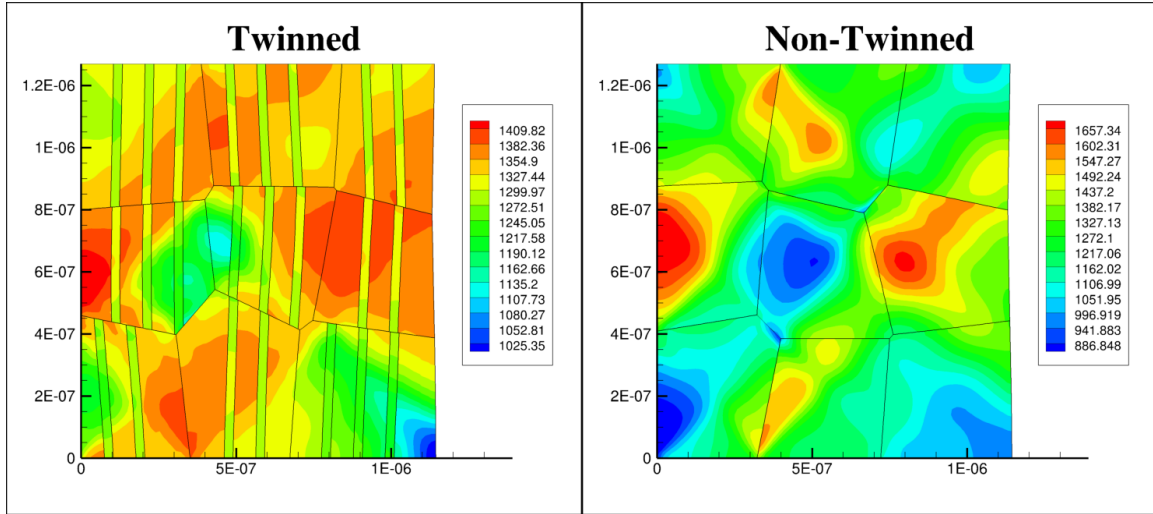
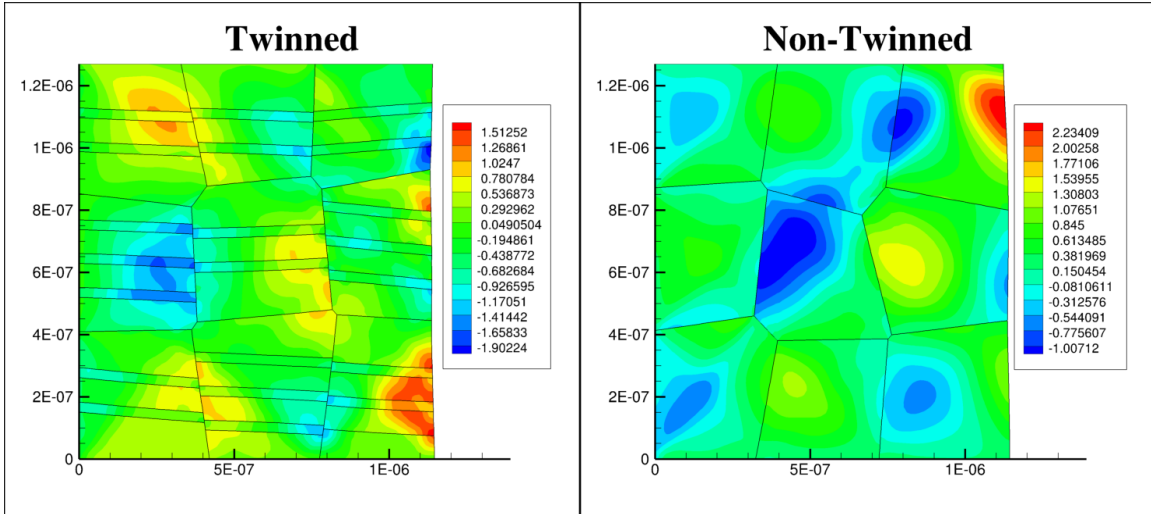
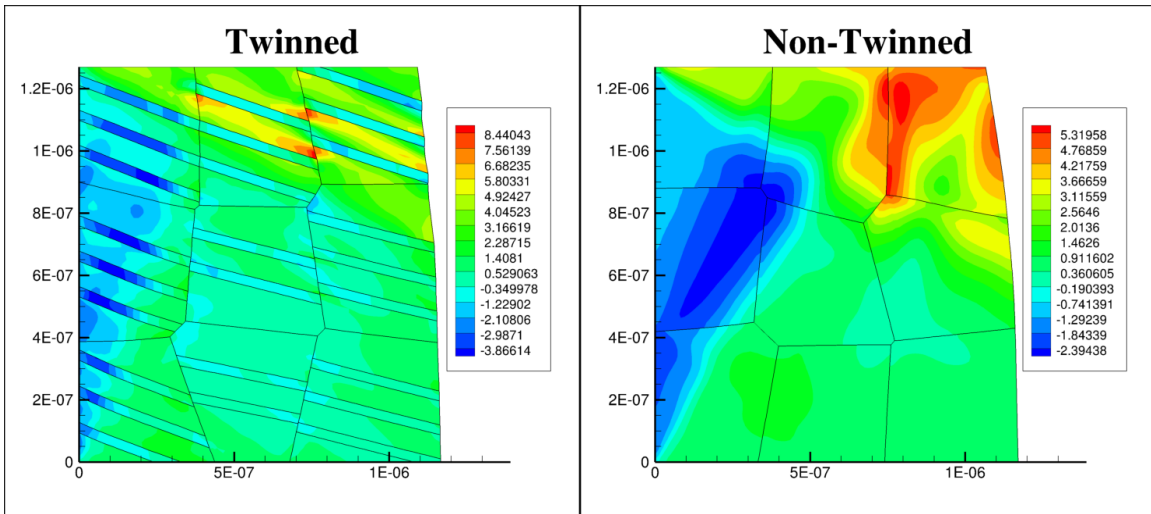


**Figure 27: Lattice rotation for twinned and non-twinned materials at various orientations. (All spatial units are in meters)**

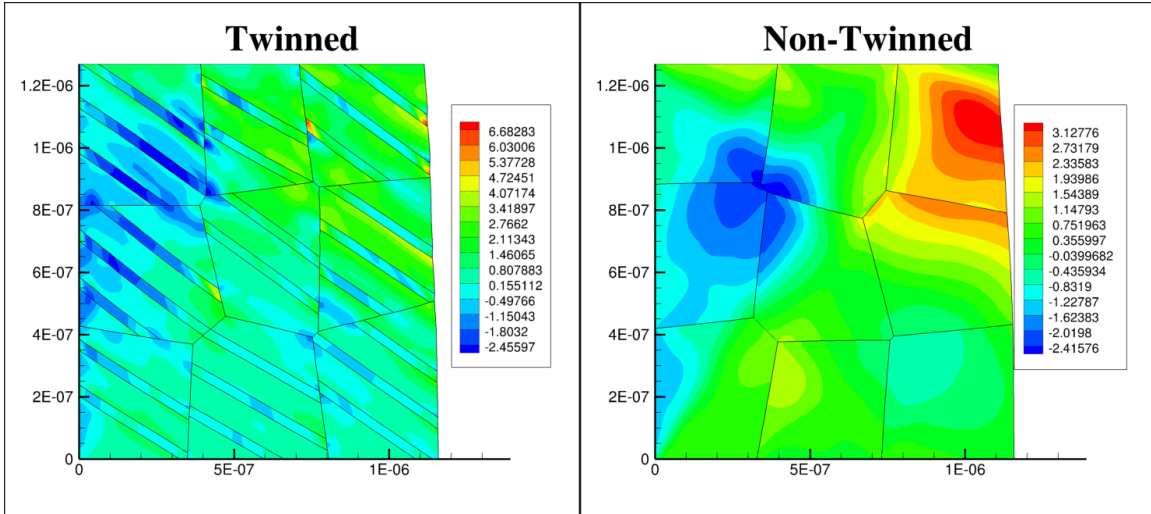
## 0° Orientation Lattice Rotation



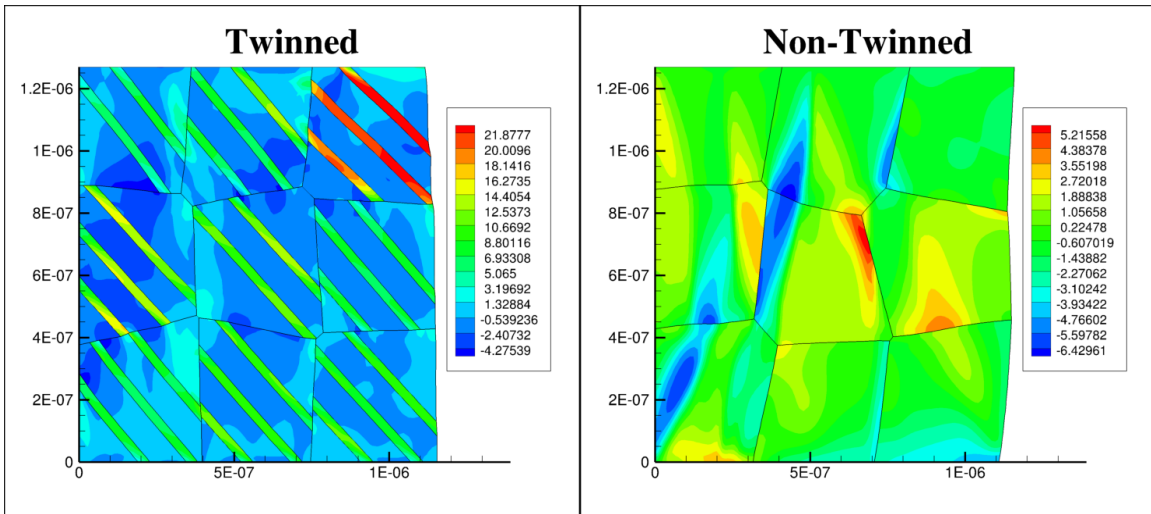
## 15° Orientation Lattice Rotation



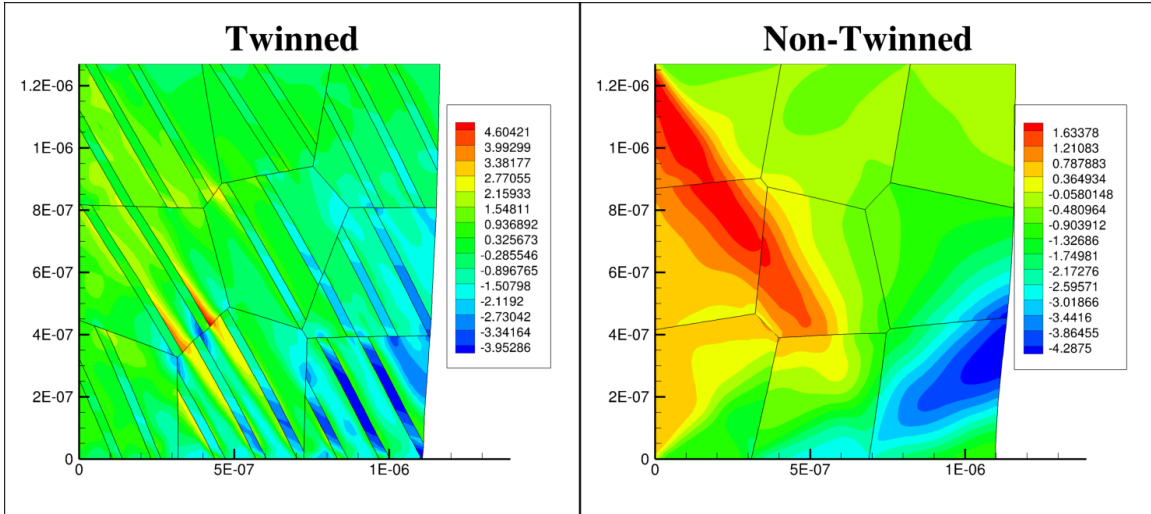
### 30° Orientation Lattice Rotation



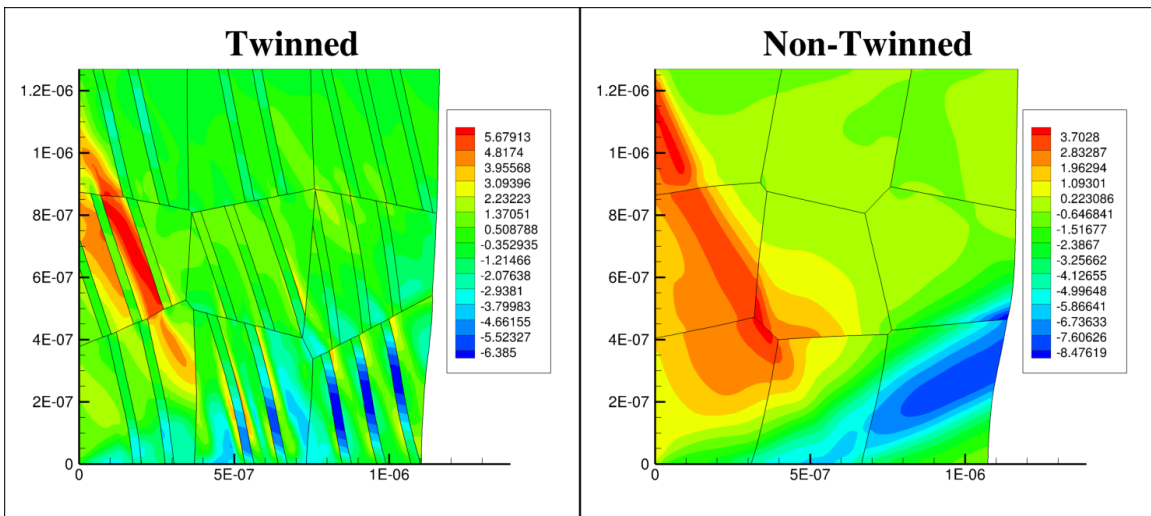
### 45° Orientation Lattice Rotation



## 60° Orientation Lattice Rotation



## 75° Orientation Lattice Rotation



# 90° Orientation Lattice Rotation

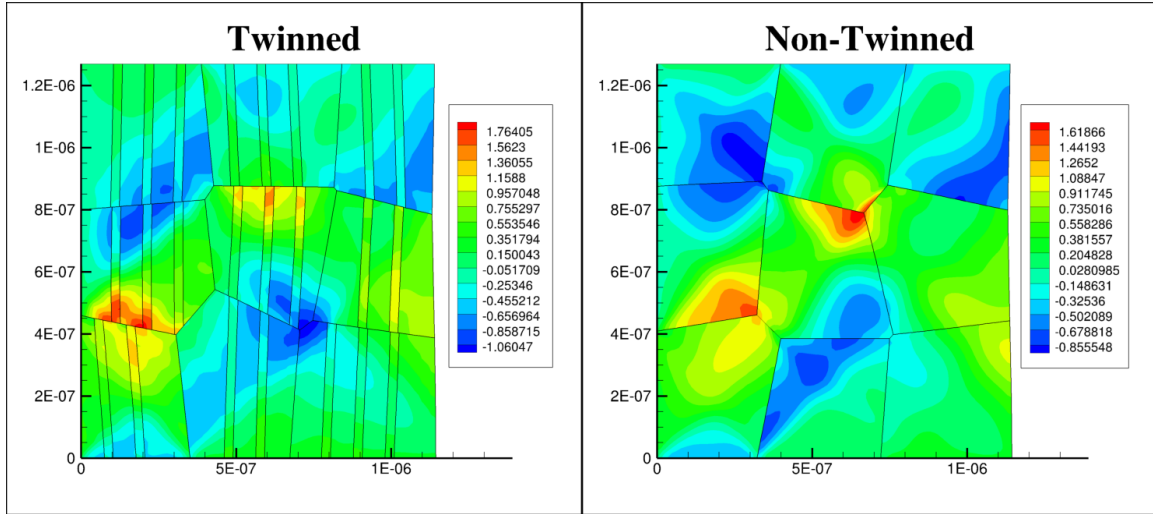
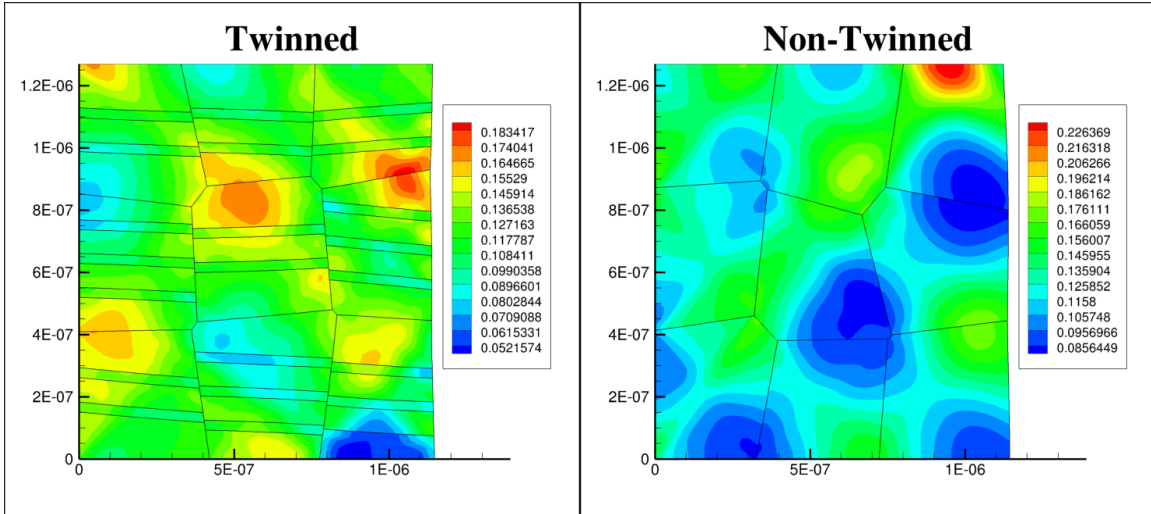
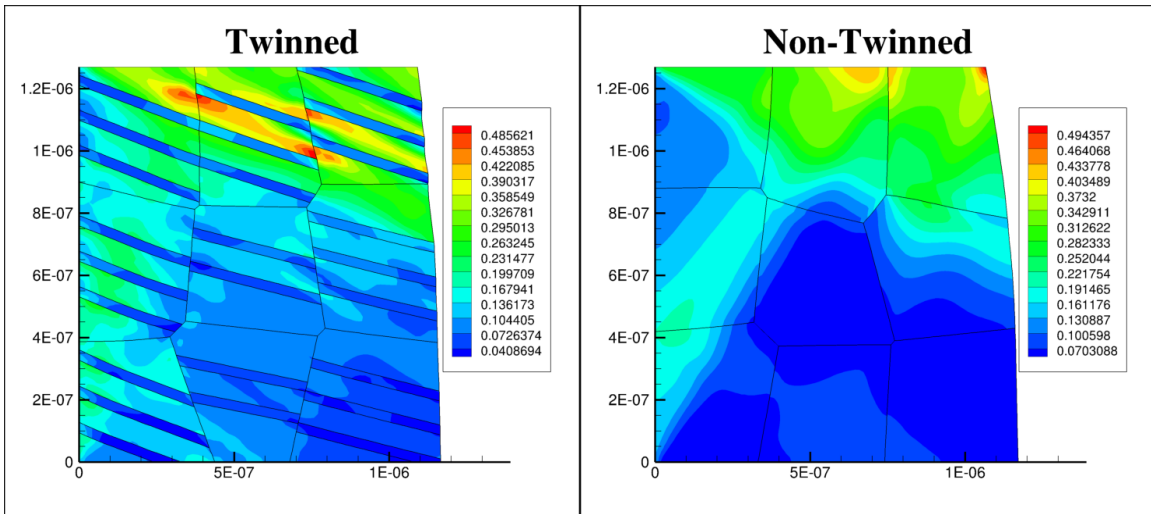


**Figure 28: Shear slip comparisons between twinned and non-twinned materials. (All spatial units are in meters)**

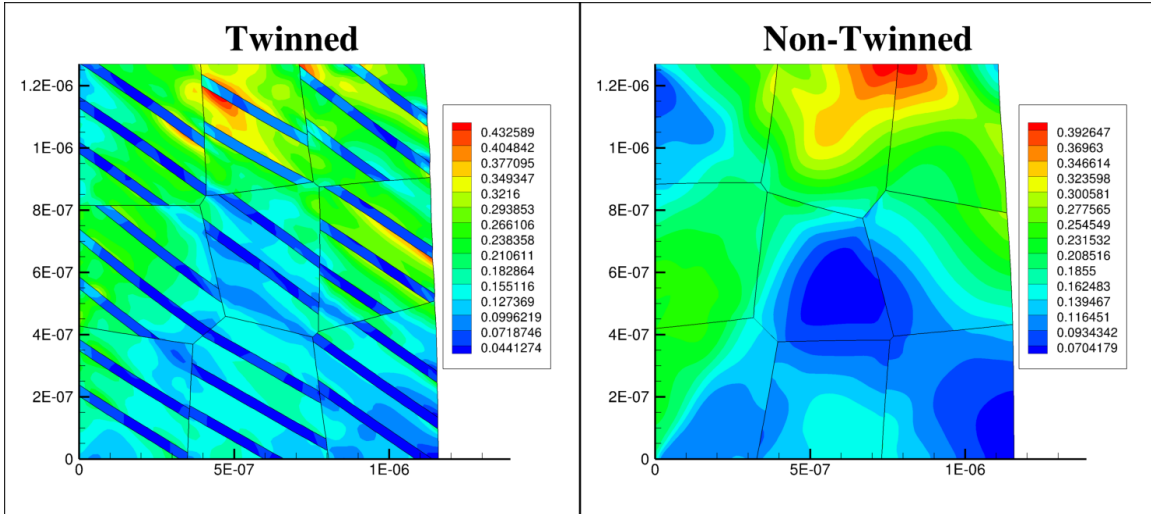
## 0° Orientation Shear Slip



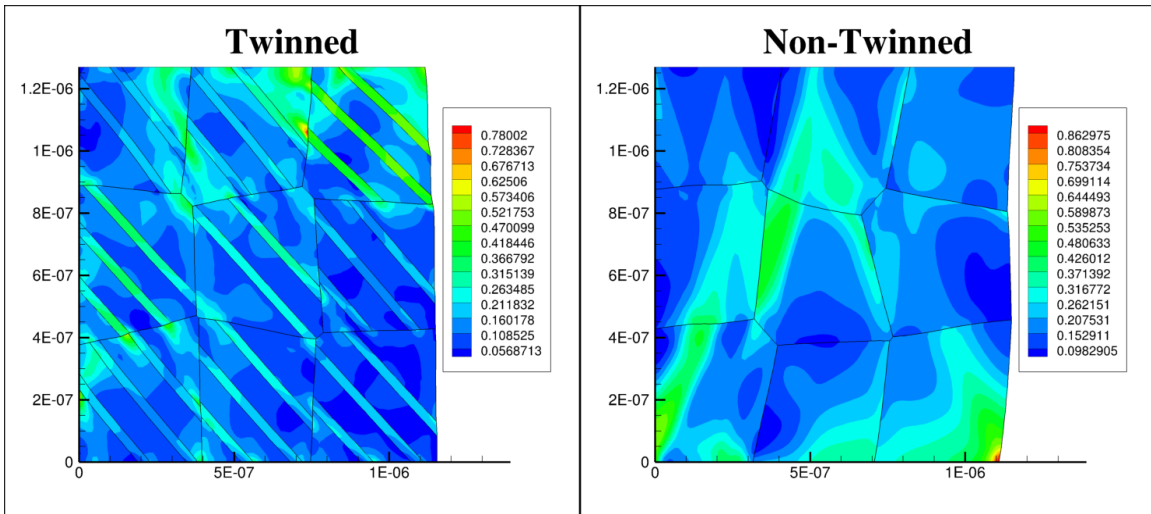
## 15° Orientation Shear Slip



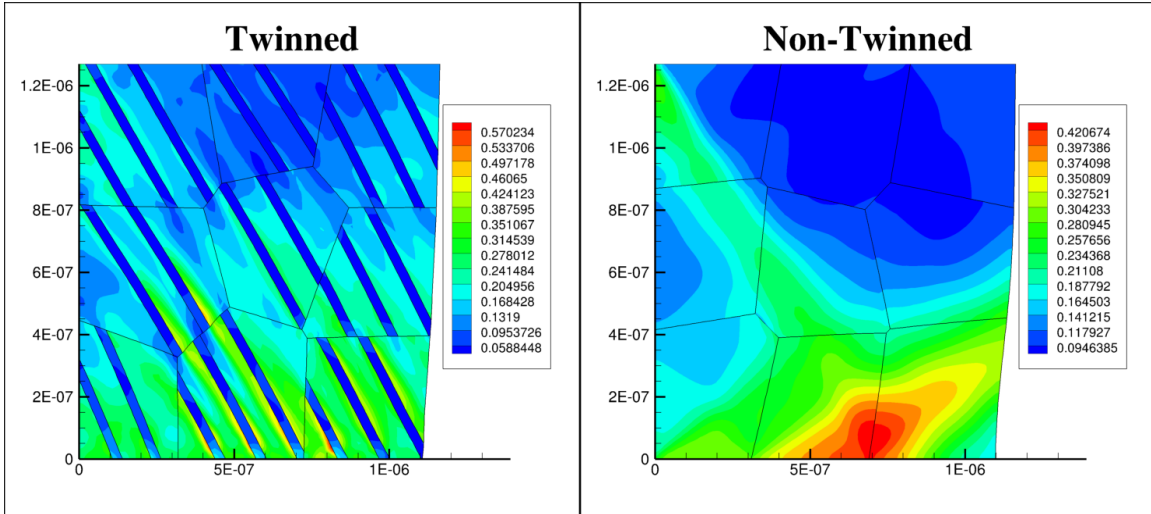
### 30° Orientation Shear Slip



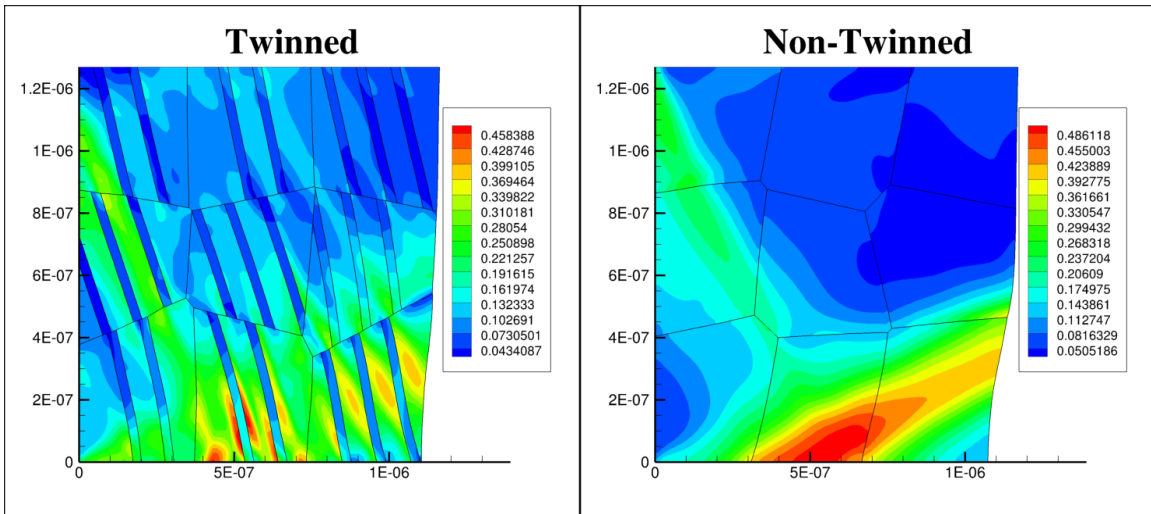
### 45° Orientation Shear Slip



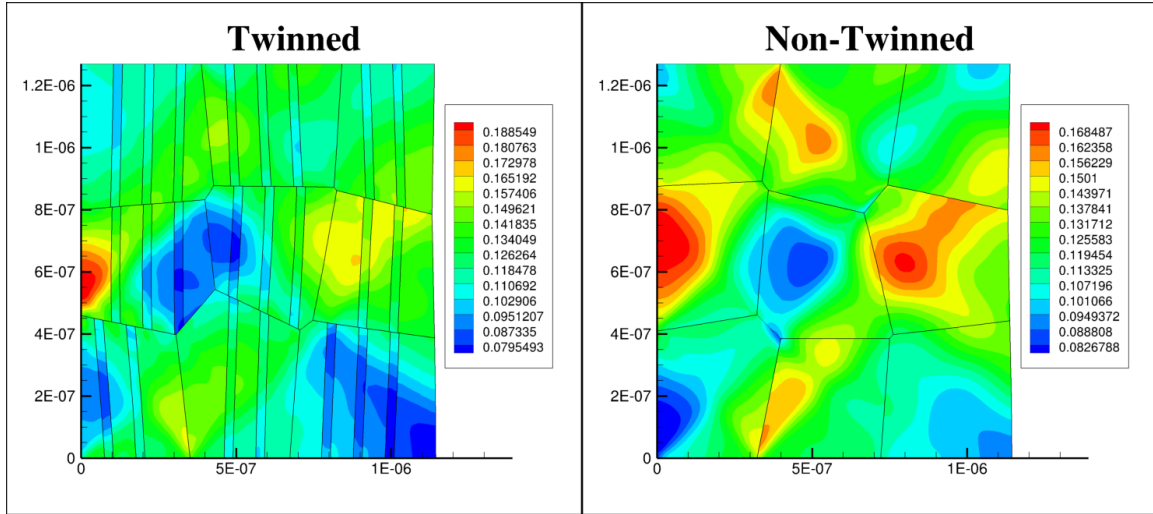
### 60° Orientation Shear Slip



### 75° Orientation Shear Slip



# 90° Orientation Shear Slip



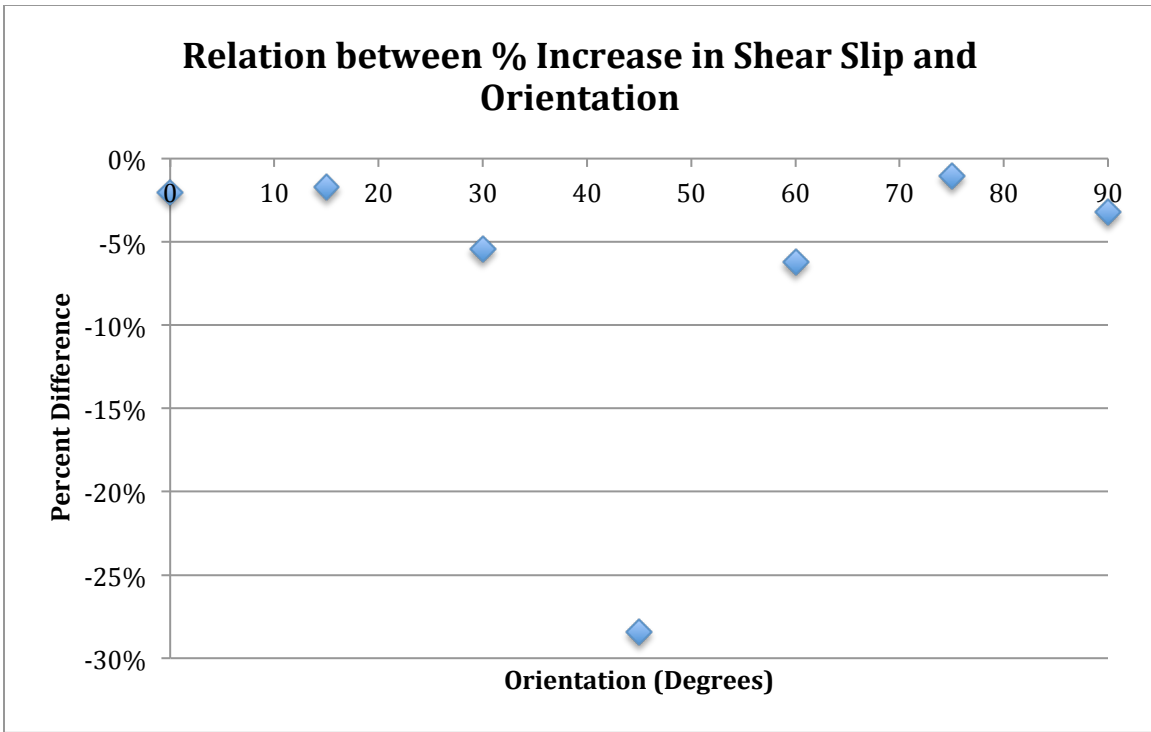
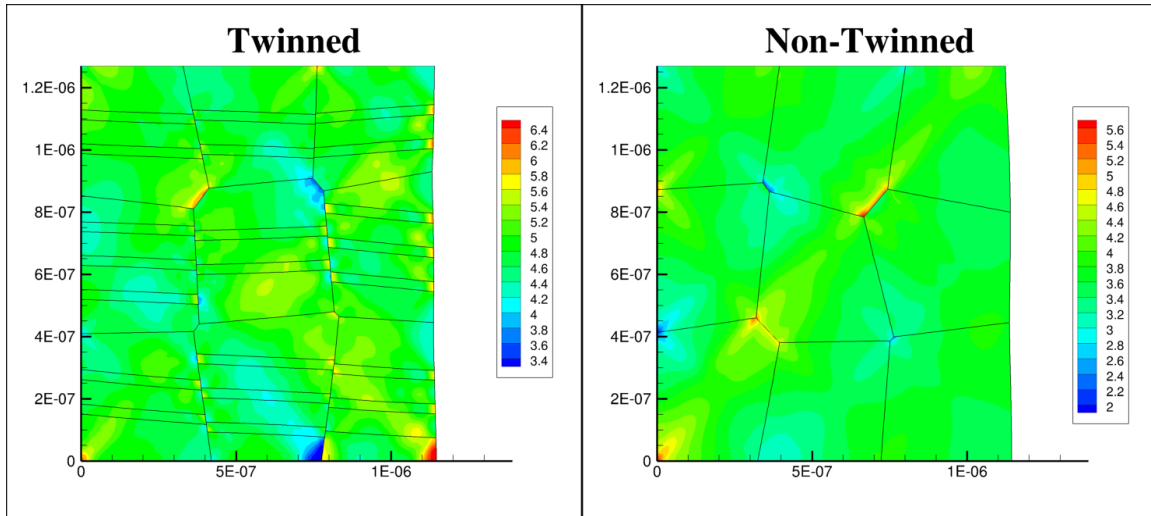


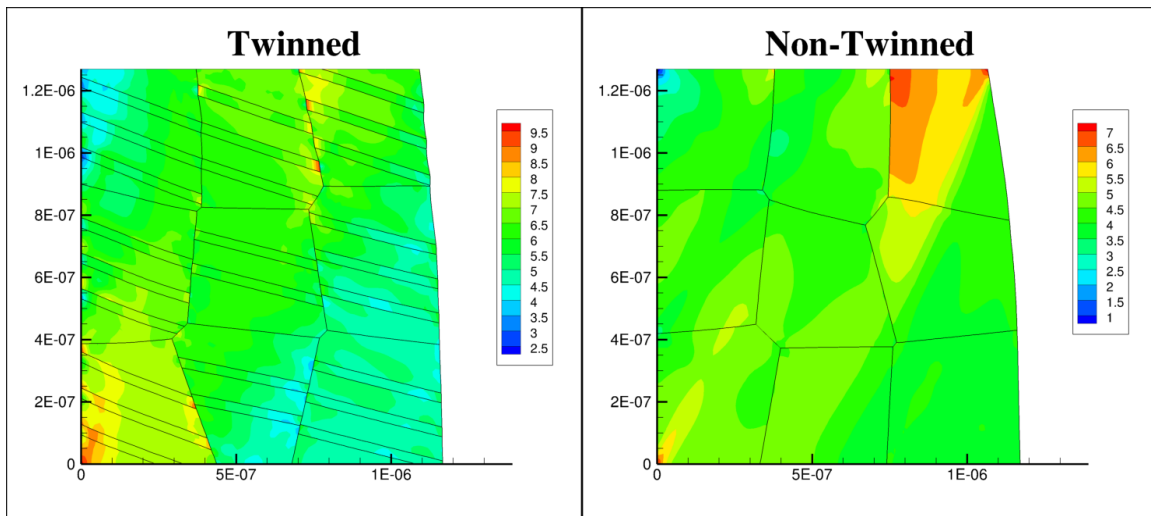
**Figure 29: Percent difference in aggregate shear slip compared with material orientation.**

**Figure 30: Normalized stress comparisons between twinned and non-twinned materials.**  
(All spatial units are in meters)

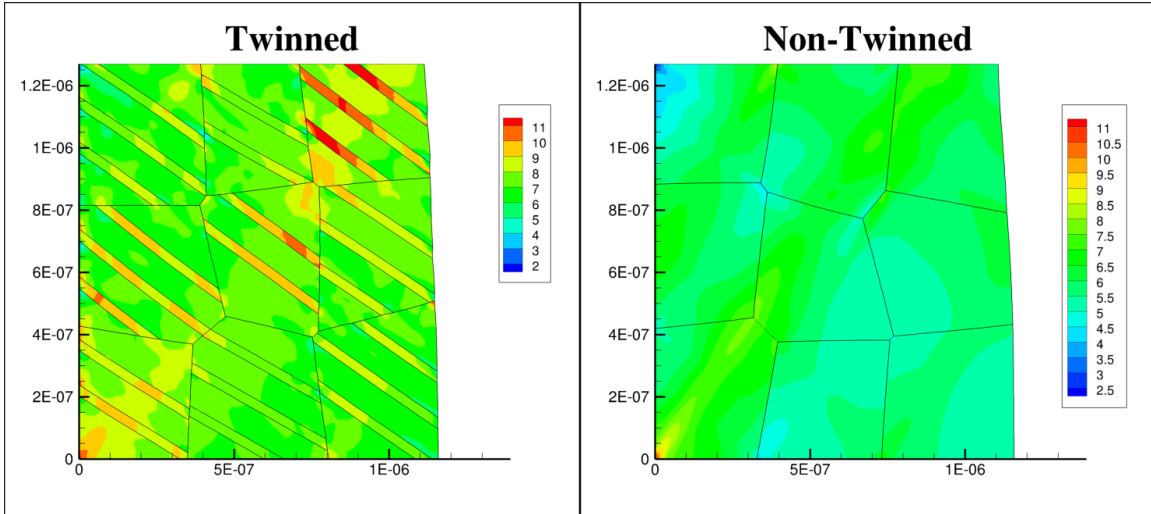
### Normal Stress for 0° Orientation (Normalized by Yield Stress)



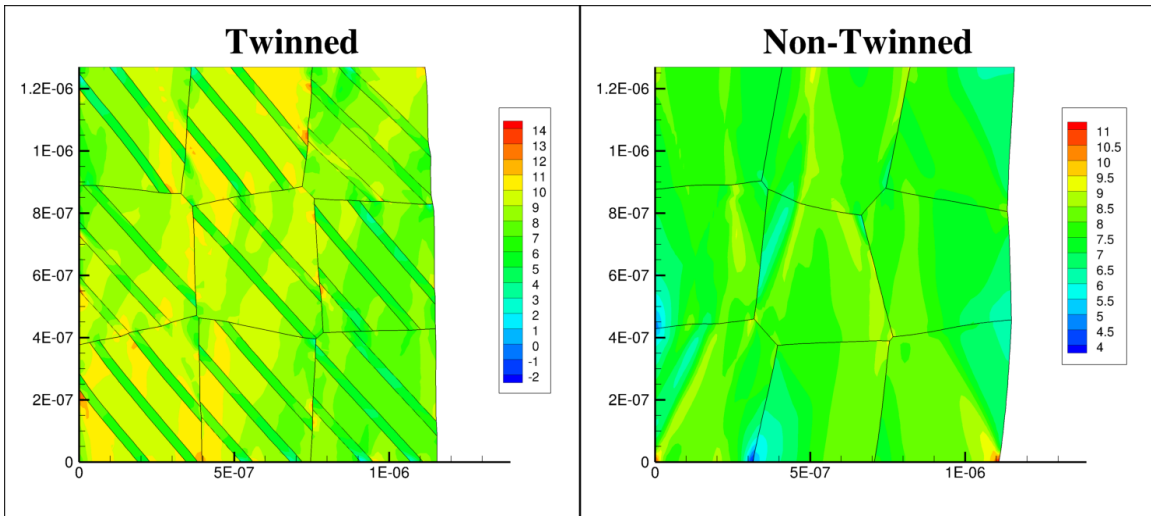
### 15° Orientation Normal Stress



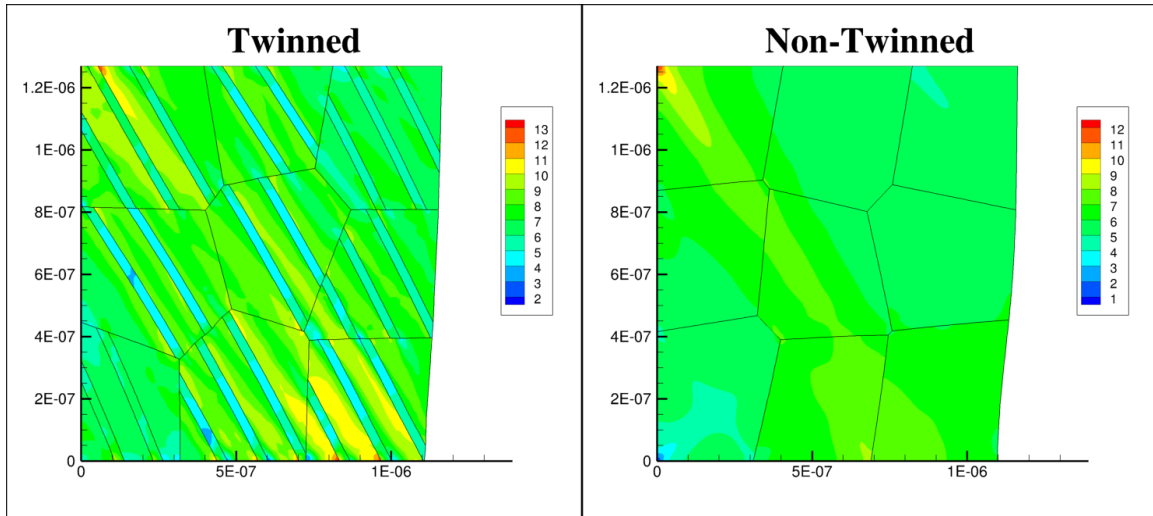
### 30° Orientation Normal Stress



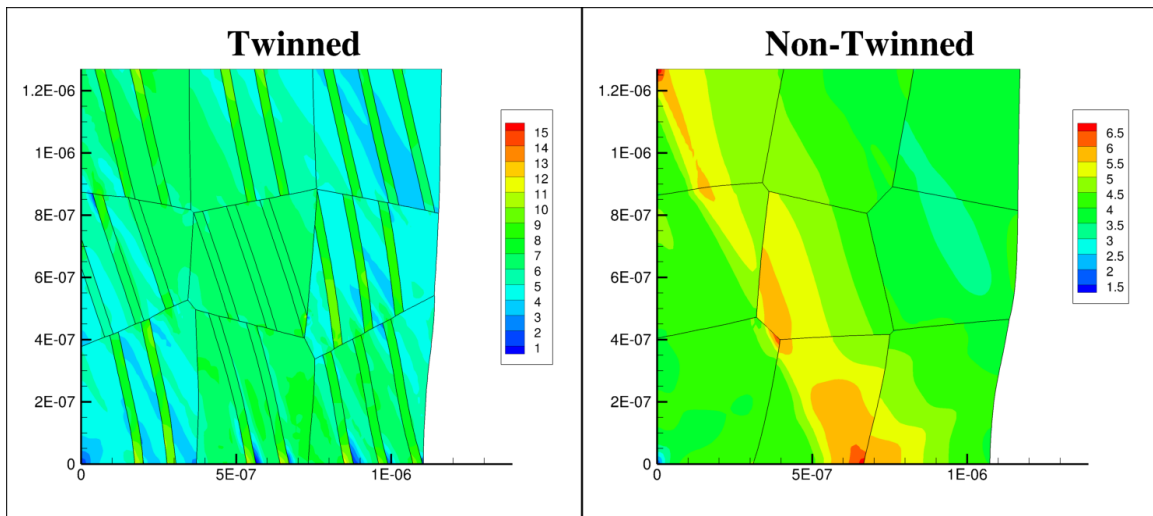
### 45° Orientation Normal Stress



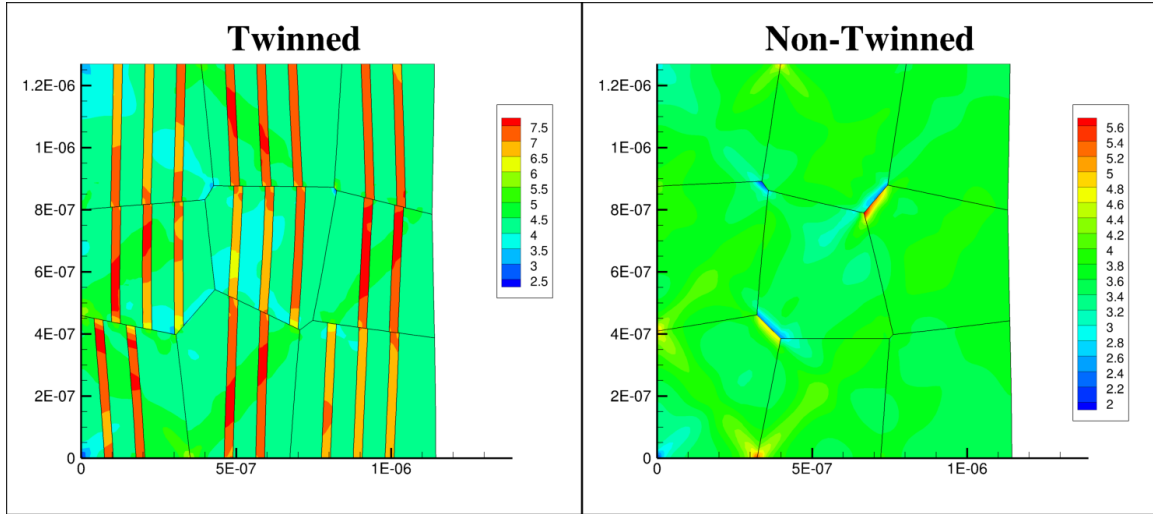
### 60° Orientation Normal Stress



### 75° Orientation Normal Stress



# 90° Orientation Normal Stress



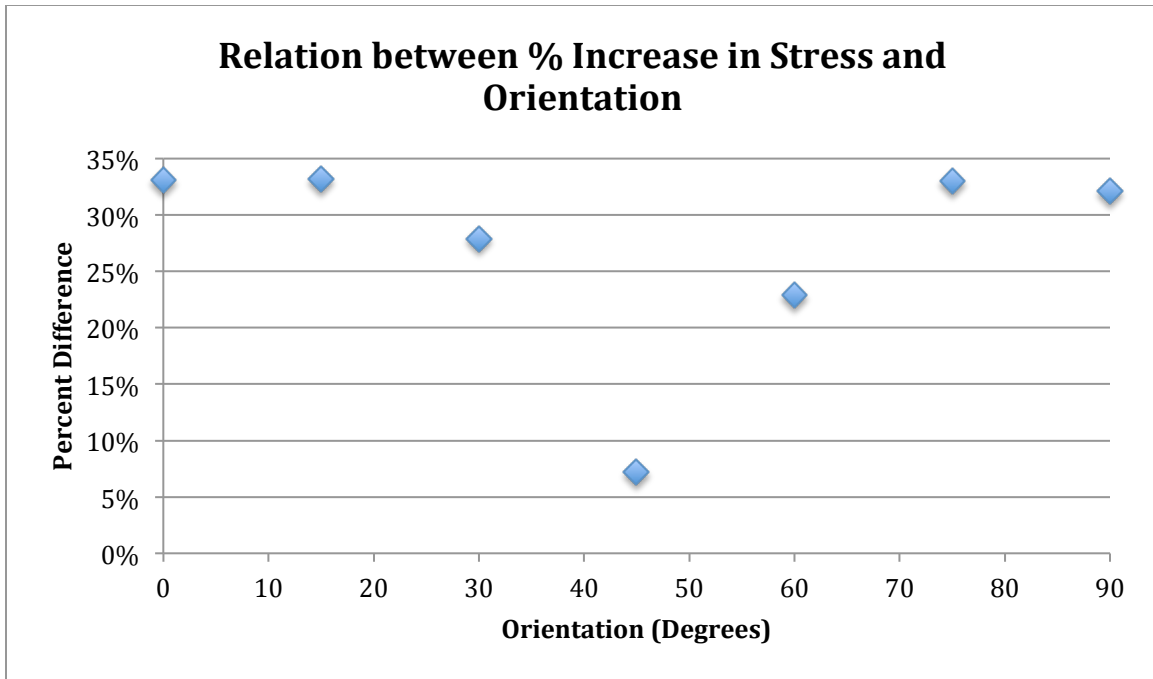
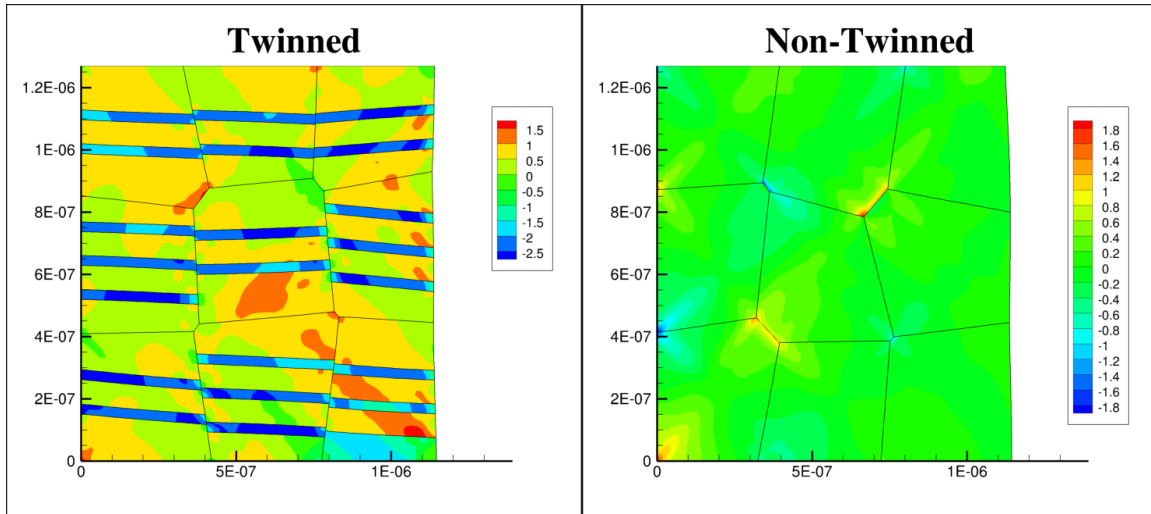


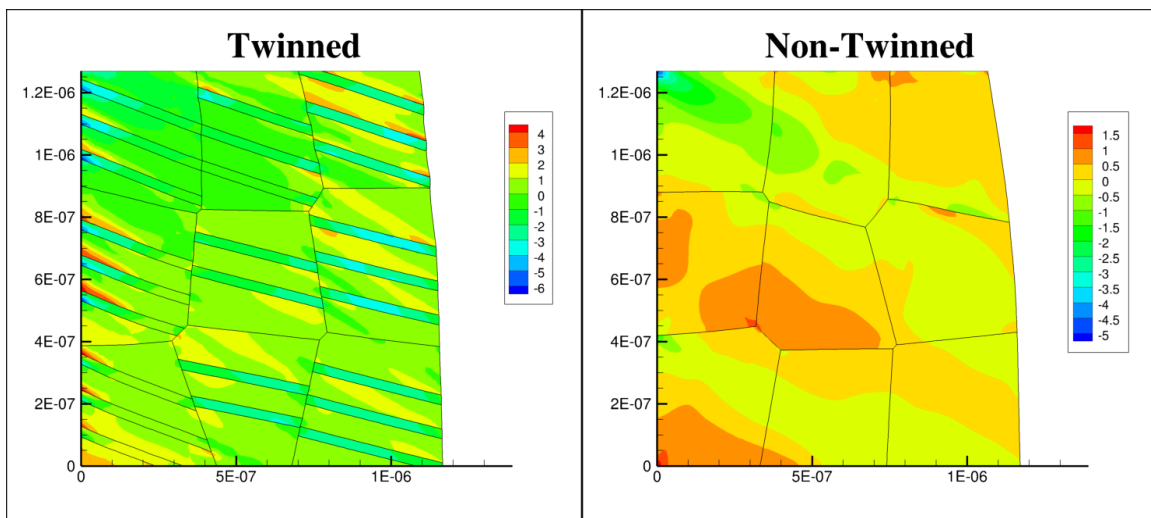
**Figure 31: Aggregate normal stress percentage increase from non-twinned to twinned materials plotted against orientation. Note that all twinned materials represent an increase in aggregate normal stress.**

**Figure 32: Normalized lateral stress for twinned and non-twinned materials. (All spatial units are in meters)**

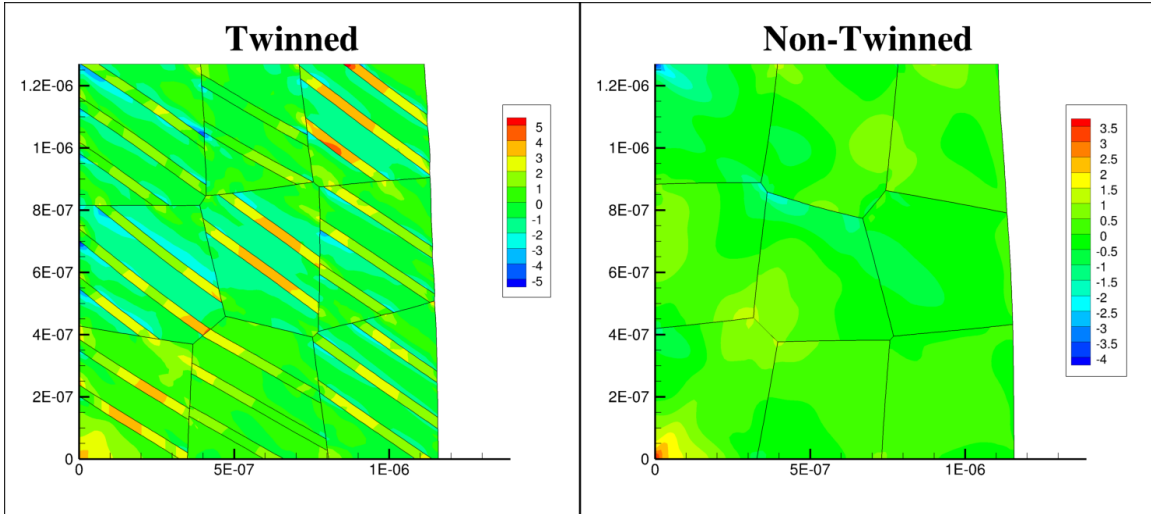
### Lateral Stress for 0° Orientation (Normalized by Yield Stress)



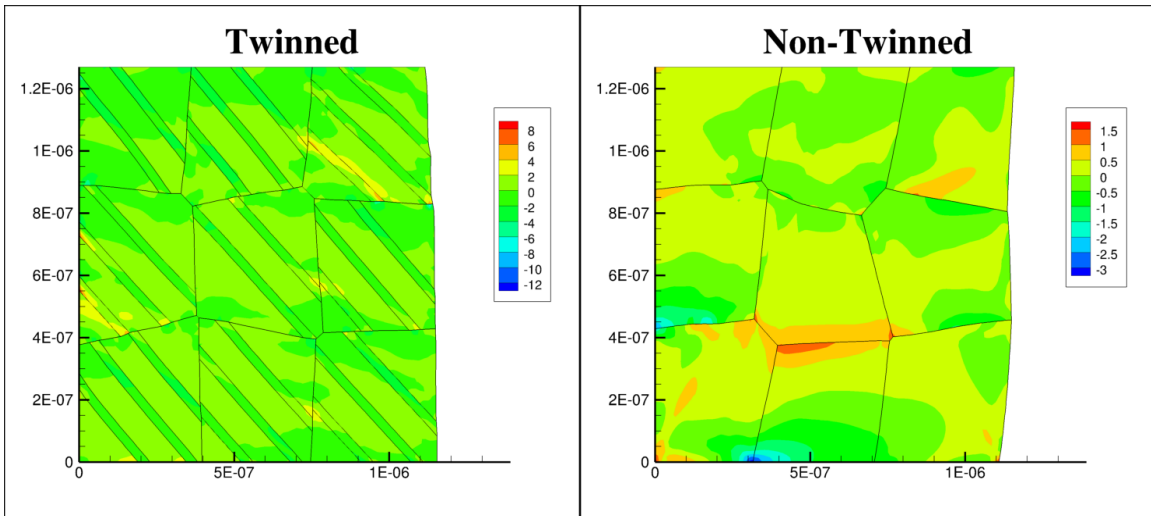
### 15° Orientation Lateral Stress



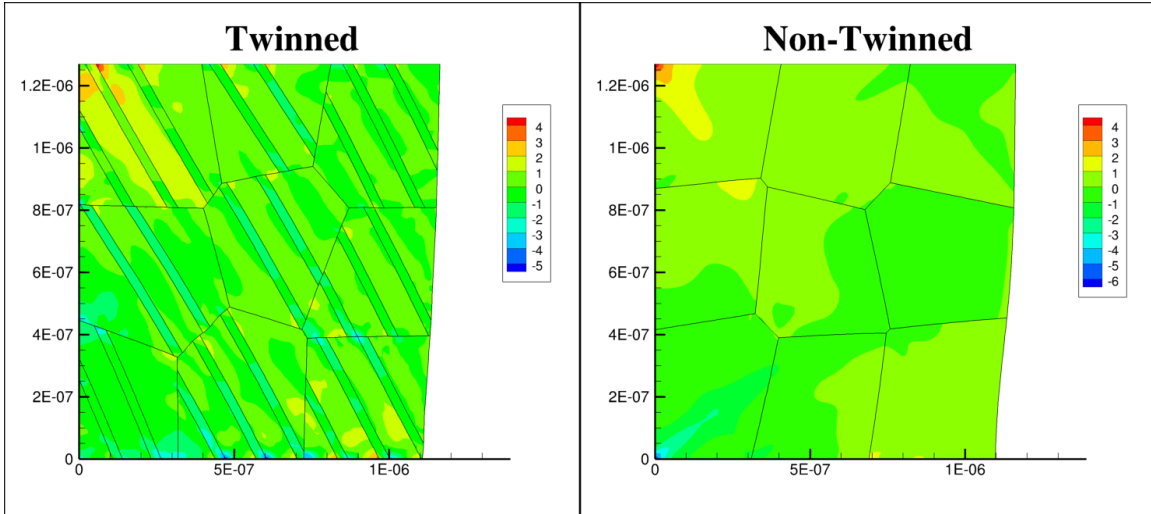
### 30° Orientation Lateral Stress



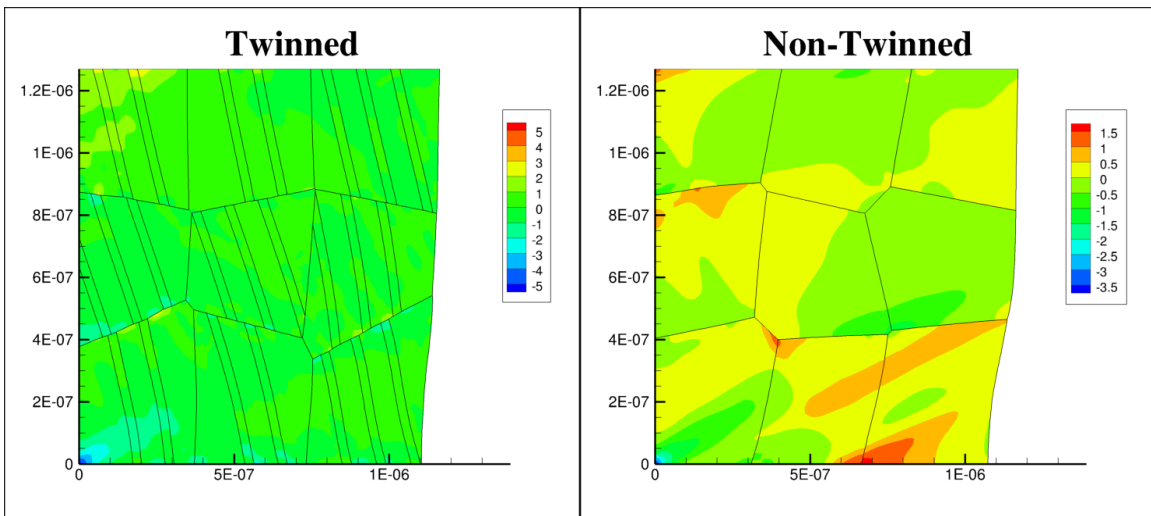
### 45° Orientation Lateral Stress



### 60° Orientation Lateral Stress



### 75° Orientation Lateral Stress



# 90° Orientation Lateral Stress

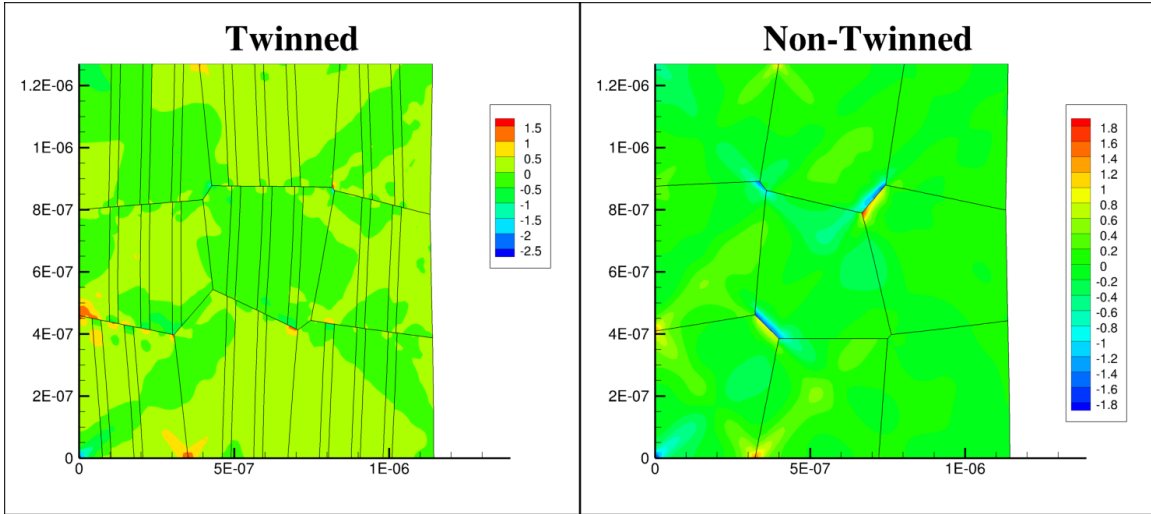
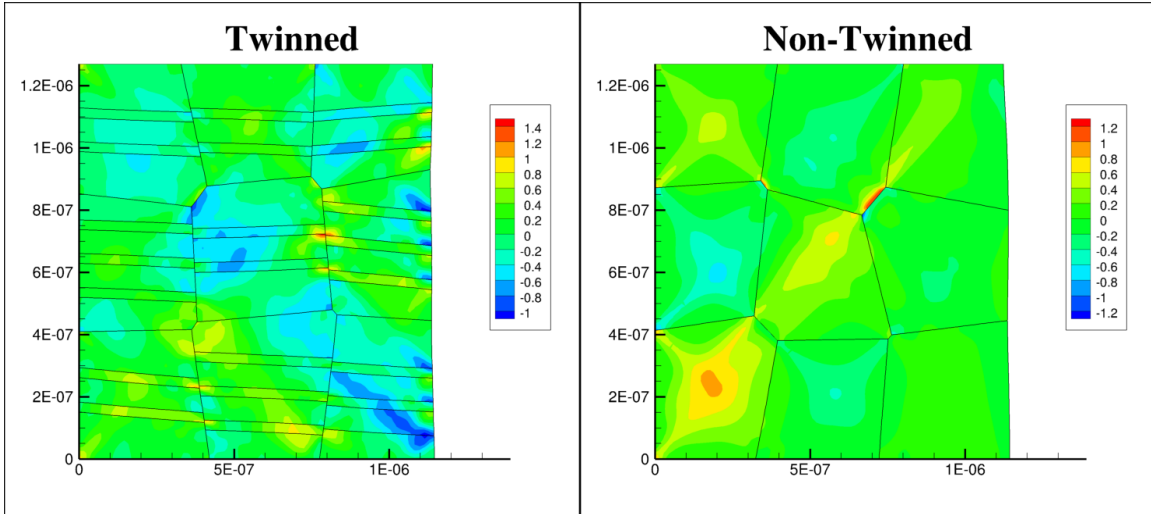
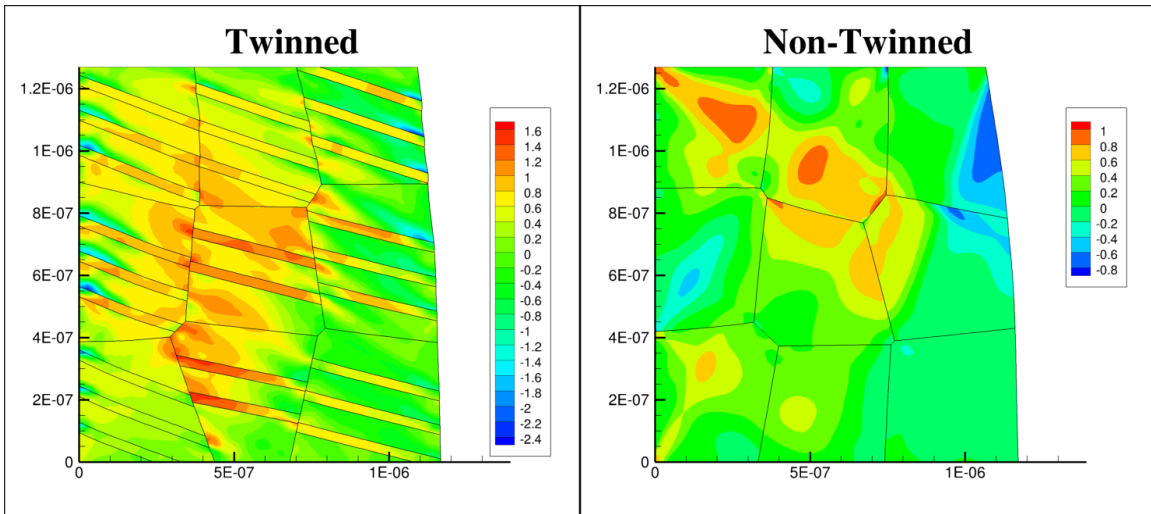


**Figure 33: Normalized Shear Stress for twinned and non-twinned materials. (All spatial units are in meters)**

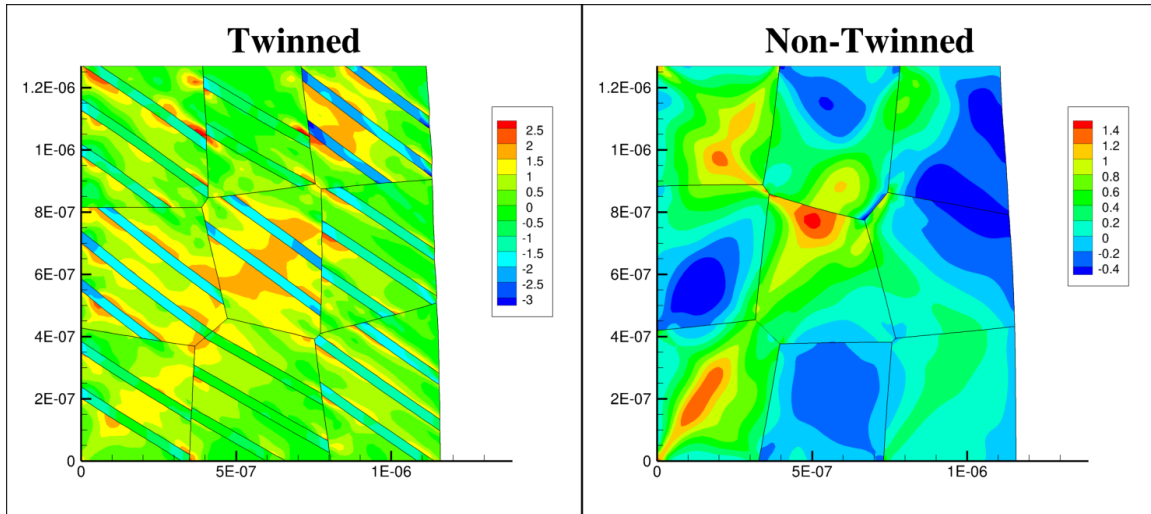
### Shear Stress for 0° Orientation (Normalized)



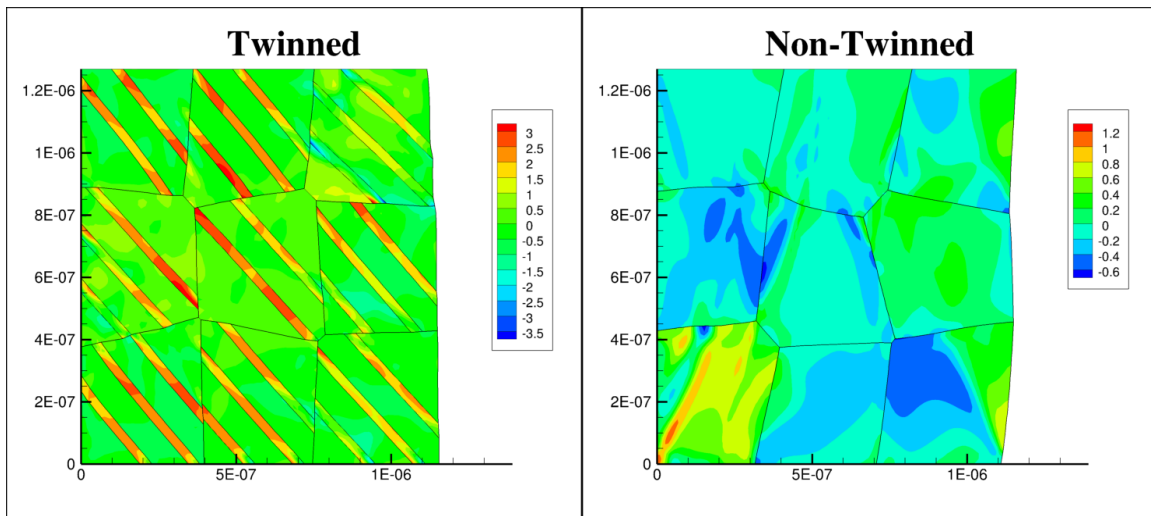
### 15° Orientation Shear Stress



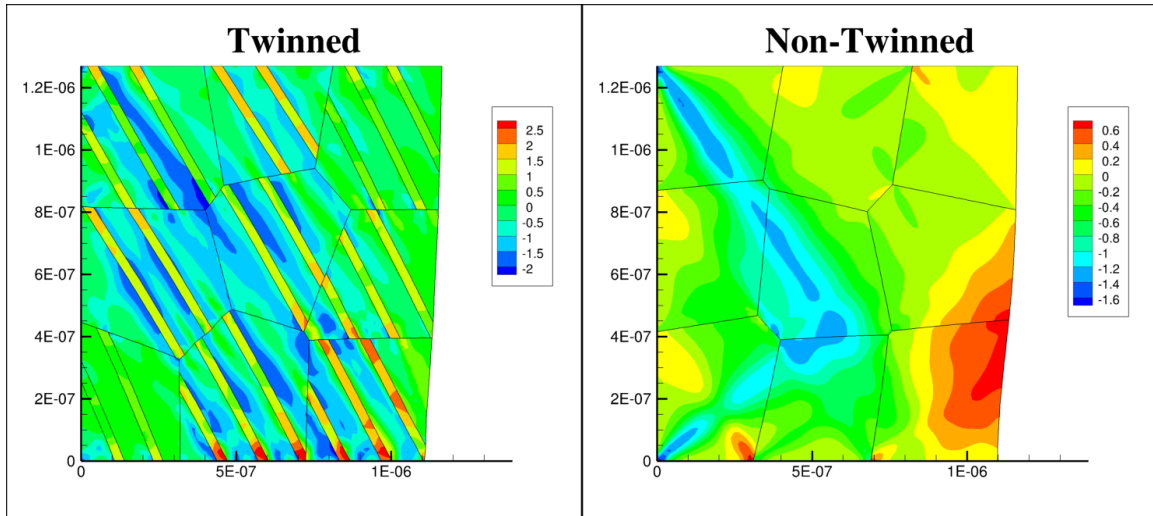
### 30° Orientation Shear Stress



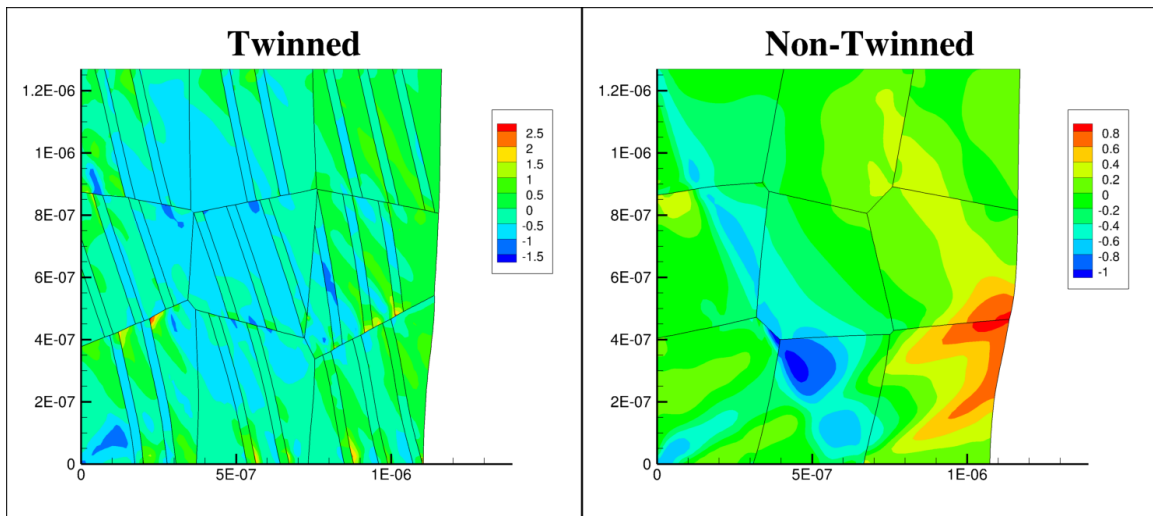
### 45° Orientation Shear Stress



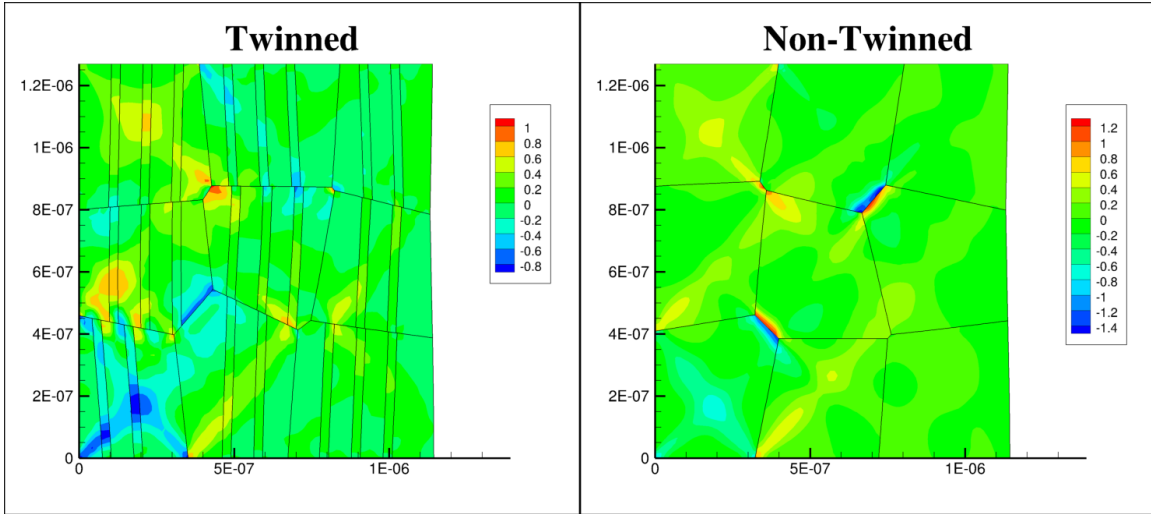
### 60° Orientation Shear Stress



### 75° Orientation Shear Stress



# 90° Orientation Shear Stress



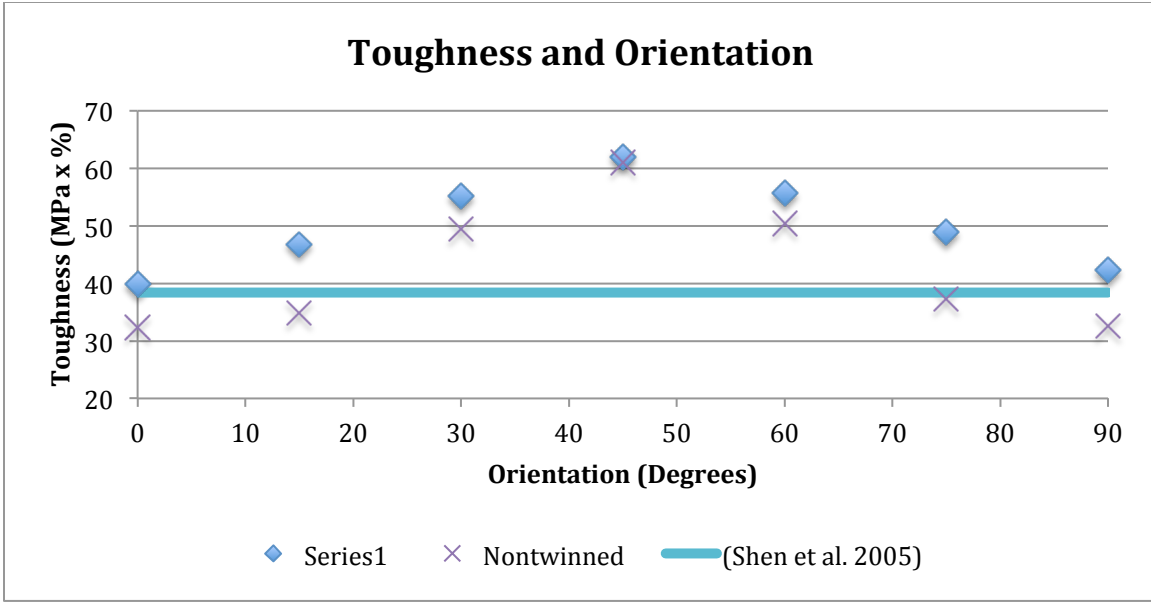


**Figure 34: Compressive loading at different orientations compared with experimental toughness for comparison.**

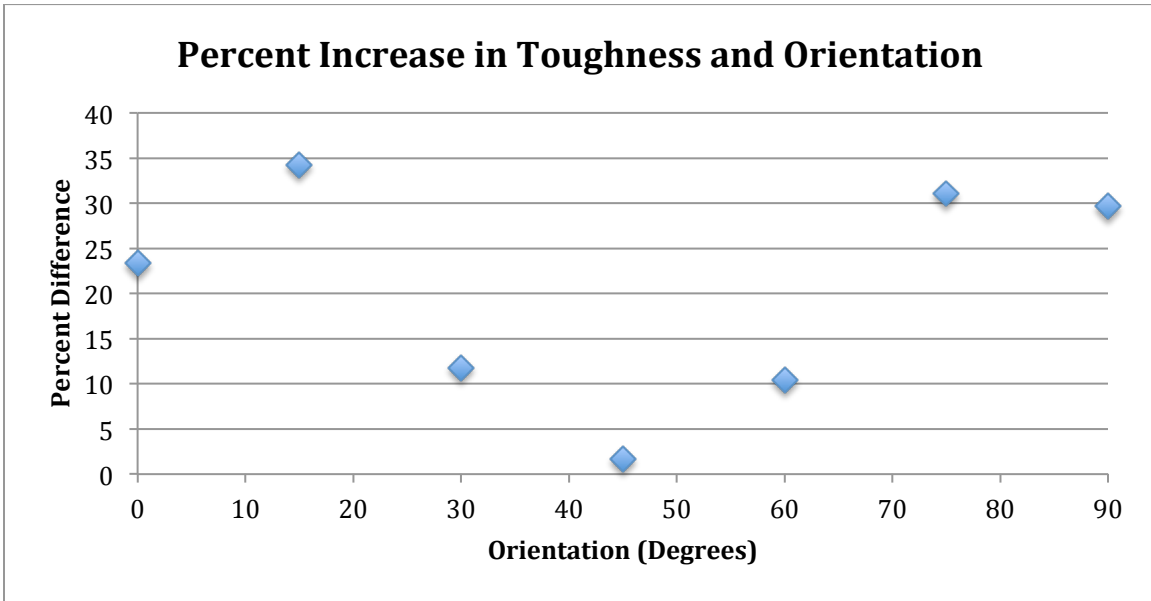


**Figure 35: Toughness increase from non-twinned simulation shown as function of orientation.**

## CHAPTER 5: RECOMMENDATIONS FOR FUTURE RESEARCH

The following are recommendations for future research, based upon the findings of this investigation:

- Incorporate failure modeling appropriate for f.c.c. materials to obtain more accurate toughness values and values for ultimate tensile strength (Rezvanian, Zikry and Rajendran 2007) and (Wu and Wei 2008).
- Perform analysis on the effects of varying grain misorientations in twinned materials.
- The current study focused on varying the twin orientation in the plane with a Y-axis normal. Varying twin orientation in the plane with the X-axis normal will likely activate other slip systems and yield a broader understanding of preferentially oriented twin structures.
- Use a plane stress formulation as opposed to plane strain to quantify the effects of preferentially oriented twins in thin films because bulk-processing techniques remain under development.

## BIBLIOGRAPHY

Chen, Mingwei, En Ma, Kevin J. Hemker, Hongwei Sheng, Yinmin Wang, and Xuemei Cheng. "Deformation Twinning in Nanocrystalline Aluminum." *Science* 300 (2003): 1275-1277.

Chen, X. H., L. Lu, and K. Lu. "Grain size dependence of tensile properties in ultrafine-grained Cu with nanoscale grains." *Scripta Materialia* 64 (October 2011): 311-314.

Christian, J. W., and S. Mahajan. "Deformation Twinning." *Progress in Materials Science*, 1995: 1-157.

Cronje, S., R. E. Kroon, W. D. Roos, and J. H. Neethling. "Twinning in copper deformed at high strain rates." *Bulletin of Materials Science* 36, no. 1 (2013): 157-162.

Dao, M., L. Lu, Y. F. Shen, and S. Suresh. "Strength, strain-rate sensitivity and ductility of copper with nanoscale twins." *Acta Materialia*, 2006: 5421-5432.

Hong, C. S., N. R. Tao, K. Lu, and X. Huang. "Grain orientation dependence of deformation twinning in pure Cu subjected to dynamic plastic deformation." *Scripta Materialia*, 2009: 289-292.

Hong, C. S., N. R. Tao, X. Huang, and K. Lu. "Nucleation and thickening of shear bands in nano-scale twin/matrix lamellae of a Cu-Al alloy processed by dynamic plastic deformation." *Acta Materialia* 58 (2010): 3103-3116.

Hsiao, Hsiang-Yao, et al. "Unidirectional Growth of Microbumps on (111)-Oriented and Nanotwinned Copper." *Science* 336 (May 2012): 1007-1010.

Hutchinson, J. W. "Bounds and Self-Consistent Estimates for Creep of Polycrystalline Materials." *Proc. Roy. Soc. London* 348, no. A (1976): 101-127.

Kameda, T., and M. A. Zikry. "Three Dimensional Dislocation-Based Crystalline Constitutive Formulation for Ordered Intermetallics." *Scripta Materialia* 38, no. 4 (1998): 631-636.

Koch, C. C., D. G. Morris, K. Lu, and A. Inoue. "Ductility of Nanostructured Materials." *Materials Research Society Bulletin* 24, no. 2 (1999): 54-58.

Li, Xiaoyan, Yujie Wei, Lei Lu, Ke Lu, and Huajian Gao. "Dislocation nucleation governed softening and maximum strength in nano-twinned metals." *Nature* 464, no. 8 (2010): 877-880.

Lu, L., R. Schwaiger, Z. W. Shan, M. Dao, K. Lu, and S. Suresh. "Nano-sized twins induce high rate sensitivity of flow stress in pure copper." *Acta Materialia* 53 (January 2005): 2169-2179.

Lu, Lei, Ting Zhu, Yongfeng Shen, Ming Dao, K. Lu, and Subra Suresh. "Stress relaxation and the structure size-dependence of plastic deformation in nanotwinned copper." *Acta Materialia* 57 (August 2009): 5165-5173.

Lu, Lei, Yongfeng Shen, Xianhua Chen, Lihua Qian, and K. Lu. "Ultrahigh Strength and High Electrical Conductivity in Copper." *Science* 304 (April 2004): 422-426.

Mirkhani, Hamidreza, and Shailendra P. Joshi. "Crystal plasticity of nanotwinned microstructures: A discrete twin approach for copper." *Acta Materialia*, 2011: 5603-5617 .

Niewczas, Marek. *Dislocations and Twinning in Face Centred Cubic Crystals*. Vol. 13, in *Dislocations in Solids*, edited by F.R.N. Nabarro and J. P. Hirth, 263-364. Elsevier B.V., 2007.

Pumphrey, P. H., and K. M. Bowkett. "Observation of Partial Dislocations on a Coherent Twin Boundary." *Philosophical Magazine* 24, no. 188 (1971): 225-230.

Rasmussen, T., T. Vegge, T. Leffers, O. B. Pedersen, and K. W. Jacobsen. "Simulation of structure and annihilation of screw dislocation dipoles." *Philosophical Magazine A* 80, no. 5 (2000): 1273-1290.

Rezvani, O., M. A. Zikry, and A. M. Rajendran. "Statistically stored, geometrically necessary and grain boundary dislocation densities: microstructural representation and modelling." *Proceedings of The Royal Society A*, 2007: 1-21.

Shan, Z. W., L. Lu, A. M. Minor, E. A. Stach, and S. X. Mao. "The effect of twin plane spacing on the deformation of copper containing a high density of growth twins." *Birck and NCN Publications* 60, no. 9 (September 2008): 71-74.

Shanthraj, P., and M. A. Zikry. "Dislocation density evolution and interactions in crystalline materials ." *Acta Materialia* 59, no. 20 (2011): 7695-7702.

Shen, Y. F., L. Lu, Q. H. Lu, Z. H. Jin, and K. Lu. "Tensile properties of copper with nano-scale twins ." *Scripta Materiala* 52 (2005): 989-994.

Wang, H. L., Z. B. Wang, and K. Lu. "Interfacial diffusion in a nanostructured Cu produced by means of dynamic plastic deformation." *Acta Materiala* 59 (2011): 1818-1828.

Wu, Bo, and Yuanguang Wei. "Simulations of mechanical behavior of polycrystalline copper with nano-twins." *Acta Mechanica Solida Sinica*, 2008: 189-197.

Wu, Z. X., Y. W. Zhang, and D. J. Srolovitz. "Dislocation-twin interaction mechanisms for ultrahigh strength and ductility in nanotwinned metals." *Acta Materialia* 57, no. 15 (2009): 4508-4518.

Xiao, G. H., N. R. Tao, and K. Lu. "Strength-ductility combination of nanostructured Cu-Zn alloy with nanotwin bundles." *Scripta Materialia* 65 (March 2011): 119-122.

Yamakov, V., D. Wolf, S. R. Phillpot, and H. Gleiter. "Dislocation-dislocation and dislocation-twin reactions in nanocrystalline Al by molecular dynamics simulation." *Acta Materialia* 51, no. 14 (2003): 4135-4147.

You, Z. S., L. Lu, and K. Lu. "Tensile behavior of columnar grained Cu with preferentially oriented nanoscale twins." *Acta Materialia* 59 (July 2011): 6927-6937.

Zhang, X., et al. "Enhanced hardening in Cu/330 stainless steel multilayers by nanoscale twinning." *Acta Materialia* 52 (2004): 995-1002.

Zhou, Haofei, Shaoxing Qu, and Wei Yang. "Toughening by nano-scaled twin boundaries in nanocrystals." *Modelling and Simulation in Materials Science and Engineering* 18 (2010): 1-10.

Zikry, M. A., and M. Kao. "Inelastic Microstructural Failure Mechanisms in Crystalline Materials with High Angle Grain Boundaries." *J. Mech. Phys. Solids* 44, no. 11 (1996): 1765-1798.